Eidgenössische Technische Hochschule Zürich
Swiss Federal Institute of Technology Zurich

Geometric Phase of a Harmonic Oscillator in Circuit QED

Master's Thesis in Physics
Presented by Marek Pechal
Supervised by Simon Berger and Dr. Stefan Filipp
Handed in to Prof. Dr. Andreas Wallraff,
Laboratory for Solid State Physics, ETH Zurich

Zurich, March 21, 2011

To read our E-mail, how mean
of the spies and their quantum machine;
Be comforted though,
they do not yet know
how to factorize twelve or fifteen.

Volker Strassen, 1998

Abstract

Quantum information processing is a concept which uses the laws of quantum mechanics to process and transport data in a fundamentally more efficient way than classical information technology. One of the schemes proposed to achieve reliable coherent control of quantum devices and to overcome decoherence effects, the biggest obstacle on the way towards practical implementations of quantum information processing, is based on geometric effects. The so-called geometric phase is a property of quantal evolution which only depends on the trajectory followed by the system in the space of quantum states and not on the dynamical properties of the evolution – its time scale and the eigenenergies of the underlying Hamiltonian. In this thesis, the geometric phase of an adiabatically manipulated harmonic oscillator realized as a transmission line resonator in a superconducting circuit is measured. We observe the expected scaling of the geometric phase with the square of the drive signal amplitude, its dependence on the direction and the shape of the path traced by the quantum state and its insensitivity to the length of the adiabatic sequence. We investigate dephasing effects caused by deviations from the ideal adiabatic regime. The results of our measurements are compared with the theoretical predictions and good quantitative agreements is found. In light of our results, a harmonic oscillator, a well-understood simple system, appears to be a convenient tool for studying the geometric phase and its potential use for quantum information processing.

Contents

List of Figures

1 Introduction

The theoretical concept of quantum computation emerged almost three decades ago when Richard P. Feynman [1] noted that general quantum systems cannot be efficiently simulated on classical computers. He pointed out that a new kind of computer, itself quantum mechanical in nature, is much better suited for simulating other quantum systems. This idea served as a direct evidence that there are certain computational tasks, at least in the field of quantum simulations, for which a suitable quantum computer outperforms a classical one.

Just a few years after Feynman, David Deutsch [2] came up with the concept of a *universal quantum computer* and showed that it is indeed computationally more powerful than its classical counterpart – the famous Turing machine. His quantum computer architecture operating with two-state quantum systems as elementary carriers of information, commonly known as *qubits*, has proven to be very convenient thanks to its similarity to the classical model of computation. This similarity makes it particularly easy to see that a quantum computer can simulate a classical one. The crucial aspect of efficient quantum computation is that a qubit can exist not only in its two basis states but also in their arbitrary linear superposition. This means that a quantum computer can process multiple inputs at the same time, thus allowing certain tasks to be solved significantly faster than on a classical computer.

Since Deutsch's pioneering theoretical work, a range of quantum algorithms have been found that offer more efficient solutions than classical ones for many concrete computational problems unrelated to simulating quantum mechanics. Some of the more famous examples are the Deutsch-Jozsa algorithm [3], Grover's search algorithm [4] and Shor's factoring algorithm [5]. The latter is widely known thanks to its serious implications for cryptography.

A natural set of requirements that a physical system has to meet to realize quantum computation has been formulated by David P. DiVincenzo [6]. These criteria are: the existence of well-defined qubits, the possibility to initialize them in a pure quantum state, manipulate them unitarily by a universal set of quantum gates and measure the state of individual qubits. Also, the coherence time of the system needs to be long compared to the typical operation time. In the past two decades, several different physical implementations of quantum computation [7] that satisfy some or all of the DiVincenzo criteria have been proposed and experimentally tested. Examples are trapped ions [8], nuclear spins inside organic molecules [9], semiconducting quantum dots [10] and superconducting qubits [11].

The latter approach is currently developed at the Quantum Device Lab at ETH Zurich. Quantum bits based on superconducting electrical circuits are well controllable [12] and exhibit relatively long coherence times. They can be easily coupled via microwave transmission line resonators [13] which also serve as an efficient read-out channel [14]. The interactions between the qubits and photons mediating the coupling are described by

the theory of *circuit quantum electrodynamics*. Superconducting circuits are therefore a promising candidate for quantum computation and considerable effort is currently devoted to their study and further development.

Significant effort is directed towards solving one of the big problems inevitably facing any quantum device – the loss of quantum coherence due to dissipation and dephasing processes. These effects can be caused by interactions of the quantum system with its environment or by fluctuations of the control parameters used to manipulate the device. One interesting possibility to deal with the latter is offered by the concept of *geometric quantum computation*. It is based on the fact that a quantum state tracing out a given path in the projective Hilbert space acquires a complex phase which contains a geometric contribution – a part of the total phase which does not depend on dynamical quantities such as energy and time but only on the path traversed by the state [15]. Consequently, qubit operations utilizing the geometric rather than the dynamical phase are believed to be less susceptible to noise in their control parameters. Apart from its potential practical application, the geometric phase is also interesting from the theory point of view because of its intriguing connections with differential geometry [16]. Recently, the geometric phase has been studied experimentally in superconducting qubits [17, 18].

Another simple quantum system in which geometric effects can be observed and investigated is the harmonic oscillator whose exact integrability allows us to study the geometric phase analytically.

The use of the geometric phase of a harmonic oscillator for the realization of quantum gates has been studied theoretically [19, 20] and demonstrated experimentally in trapped ion qubits [21]. In the present work, we experimentally observe the geometric phase of an adiabatically manipulated harmonic oscillator in a superconducting circuit. We make use of the circuit QED setup – a microwave resonator coupled to a superconducting qubit – in the so-called *dispersive regime*. In this way, the resonator can be treated as a harmonic oscillator with a frequency depending on the state of the qubit. This allows us to measure the difference between the geometric phases for the two different resonator frequencies in a simple interference experiment.

A theoretical description of the measurement as well as a presentation and discussion of its results are the main aims of this thesis. An introduction into superconducting circuits used for quantum information processing together with a general theoretical overview of the geometric phase is given in Sections 2 and 3. Section 4 presents a more specific theoretical description of the geometric phase for the circuit QED system used in our experiment. Section 5 comprises a description of the experimental setup and methods, the obtained results and their discussion.

2 Superconducting qubits and circuit QED

2.1 Superconducting qubits

Superconductivity in metals, a remarkable phenomenon where at sufficiently low temperatures a material becomes a perfect electrical conductor, is caused by condensation of electrons into bosonic Cooper pairs – two-particle bound states held together by a phonon-mediated attractive interaction [22]. The fact that charge carriers in a superconductor macroscopically occupy a single quantum ground state allows superconducting circuits to exhibit quantum mechanical properties on a much larger scale than most other systems (μm as opposed to nm scale of quantum dots or sub-nm scale of trapped ions).

The classical passive electronic components alone, capacitors and inductors, cannot constitute a non-trivial quantum system because of their linearity. Any circuit composed solely of these linear components is equivalent to a system of harmonic oscillators. To create an anharmonic system usable for quantum computation, a non-linear element is needed. This can be provided by incorporating a *Josephson junction* into the circuit.

2.1.1 Josephson junctions

As predicted theoretically by B. D. Josephson [23], electric current can flow through a thin insulating junction separating two superconductors due to quantum tunneling of Cooper pairs. This tunneling current I depends on the phase difference $\Delta\varphi$ between the macroscopic wave function of the two superconductors which is in turn related to the voltage V across the junction. The non-linear equations describing the electrical properties of a Josephson junction are [22]

$$I = I_c \sin \Delta\varphi, \tag{1a}$$

$$\Delta\dot{\varphi} = \frac{2\pi V}{\Phi_0}, \tag{1b}$$

where the so-called *critical current* I_c is a parameter of the junction and $\Phi_0 = h/2e$ is the magnetic flux quantum. The two equations imply the following direct relation between the current and the voltage:

$$\dot{I} = \frac{2\pi V}{\Phi_0}\sqrt{I_c^2 - I^2}.$$

This means that a Josephson junction can be viewed as a non-linear inductor with a current-dependent inductance $L = \Phi_0/2\pi\sqrt{I_c^2 - I^2}$. The energy of the junction is given by

$$E = \int V I \,\mathrm{d}t = \int \frac{\Phi_0 I_c}{2\pi} \sin\Delta\varphi \,\mathrm{d}\Delta\varphi = -\frac{\Phi_0 I_c}{2\pi}\cos\Delta\varphi. \tag{2}$$

The quantity $\Phi_0 I_c/2\pi$ is usually called *Josephson energy* of the junction and denoted by E_J.

The Josephson junction as described above is obviously a highly idealized concept. Real junctions can possess additional non-zero conductance, inductance or capacitance. However, it turns out that the first two quantities can be indeed neglected in most cases and a real Josephson junction can be quite accurately modelled as an ideal junction with an additional capacitance connected in parallel (see Fig. 1a).

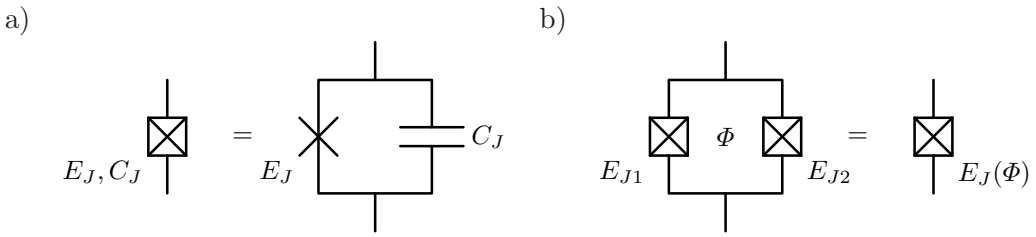

Figure 1: Equivalent circuits for a real and a split Josephson junction. (a) A real Josephson junction (commonly represented in circuit diagrams by a crossed square) can be described as an ideal junction (represented by a cross) characterised by its Josephson energy E_J and a parallel capacitance C_J connected in parallel. (b) A split Josephson junction is equivalent to a simple junction with a variable Josephson energy depending on the magnetic flux Φ through the loop.

It can be easily shown that two junctions with Josephson energies E_{J1} and E_{J2} connected in parallel – the so-called *split Josephson junction* – are equivalent to a single junction with a Josephson energy which depends on the magnetic flux through the loop (see Fig. 1b). The phase differences across the junctions are related to the flux by [22] $\Delta\varphi_1 - \Delta\varphi_2 = 2\pi\Phi/\Phi_0$. This together with Eqs. (1) implies that the relations between the current, the phase difference and the voltage for the split junction are of the same form as Eqs. (1) with

$$\begin{aligned} I_c &= \sqrt{I_{c1}^2 + I_{c2}^2 + 2I_{c1}I_{c2}\cos(2\pi\Phi/\Phi_0)}, \\ \Delta\varphi &= \frac{1}{2}(\Delta\varphi_1 + \Delta\varphi_2) + \arg(I_{c1}\mathrm{e}^{\mathrm{i}\pi\Phi/\Phi_0} + I_{c2}\mathrm{e}^{-\mathrm{i}\pi\Phi/\Phi_0}). \end{aligned}$$

This configuration of two junctions can therefore be conveniently used to tune the Josephson energy by an externally applied magnetic field.

2.1.2 Quantization of a circuit – Cooper pair box

The procedure of quantizing the circuit is rather straightforward (see e.g. [24]). After expressing the energy of the system in terms of the wave function phases φ_i and numbers n_i of Cooper pairs in all disconnected parts of the circuit, one replaces these quantities by operators to obtain the quantum-mechanical Hamiltonian and imposes the canonical commutation relations

$$[\hat{n}_i, \hat{\varphi}_j] = \mathrm{i}\delta_{ij}$$

for each pair of indices i, j. It is noteworthy that the energy term $\hat{H}_J^{ij}$ deduced from Eq. (2) that corresponds to a Josephson junction between superconducting islands i and

j, when written in terms of $\hat{\varphi}_i$ and $\hat{\varphi}_j$, can be expressed as a sum of two operators $\hat{H}^{ij}_{J\pm} = E_J e^{\pm i(\hat{\varphi}_i - \hat{\varphi}_j)}/2$. These satisfy $[\hat{n}_i, \hat{H}^{ij}_{J\pm}] = \mp\hat{H}^{ij}_{J\pm}$ and $[\hat{n}_j, \hat{H}^{ij}_{J\pm}] = \pm\hat{H}^{ij}_{J\pm}$, reminiscent of the commutation relations $[\hat{a}^\dagger\hat{a}, \hat{a}] = -\hat{a}$ and $[\hat{a}^\dagger\hat{a}, \hat{a}^\dagger] = \hat{a}^\dagger$ of creation and annihilation operators. They can therefore be very naturally interpreted as representing the process of one Cooper pair tunneling through the junction.

There are several widely used types of superconducting qubits (see Fig. 2). They are usually classified according to the macroscopic quantity which is most relevant to interactions and readout of the qubit. Examples include the flux qubit consisting of a superconducting ring divided by one or three Josephson junction [25], the phase qubit which is essentially a single current-biased junction [26] and the Cooper pair box qubit in which tunneling of charge carriers between a reservoir and a superconducting island is controlled by a bias voltage [24].

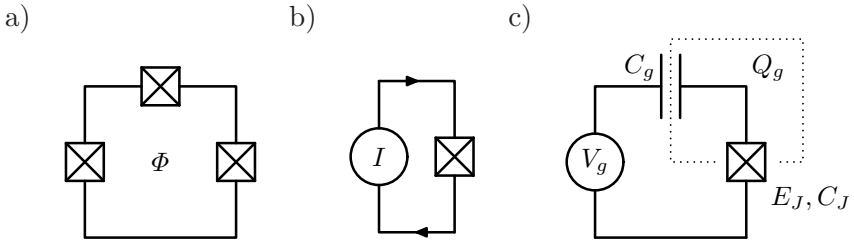

Figure 2: Types of superconducting qubits. Circuit diagrams of (a) a flux qubit, (b) a phase qubit and (c) a Cooper pair box as three examples of superconducting qubit designs. The dotted rectangle in (c) marks the island of the Cooper pair box.

We will further focus on the Cooper pair box as it is closely related to the transmon qubit used in our setup. If we denote the electric potential of the Cooper pair box (see Fig. 2c) by V, the total charge Q_g on the superconducting island is given by $C_g(V - V_g) + C_J V$. The electrostatic energy of the system is

$$\begin{aligned} E_{\text{el}} &= \frac{1}{2}C_g(V - V_g)^2 + \frac{1}{2}C_J V^2 - C_g V_g(V - V_g) \\ &= \frac{(Q_g - C_g V_g)^2}{2(C_g + C_J)} + \dots, \end{aligned}$$

where the omitted terms represent an irrelevant overall energy shift independent of Q_g. After expressing the charge in terms of the excess number n of Cooper pairs on the island as $Q_g = -2en$ and defining a convenient dimensionless measure of the bias voltage $n_g = -C_g V_g/2e$ we obtain [24]

$$E_{\text{el}} = \frac{2e^2}{C_g + C_J}(n - n_g)^2.$$

The factor $e^2/2(C_g + C_J)$ is commonly denoted as the *charging energy*[1] E_C of the Cooper pair box. After adding the contribution of the Josephson junction we arrive at the Hamiltonian of the system

$$\hat{H} = 4E_C(\hat{n} - n_g)^2 - E_J \cos \Delta\hat{\varphi}. \tag{3}$$

The operators $\mathrm{e}^{\pm \mathrm{i}\Delta\hat{\varphi}}$ satisfy commutation relations

$$[\hat{n}, \mathrm{e}^{\pm \mathrm{i}\Delta\hat{\varphi}}] = \mp \mathrm{e}^{\pm \mathrm{i}\Delta\hat{\varphi}}$$

and therefore act as ladder operators on eigenstates of $\hat{n}$. The Hamiltonian (3) can then be written in the eigenbasis of $\hat{n}$ as [24]

$$\hat{H} = 4E_C \sum_n (n - n_g)^2 |n\rangle\langle n| + E_J \sum_n \frac{|n\rangle\langle n+1| + |n+1\rangle\langle n|}{2}.$$

The Cooper pair box is typically operated in a regime where the charging energy E_C dominates over the Josephson energy E_J, i.e. $E_C \gg E_J$, and with the bias voltage adjusted so that n_g is a half-integer. Let us assume without loss of generality that $n_g = 1/2$. Then the only pair of states $|n\rangle$ for which the coupling terms cannot be neglected are $|0\rangle$ and $|1\rangle$. All other pairs of consecutive states are separated by energies much larger than the coupling energy E_J and can be considered as effectively decoupled.

The Hamiltonian restricted to the space spanned by the states $|0\rangle$ and $|1\rangle$ then takes the simple form

$$\hat{H} = \frac{1}{2} E_J \left(|0\rangle\langle 1| + |1\rangle\langle 0| \right).$$

The eigenvectors of this Hamiltonian are $|g\rangle = (|0\rangle - |1\rangle)/\sqrt{2}$ with eigenenergy $-E_J/2$ and $|e\rangle = (|0\rangle + |1\rangle)/\sqrt{2}$ with eigenenergy $E_J/2$. These two states are well separated from the rest of the energy spectrum which means that the Cooper pair box can be operated as an effectively two-level system and used as a qubit.

It can be manipulated by means of an additional voltage source V_e coupled by a capacitance C_e to the superconducting island in the same way as the bias voltage V_g. The derivation of the Hamiltonian is analogous to that of Eq. (3) and results in a similar expression but with the total capacitance in the charging energy now including C_e and with n_g replaced by $n_g - C_e V_e/2e$. Apart from a simple change in the definition of E_C and an overall energy shift, this modification therefore amounts to adding the term $4(n - n_g)E_C C_e V_e/e$ to the Hamiltonian. When written in terms of the computational basis states $|g\rangle$ and $|e\rangle$, the total Hamiltonian has the form

$$\hat{H} = \frac{1}{2} E_J (|e\rangle\langle e| - |g\rangle\langle g|) - \frac{2E_C C_e}{e} V_e (|e\rangle\langle g| + |g\rangle\langle e|),$$

[1] Note that the definitions of this quantity in Refs. [24] and [27] differ by a factor of 4 due to the definition of n in terms of electrons or Cooper pairs. Here we employ the convention used in [27].

which we can express using the Pauli matrices

$$\begin{aligned}\hat{\sigma}_x &= |e\rangle\langle g| + |g\rangle\langle e|,\\ \hat{\sigma}_y &= \mathrm{i}|g\rangle\langle e| - \mathrm{i}|e\rangle\langle g|,\\ \hat{\sigma}_z &= |e\rangle\langle e| - |g\rangle\langle g|\end{aligned}$$

as

$$\hat{H} = \frac{1}{2}\hbar\omega_q\hat{\sigma}_z + \hbar\Omega_x\hat{\sigma}_x, \tag{4}$$

where $\omega_q = E_J/\hbar$ and $\Omega_x = -4E_C C_e V_e/\hbar e$. This form is strongly reminiscent of the Hamiltonian of a spin 1/2 particle with a magnetic moment in a magnetic field, a well understood system, very extensively studied in the context of nuclear magnetic resonance.

Note that the simple scheme described above is by no means the only way in which external voltage can be capacitively coupled to the qubit. For example, the qubit need not be physically connected to the ground, as is the case for our experimental sample. In that case, it is more appropriate to think of the qubit as consisting of two superconducting islands rather than an island and a reservoir. In general, there can be arbitrary cross-capacitances between the two islands, the ground and the voltage source. Although this makes the derivation of the Hamiltonian more tedious, the resulting coupling term has always the same form proportional to $V_e\hat{n}$.

As the energy separation between the two qubit levels depends on the bias voltage V_g, fluctuations in this control parameter will result in dephasing of the qubit. Close to the working point $n_g = 1/2$ the relative qubit frequency shift $\Delta\omega_q/\omega_q$ caused by a small deviation of n_g by Δn_g (charge dispersion) can be approximated as [27]

$$\frac{\Delta\omega_q}{\omega_q} = 32\Delta n_g^2\left(\frac{E_C}{E_J}\right)^2.$$

Since Cooper pair box qubits operate at $E_C/E_J > 1$ this relation makes it clear that they are particularly sensitive to noise in the bias voltage which can be brought about by charge fluctuations in the surrounding conductors.

2.1.3 The transmon qubit

It may seem natural to use the opposite regime $E_J \gg E_C$ to circumvent this problem. However, such possibility has not been seriously considered until relatively recently because it was thought the weak anharmonicity of the system would render it unusable as a qubit. As shown in Ref. [27], one can still benefit from the reduced charge dispersion while keeping the anharmonicity sufficiently high by shunting the Josephson junction with a large capacitance C_B, thus decreasing E_C. The modified version of the Cooper pair box is then operated in the regime $E_J \gg E_C$. Since the charge dispersion of the

qubit is then significantly suppressed, it is no longer necessary to precisely tune n_g and the bias voltage can be omitted altogether. Still, the energy of the qubit can be tuned by an external magnetic field if a split Josephson junction is used in the circuit. A diagram of the resulting *transmon qubit* is shown in Fig. 3a. For comparison, Fig. 3b shows the real qubit fabricated on a chip as seen under an optical microscope.

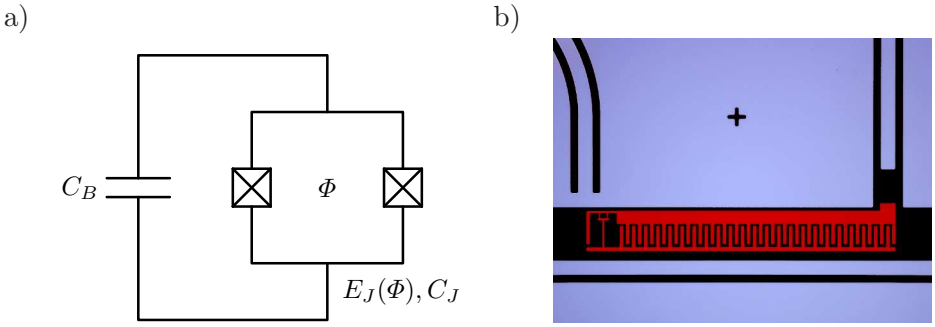

Figure 3: The transmon qubit. (a) Its circuit diagram shows the split Josephson junction shunted by a large capacitance C_B. Unlike for the Cooper pair box, voltage bias is not needed in the transmon qubit. (b) Optical microscope image of the qubit (in false colours as red) showing the zipper-like structure of the shunting capacitance on the right as well as the split Josephson junction on the left. The additional structures in the picture are used to manipulate and read out the qubit. The image is courtesy of J. Fink.

As the structure of the transmon qubit is essentially identical to that of a Cooper pair box with $C_g = C_B$ and $V_g = 0$, we can directly use Eq. (3) and write the Hamiltonian of the transmon as

$$\hat{H} = 4E_C\hat{n}^2 - E_J\cos\hat{\varphi},$$

where $E_C = e^2/2(C_B + C_J) \approx e^2/2C_B$ is the charging energy of the qubit. Because $E_J \gg E_C$, it turns out to be more convenient to express the state vector of the system in the eigenbasis of $\hat{\varphi}$ instead of $\hat{n}$. The phase φ is a continuous variable and the state $|\Psi\rangle$ can be represented by a wave function $\Psi(\varphi) = \langle\varphi|\Psi\rangle$. Since two values of the phase differing by a multiple of 2π are physically indistinguishable, the wave function has to be periodic, i.e. $\Psi(\varphi + 2\pi) = \Psi(\varphi)$.

The commutation relation $[\hat{n}, \hat{\varphi}] = \mathrm{i}$ implies that $\hat{n}$ in the φ-representation is given by the differential operator $\mathrm{i}\,\mathrm{d}/\mathrm{d}\varphi$. We can then write the time-independent Schrödinger equation as

$$-4E_C\frac{\mathrm{d}^2\Psi(\varphi)}{\mathrm{d}\varphi^2} - E_J\Psi(\varphi)\cos\varphi = E\Psi(\varphi). \tag{5}$$

The transmon qubit is therefore equivalent to a quantum mechanical particle moving in a one-dimensional periodic potential (with the additional requirement of periodicity forcing the lattice momentum generating discrete translations by 2π to be zero). The wave functions satisfying Eq. (5) can be expressed in terms of the so-called *Mathieu functions* [28]. However, in the limit $E_J \gg E_C$ a simple approximate solution of the Schrödinger equation can be found using perturbation theory.

The condition $E_J \gg E_C$ implies that the minimum of the "potential energy" $V(\varphi) = -E_J \cos\varphi$ is very deep. It is therefore quite reasonable to expect the wave function to be strongly peaked around $\varphi = 0$ where $V(\varphi)$ can be well approximated by its Taylor series. We will take into consideration only the terms up to fourth order in φ, i.e. $V(\varphi) = -E_J(1 - \varphi^2/2 + \varphi^4/24)$. Neglecting the fourth order term for the moment, we see that the Hamiltonian exactly matches that of a harmonic oscillator with mass m and frequency ω if we make the following correspondence:

harmonic oscillator	transmon qubit
x	φ
$\hbar^2/2m$	$4E_C$
$m\omega^2$	E_J

This parallel allows us to immediately write the Hamiltonian and the operators $\hat{n}$ and $\hat{\varphi}$ in terms of the well known ladder operators [29] as

$$\hat{H} = \sqrt{8E_C E_J}\left(\hat{b}^\dagger \hat{b} + \frac{1}{2}\right) - \frac{1}{12}E_C(\hat{b}^\dagger - \hat{b})^4 - E_J, \tag{6a}$$

$$\hat{n} = \sqrt[4]{\frac{E_J}{32E_C}}(\hat{b}^\dagger + \hat{b}), \tag{6b}$$

$$\hat{\varphi} = \mathrm{i}\sqrt[4]{\frac{2E_C}{E_J}}(\hat{b}^\dagger - \hat{b}). \tag{6c}$$

Here we have again included the term quartic in $\hat{\varphi}$ in our Hamiltonian (6a) and we substituted for $\hat{\varphi}$ from Eq. (6c). In order to determine the energy levels of the transmon qubit, we can treat this term as a perturbation. The first order correction to the n-th level energy is $\Delta E_n^{(1)} = -E_C\langle n|(\hat{b}^\dagger - \hat{b})^4|n\rangle/12$. This expression can be easily evaluated using the properties of annihilation and creation operators and the corrected energy can be cast into the form

$$E_n = \left(\sqrt{8E_C E_J} - E_C\right)n - E_C\frac{n(n-1)}{2} + \ldots$$

The ellipsis here stands for the omitted ground state energy. We can see that the presence of the quartic term leads to a small relative shift of the transmon transition energy $\hbar\omega_q = E_1 - E_0$ from $\sqrt{8E_C E_J}$ to $\sqrt{8E_C E_J} - E_C$ as well as to anharmonic energy level spacing given by

$$(E_{n+1} - E_n) - (E_1 - E_0) = \hbar\alpha n,$$

where the *anharmonicity* of the transmon qubit is simply $\alpha = -E_C/\hbar$.

We can then rewrite the diagonalized transmon Hamiltonian to lowest order in the quartic interaction as

$$\hat{H} = \hbar\sum_{n=0}^{\infty}\underbrace{\left(\omega_q n + \frac{1}{2}\alpha n(n-1)\right)}_{\omega_{qn}}|n\rangle\langle n|. \tag{7}$$

Note that the states $|n\rangle$ appearing here are eigenstates of the perturbed Hamiltonian, not the harmonic oscillator. Consequently, the ladder operators $\hat{b}, \hat{b}^\dagger$ in this basis do not satisfy the standard relation $\hat{b}|n\rangle = \sqrt{n}|n-1\rangle$ but are rather given by the formula

$$\hat{b} = \sum_{m,n=0}^{\infty} \lambda_{mn} |m\rangle\langle n|, \tag{8}$$

where $\lambda_{mn} = \delta_{m,n-1}\sqrt{n} + \mathcal{O}(\sqrt{E_C/E_J})$.

The anharmonic level structure of the transmon makes it possible to manipulate the qubit in the subspace spanned by the two lowest levels $|0\rangle$ and $|1\rangle$. In this case one can describe the transmon by a Hamiltonian of the type given in Eq. (4). Nevertheless, the magnitude of the anharmonicity $\hbar\alpha$ relative to the transition energy $\hbar\omega_q$ scales as $(E_J/E_C)^{-1/2}$ and is therefore small in the transmon regime $E_J \gg E_C$. This means that a special care has to be taken to keep the qubit inside the computational subspace and eliminate possible unwanted effects of the higher energy levels. The similarity between the spectra of a transmon and a harmonic oscillator is illustrated in Fig. 4.

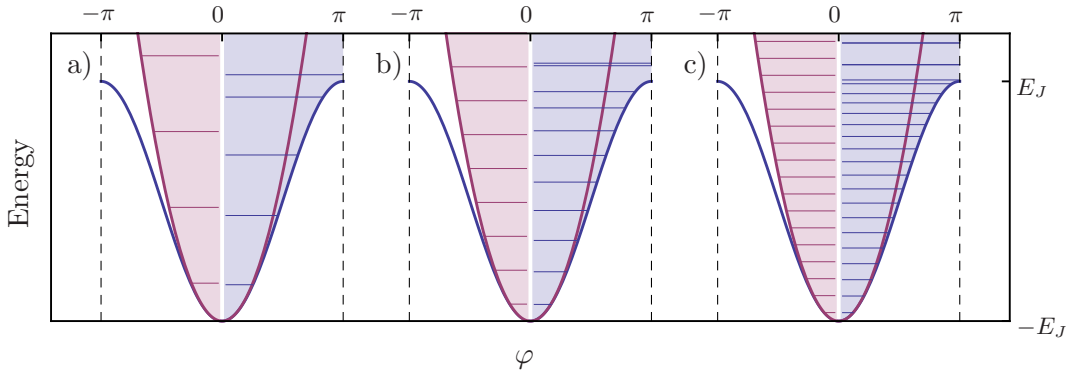

Figure 4: Energy levels of a transmon qubit (in blue) compared to those of a harmonic oscillator obtained by second order Taylor expansion of the Hamiltonian around $\varphi = 0$ (in purple). The levels represented by horizontal lines are superimposed on plots of the "potential energy" $V(\varphi)$ shown by thick lines. Comparison of the qubit energy levels for progressively increasing values of (a) $E_J/E_C = 20$, (b) $E_J/E_C = 100$ and (c) $E_J/E_C = 400$ illustrates that the anharmonicity decreases as $E_J/E_C \to \infty$.

The slight drawback presented by a weak anharmonicity has a bright side in a significantly reduced charge dispersion of the qubit. Although we set the bias voltage V_g to zero at the very beginning, it can obviously fluctuate around zero due to environmental effects. After replacing $\mathrm{i}\,\mathrm{d}/\mathrm{d}\varphi$ in the Schrödinger equation (5) by $\mathrm{i}\,\mathrm{d}/\mathrm{d}\varphi - n_g$, one can restore its original form by substituting $\Psi(\varphi) = \mathrm{e}^{-\mathrm{i}n_g\varphi}\Psi'(\varphi)$. The new wave function $\Psi'(\varphi)$ then again satisfies Eq. (5) but unlike $\Psi(\varphi)$, its boundary condition is $\Psi'(\varphi + 2\pi) = \mathrm{e}^{2\pi\mathrm{i}n_g}\Psi'(\varphi)$. After finding the eigenenergies as functions of n_g, one can observe that as the ratio E_J/E_C increases, the energy levels of the qubit become "flat" very quickly. In fact, the relative variation of the transition energies decreases *exponentially* [27] with increasing value of E_J/E_C, as is shown in Fig. 5. This significant suppression

of the charge dispersion makes the transmon qubit relatively resistant to dephasing due to environmental charge noise.

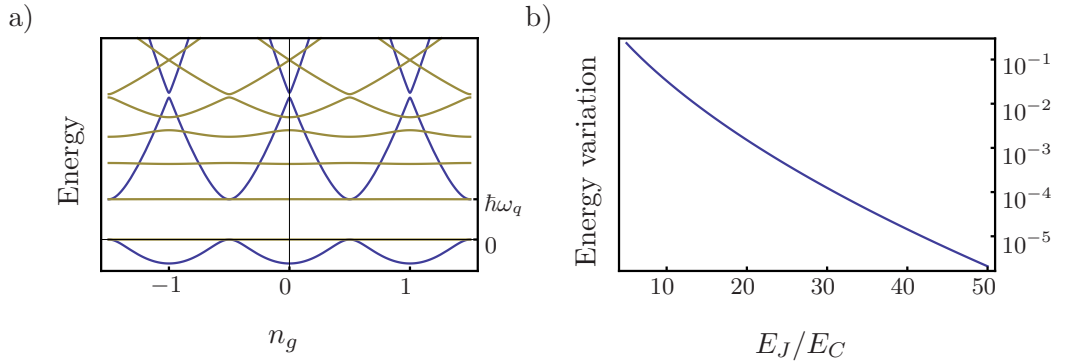

Figure 5: Charge dispersion of a transmon qubit. (a) Comparison between the dependence of the first few energy levels on the offset charge n_g for a qubit with $E_J/E_C = 1$ (in blue) and for a qubit in the transmon regime with $E_J/E_C = 20$ (in yellow). The figure shows a reduced sensitivity of the qubit transition energy to changes in the offset charge in the transmon regime $E_J \gg E_C$. (b) The relative variation of the transition energy between the ground and the first excited state decreases exponentially with increasing ratio E_J/E_C.

Just like for the Cooper pair box, one can simply extend the transmon Hamiltonian (7) to include coupling between the qubit and an external capacitively coupled drive voltage V_e. The additional interaction term in the Hamiltonian is again proportional to $V_e\hat{n}$ with the proportionality constant depending on the charging energy of the qubit and the capacitance coupling it to the voltage source. After substituting for $\hat{n}$ from Eq. (6b) and expressing the ladder operators in the transmon eigenstate basis using Eq. (8), we obtain a multilevel generalization of the Hamiltonian given in Eq. (4)

$$\hat{H} = \hbar \sum_{n=0}^{\infty} \omega_{qn} |n\rangle\langle n| + \hbar \sum_{n=0}^{\infty} (\lambda_n \Omega_x |n\rangle\langle n+1| + \text{h.c.}). \tag{9}$$

The quantity $\Omega_x = (8E_C^3 E_J)^{1/4} C_e V_e/\hbar e$ represents the drive strength and is proportional to the voltage V_e. In writing this Hamiltonian, we also neglect the matrix elements λ_{mn} of $\hat{b}$ with $|m-n| \neq 1$ as they tend to zero in the limit $E_J \gg E_C$ and denote the remaining coupling terms $\lambda_{n,n+1}$ between neighbouring states simply by λ_n.

Although the drive Ω_x is real-valued, which might seem to be a limitation for the controllability of the qubit, it can be made effectively complex by going to a rotating frame and using the so-called *rotating wave approximation*. Suppose the drive is a quickly oscillating function of time given by $\Omega_x(t) = \Omega(t)\cos(\omega t + \phi)$ where the envelope function $\Omega(t)$ changes slowly in comparison to ω. The state vector in the frame rotating at the drive frequency ω is defined as $|\Psi_r\rangle = \hat{U}|\Psi\rangle$, where $\hat{U} = \exp(\mathrm{i}\omega t \sum_n n|n\rangle\langle n|)$. It is straightforward to show that its evolution is governed by the effective rotating frame Hamiltonian

$$\hat{H}_r = \hat{U}\hat{H}\hat{U}^\dagger + \mathrm{i}\hbar \frac{\mathrm{d}\hat{U}}{\mathrm{d}t}\hat{U}^\dagger.$$

The second term on the right-hand side of this formula arises due to the time-dependence of the transformation and is equal to $-\hbar\omega\sum_n n|n\rangle\langle n|$. It corresponds to a shift of the effective qubit frequency from ω_q to $\delta_q = \omega_q - \omega$.

The unitary transformation $\hat{U}$ acting on the Hamiltonian given in Eq. (9) results in multiplication of the operators $|n\rangle\langle n+1|$ by $\mathrm{e}^{-\mathrm{i}\omega t}$ and $|n+1\rangle\langle n|$ by $\mathrm{e}^{\mathrm{i}\omega t}$. The cosine factor from $\Omega_x(t)$ multiplied by $\mathrm{e}^{\pm\mathrm{i}\omega t}$ yields a sum of two terms – one of them constant and the other oscillating with frequency 2ω. Since the timescale of the qubit evolution in the rotating frame is basically set by $\omega_q - \omega$ and Ω, the oscillating term can be neglected if $2\omega \gg |\omega_q - \omega|, |\Omega|$ (the rotating wave approximation). In this way $\Omega_x(t)\mathrm{e}^{\pm\mathrm{i}\omega t}$ is replaced by $\Omega(t)\mathrm{e}^{\mp\mathrm{i}\phi}/2$ and after defining a *complex* drive $\tilde{\Omega}(t) = \Omega(t)\mathrm{e}^{-\mathrm{i}\phi}$, we arrive at the final form of the rotating frame Hamiltonian

$$\hat{H}_r = \hbar\sum_{n=0}^{\infty}\delta_{qn}|n\rangle\langle n| + \frac{1}{2}\hbar\sum_{n=0}^{\infty}(\lambda_n\tilde{\Omega}^*|n\rangle\langle n+1| + \text{h.c.}). \tag{10}$$

In summary, this procedure, illustrated in Fig. 6, allows one to replace the Hamiltonian (9) by a Hamiltonian of the same form but with the drive being complex rather than just real. The effective qubit transition energy is in this frame adjustable by changing the detuning δ_q between the drive and the qubit frequency.

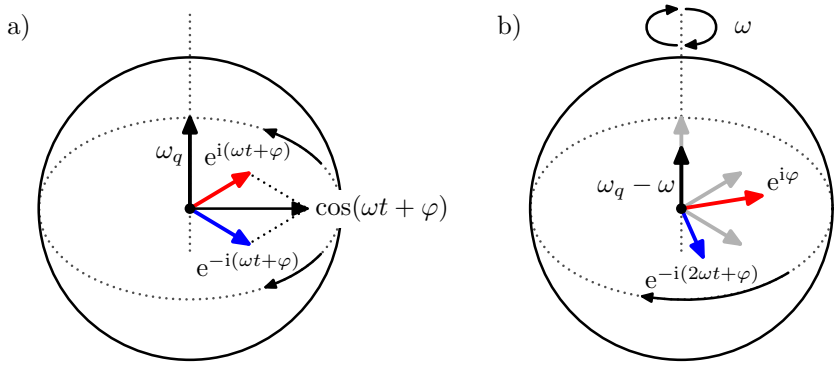

Figure 6: Illustration of the rotating wave approximation. (a) A harmonic signal proportional to $\cos(\omega t+\varphi)$ is coupled to a qubit with transition frequency ω_q. The real harmonic drive can be decomposed into two complex rotating waves proportional to $\mathrm{e}^{\mathrm{i}(\omega t+\varphi)}$ (red) and $\mathrm{e}^{-\mathrm{i}(\omega t+\varphi)}$ (blue). (b) In a frame rotating at the frequency ω around the z-axis the corotating wave (red) is constant in time while the counterrotating wave (blue) varies with frequency 2ω and can be neglected. Due to the transformation into a time-dependent frame, an additional term needs to be added to the Hamiltonian which reduces the effective qubit transition frequency by ω.

2.2 Circuit QED

One of the essential ingredients for quantum information processing is efficient and controllable coupling between qubits. Although this is in principle achievable using direct

qubit-qubit interactions, such a simple approach usually requires the coupled systems to be spatially close which may pose difficulties for scaling the device. For this reason, coupling mechanisms relying on non-local interactions mediated by mobile or spatially extended physical systems are preferred.

Such a mediator of interactions between qubits can be for instance a collective motional degree of freedom of the qubits like in ion-trap experiments [8], real photons that couple distant atoms [30] or virtual photons to couple superconducting qubits [13]. Here we will focus on the coupling between superconducting qubits due to exchange of virtual microwave photons through a transmission line resonator.

The qubits are embedded in an electromagnetic resonator consisting of a coplanar waveguide of finite length – a superconducting strip separated by a gap from a ground plane at each side (see Fig. 7). The one-dimensional nature of the resonator, which confines the electromagnetic field to a smaller volume than in a three-dimensional resonant cavity, leads to larger intensities of the field and consequently to a stronger coupling between the resonator and the qubits. The interactions between the qubits and photons are described by the theory of *circuit quantum electrodynamics* [11]. As shown in Ref. [13], the strong coupling can be used to coherently exchange quantum information between qubits in a controlled way.

The length L of the resonator is much larger than its transverse dimensions which allows it to be treated as a quasi-one-dimensional system supporting a number of discrete electromagnetic field modes. In a lumped element approach, it can be viewed as an electrical circuit composed of a chain of infinitesimal ideal capacitances and inductances, as shown in Fig. 8a. As we almost exclusively deal with situations where the qubits are far detuned from all but one of the resonator modes, we can further approximate the resonator as a simple LC circuit.

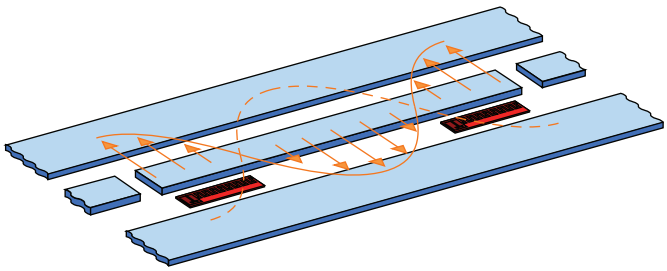

Figure 7: Circuit QED architecture. The coplanar transmission line resonator (in blue) supports a standing electromagnetic wave whose electric field (schematically shown by orange arrows) couples the qubits (in red) placed inside the resonator.

The LC circuit can be treated as a harmonic oscillator. Once again, we can employ the analogy with the mechanical case and by noting that the charge Q, magnetic flux Φ, inductance L and capacitance C correspond to position, momentum, mass and the combination $1/m\omega^2$, respectively, we can immediately write down relations between the

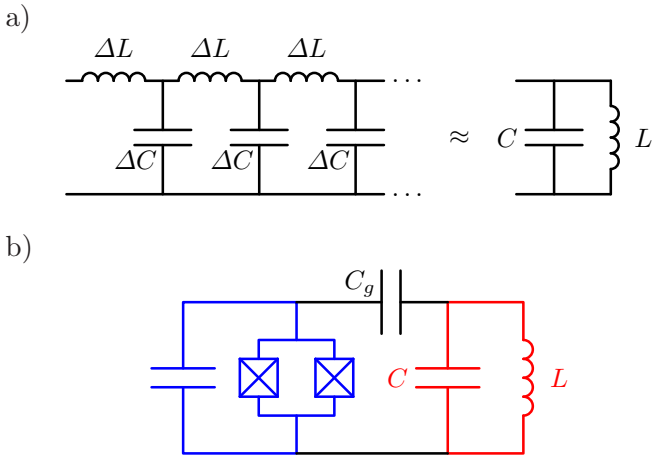

Figure 8: The resonator and its coupling to the qubit. (a) The resonator as a chain of inductances and capacitances and its approximation by a simple LC circuit. (b) The qubit (in blue) is coupled to the resonator (in red) through a gate capacitance C_g.

Hamiltonian, the ladder operators $\hat{a}, \hat{a}^\dagger$ and the operators $\hat{Q}$ and $\hat{\Phi}$

$$\hat{H} = \hbar \overbrace{\sqrt{\frac{1}{LC}}}^{\omega_r} \left(\hat{a}^\dagger \hat{a} + \frac{1}{2} \right), \tag{11a}$$

$$\hat{Q} = \sqrt{\frac{\hbar \omega_r C}{2}} (\hat{a}^\dagger + \hat{a}), \tag{11b}$$

$$\hat{\Phi} = \mathrm{i} \sqrt{\frac{\hbar \omega_r L}{2}} (\hat{a}^\dagger - \hat{a}). \tag{11c}$$

This seemingly crude approximation by a harmonic oscillator is in fact not too far away from the truth. When the electromagnetic field inside the resonator is quantized properly [11], one finds that each of its individual modes behaves indeed as an isolated harmonic oscillator. If we analyzed the resonator in this way and only made the single-mode approximation afterwards, we would arrive at a result identical in its form to Eqs. (11). If more than just one mode is relevant, the expressions on the right-hand side of Eqs. (11) are simply replaced by sums of the corresponding terms for the different modes. We will now restrict ourselves to only one mode and one qubit, knowing that the resulting Hamiltonian can be readily generalized to multiple modes and qubits.

2.2.1 The Jaynes-Cummings Hamiltonian

If the qubit is capacitively coupled to the resonator, as depicted in Fig. 8b, we can view the resonator LC circuit as a source of a quantum drive voltage $\hat{Q}/C = \sqrt{\hbar\omega_r/2C}(\hat{a}^\dagger + \hat{a})$ applied to the qubit. We use Eq. (9), add the resonator energy term given by Eq. (11a)

and replace Ω_x, which is proportional to the voltage, by $g(\hat{a}^\dagger + \hat{a})$. Here the coupling constant g incorporates the proportionality coefficients between Ω_x, the voltage and $\hat{a}^\dagger + \hat{a}$.

Since we are now describing the composite system within the tensor product of the qubit and resonator Hilbert spaces, we will from now on denote the qubit and resonator states and operators respectively with subscripts q and r (e.g. $|m_q, n_r\rangle$, $|n\rangle\langle n|_q$ or $\hat{a}_r$). Alternatively, we can sometimes distinguish between them by using the letters g, e and f for the three lowest qubit states and numbers for the resonator states (e.g. $|e, 3\rangle$).

Out of the four types of coupling terms $\hat{a}_r^\dagger|n+1\rangle\langle n|_q$, $\hat{a}_r^\dagger|n\rangle\langle n+1|_q$, $\hat{a}_r|n+1\rangle\langle n|_q$ and $\hat{a}_r|n\rangle\langle n+1|_q$ arising in the Hamiltonian, the first and the last one are in a sense "less energy-conserving" than the remaining two. In the interaction picture, they oscillate at a frequency given by the sum of the qubit and resonator frequencies whereas the other terms oscillate at the frequency difference. Just like in the case of a classical harmonic drive, one can make the rotating wave approximation and if $g, |\omega_q - \omega_r| \ll \omega_r$, neglect the terms $\hat{a}_r^\dagger|n+1\rangle\langle n|_q$ and $\hat{a}_r|n\rangle\langle n+1|_q$.

The result is the well-known *Jaynes-Cummings Hamiltonian* [31]

$$\hat{H} = \hbar\sum_{n=0}^{\infty}\omega_{qn}|n\rangle\langle n|_q + \hbar\omega_r\hat{a}_r^\dagger\hat{a}_r + \hbar g\sum_{n=0}^{\infty}(\lambda_n\hat{a}_r^\dagger|n\rangle\langle n+1|_q + \text{h.c.}). \tag{12}$$

Thanks to the rotating wave approximation, the interaction term can move excitations between the qubit and the resonator but leaves their total number unchanged. In other words, the operator $\hat{N} = \hat{a}_r^\dagger\hat{a}_r + \sum_n n|n\rangle\langle n|_q$ which counts the total number of excitations commutes with the Hamiltonian (12).

In particular, if the qubit has only two levels $|g\rangle$ and $|e\rangle$, the form of the Hamiltonian becomes very simple. For any n it only couples the state $|e, n\rangle$ to $|g, n+1\rangle$. The resulting structure (illustrated in Fig. 9a), in which the Hilbert space decomposes into two-dimensional decoupled subspaces, is commonly referred to as the *Jaynes-Cummings ladder*.

In this case, the Hamiltonian can be exactly diagonalized by performing a unitary transformation acting separately on each subspace, which can be formally written as

$$\hat{U} = \exp\left(\frac{1}{2}\vartheta(\hat{N})(\hat{a}^\dagger|g\rangle\langle e| - \hat{a}|e\rangle\langle g|)\right),$$

where $\vartheta(\hat{N}) = \arctan(2g\hat{N}^{1/2}/(\omega_r - \omega_q))/\hat{N}^{1/2}$. The transformed Hamiltonian then is

$$\hat{U}\hat{H}\hat{U}^\dagger = \hbar\omega_q|e\rangle\langle e| + \hbar\omega_r\hat{a}^\dagger\hat{a} - \hbar\chi(\hat{N})(|e\rangle\langle e| - |g\rangle\langle g|), \tag{13}$$

$$\text{where } \chi(\hat{N}) = \frac{\omega_r - \omega_q}{2}\left(\sqrt{\frac{4g^2\hat{N}}{(\omega_r - \omega_q)^2} + 1} - 1\right).$$

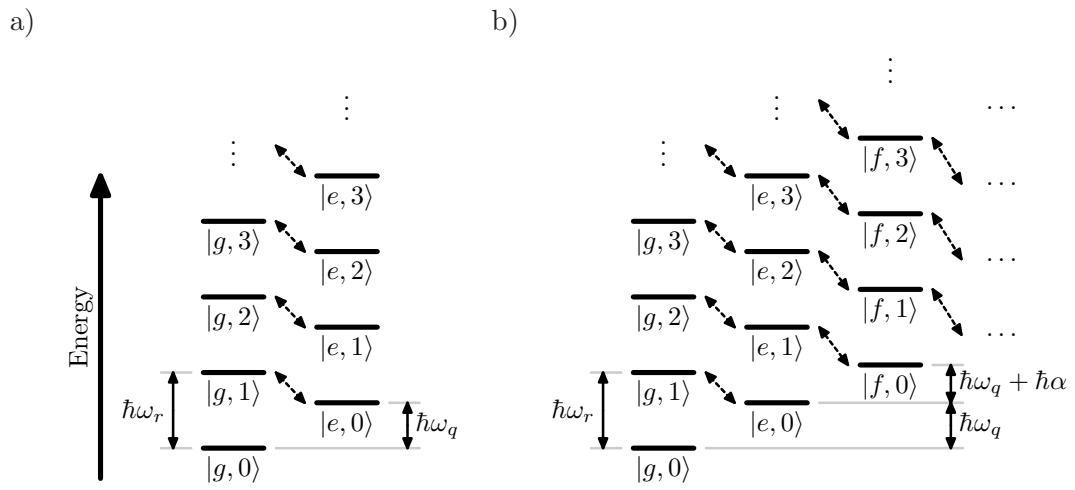

Figure 9: (a) The Jaynes-Cummings ladder for a two-level system interacting with an electromagnetic mode. The qubit levels are marked by letters (g for the ground and e for the excited state) to avoid confusion with the numbered Fock states of the resonator. The Jaynes-Cummings Hamiltonian only couples states within the same two-dimensional excitation manifold. (b) The Jaynes-Cummings ladder for a transmon. The individual excitation manifolds grow in size due to the multilevel structure of the qubit.

The first two terms are simply the decoupled qubit and resonator energies while the third term describes shifts of eigenenergies due to the Jaynes-Cummings coupling. The eigenstates related to $|g, n+1\rangle$ by the unitary transformation above get their energies shifted by $\hbar\chi(n+1)$ whereas the states obtained by transforming $|e, n\rangle$ undergo a shift of the same magnitude but opposite sign.

In the case of a multilevel qubit, the Hamiltonian (12) still conserves the total number $\hat{N}$ of excitations in the system but the decoupled subspaces grow in size with increasing $\hat{N}$ (see Fig. 9b) since there is an ever increasing number of ways in which the excitations can be distributed between the resonator and the qubit. As a consequence, the Hamiltonian cannot be diagonalized exactly and approximate or numerical methods need to be used to find its eigenstates and eigenenergies.

2.2.2 The dispersive regime

The Jaynes-Cummings Hamiltonian can be approximately diagonalized in the so-called *dispersive limit* [11] when $2g\hat{N}^{1/2}/|\omega_r - \omega_q| \ll 1$, regardless of whether the qubit is a two-level system or not. Let us first look at the two-level case as the dispersive limit can then be very simply derived from the exact result given by Eq. (13).

First of all, note that the condition $2g\hat{N}^{1/2}/|\omega_r - \omega_q| \ll 1$ depends on $\hat{N}$ and can therefore be satisfied only in a finite subspace of the whole Hilbert space with the number of excitations not exceeding certain critical number given by $n_{\mathrm{crit}} = (\omega_r - \omega_q)^2/4g^2$. Moreover,

for the dispersive limit to be valid at all, the critical number needs to satisfy $n_{\mathrm{crit}} \gg 1$. Otherwise the approximation is only applicable to the zero-excitation manifold and thus not very useful. If the inequality above holds the unitary transformation parameter $\vartheta(\hat{N})$ as well as the energy shift $\chi(\hat{N})$ can be expanded to lowest order in $\hat{N}$ which yields

$$\hat{U}_{\mathrm{disp}} = \exp\left(\frac{g}{\omega_r - \omega_q}(\hat{a}^\dagger|g\rangle\langle e| - \hat{a}|e\rangle\langle g|)\right), \tag{14}$$

$$\hat{H}_{\mathrm{disp}} = \hat{U}_{\mathrm{disp}}\hat{H}\hat{U}^\dagger_{\mathrm{disp}} = \hbar\omega_q|e\rangle\langle e| + \hbar\omega_r\hat{a}^\dagger\hat{a} - \hbar\frac{g^2\hat{N}}{\omega_r - \omega_q}(|e\rangle\langle e| - |g\rangle\langle g|).$$

If we express $\hat{N}$ in terms of the qubit and resonator operators the interaction term becomes easy to interpret. We obtain

$$\hat{H}_{\mathrm{disp}} = \hbar\left(\omega_q + \frac{g^2}{\omega_q - \omega_r}\right)|e\rangle\langle e| + \hbar\left(\omega_r + \frac{g^2}{\omega_q - \omega_r}(|e\rangle\langle e| - |g\rangle\langle g|)\right)\hat{a}^\dagger\hat{a}. \tag{15}$$

The qubit frequency is shifted by $\chi = g^2/(\omega_q - \omega_r)$ while the resonator frequency undergoes a *dispersive shift* by $\pm\chi$ depending on the state of the qubit. This point of view where ω_r is qubit-dependent is of course not the only one possible. The terms in Eq. (15) can be rearranged into a form where ω_r is unchanged and the qubit frequency is shifted by $(2\hat{a}^\dagger\hat{a}+1)\chi$. This effect can be understood as an AC Stark shift of the qubit induced by the resonator field.

Although both of these standpoints are equally valid and interchangeable we will further adopt the first one since it allows more natural treatment of the processes we are about to study.

The Hamiltonian (12) of a multilevel transmon qubit interacting with the resonator mode can be diagonalized to first order in the parameter $g/(\omega_r - \omega_q)$ by a unitary transformation which is a straightforward generalization of the two-level case given by Eq. (14), namely [27]

$$\hat{U}_{\mathrm{disp}} = \exp\left(\sum_{n=0}^{\infty} g\eta_n(\hat{a}_r^\dagger|n\rangle\langle n+1|_q - \mathrm{h.c.})\right). \tag{16}$$

The coefficients η_n need to be chosen so as to eliminate the energy exchange terms $\hat{a}_r^\dagger|n\rangle\langle n+1|$ and $\hat{a}_r|n+1\rangle\langle n|$ from $\hat{H}_{\mathrm{disp}}$ to first order in $g/(\omega_r - \omega_q)$. Using the operator identity $\exp(\hat{A})\hat{H}\exp(-\hat{A}) = \hat{H} + [\hat{A},\hat{H}] + \frac{1}{2}[\hat{A},[\hat{A},\hat{H}]] + \ldots$ truncated at second order in the dispersive transformation generator $\hat{A}$, we first calculate

$$[\hat{A},\hat{H}] = \hbar\sum_{n=0}^{\infty} g\eta_n(\omega_{q,n+1} - \omega_{qn} - \omega_r)(\hat{a}_r^\dagger|n\rangle\langle n+1|_q + \mathrm{h.c.}) + \mathcal{O}(g^2),$$

which implies that the desired cancellation can be achieved if $\eta_n(\omega_{q,n+1} - \omega_{qn} - \omega_r) = -\lambda_n$.

This particular choice of η_n then yields

$$\begin{aligned}\hat{H}_{\text{disp}} =&\hbar\sum_{n=0}^{\infty}\omega_{qn}|n\rangle\langle n|_q + \hbar\omega_r\hat{a}_r^\dagger\hat{a}_r + \hbar g^2\sum_{n=0}^{\infty}\lambda_n\eta_n(\hat{a}_r^\dagger\hat{a}_r|n\rangle\langle n|_q - \hat{a}_r\hat{a}_r^\dagger|n+1\rangle\langle n+1|_q)\\ &+\frac{1}{2}\hbar g^2\sum_{n=0}^{\infty}(\lambda_n\eta_{n-1}-\lambda_{n-1}\eta_n)(\hat{a}_r^\dagger\hat{a}_r^\dagger|n-1\rangle\langle n+1|_q + \text{h.c.}) + \mathcal{O}(g^3).\end{aligned}$$

It can be argued that the term in the second line which transfers two excitations between the qubit and the resonator can be neglected due to the difference $\lambda_n\eta_{n-1} - \lambda_{n-1}\eta_n$ being small for a weakly anharmonic qubit. Within this approximation, the multilevel dispersive Hamiltonian up to second order in g can be expressed as

$$\hat{H}_{\text{disp}} = \hbar\sum_{n=0}^{\infty}(\omega_{qn}+\chi_n)|n\rangle\langle n|_q + \hbar\left(\omega_r - \sum_{n=0}^{\infty}(\chi_{n+1}-\chi_n)|n\rangle\langle n|_q\right)\hat{a}_r^\dagger\hat{a}_r, \tag{17a}$$

$$\text{where } \chi_n = \frac{g^2\lambda_{n-1}^2}{\omega_{qn}-\omega_{q,n-1}-\omega_r} = \frac{g^2 n}{\omega_q+(n-1)\alpha-\omega_r}. \tag{17b}$$

The last expression for χ_n is derived by plugging in the approximate value of $\lambda_{n-1} = \sqrt{n}$ and the frequencies ω_{qn} and $\omega_{q,n-1}$ in terms of the qubit transition frequency ω_q and its anharmonicity α.

The result for a multilevel qubit is thus qualitatively identical to what we obtained for a purely two-level qubit. Once again, the qubit energy levels are renormalized by qubit-resonator interactions and the resonator frequency is shifted by an amount depending on the qubit state. In particular, the frequencies of the resonator for the $|e\rangle$ and $|g\rangle$ qubit states differ by

$$\omega_r^{(e)} - \omega_r^{(g)} = 2\chi_1 - \chi_2.$$

In comparison with the value $2\chi_1$ we got for a two-level qubit, the resonator frequency difference for a multilevel qubit is in general lower[2] since the quantity χ_2 typically has the same sign as χ_1 and is comparable in magnitude. In fact, it is obvious from Eq. (17b) that χ_2 is very close to $2\chi_1$ if $|\alpha| \ll |\omega_r - \omega_q|$ and consequently, the resonator energy difference for a transmon is significantly smaller than for a two-level qubit. This reduction in the dispersive shift can be qualitatively understood in terms of energy level repulsion, as shown in Fig. 10.

Let us now look at how the dispersive Hamiltonian changes when a second qubit is added and an external drive is applied to the resonator. We assume that both qubits are capacitively coupled to the resonator and that there is no direct interaction between them. To distinguish between the two qubits, we will denote them as A and B and mark their respective parameters by a subscript.

[2]It has been shown in Ref. [27] that there is a (so-called *straddling*) regime where the dispersive shift is enhanced instead of reduced. However, entering this regime while staying in the dispersive limit turns out to be rather difficult.

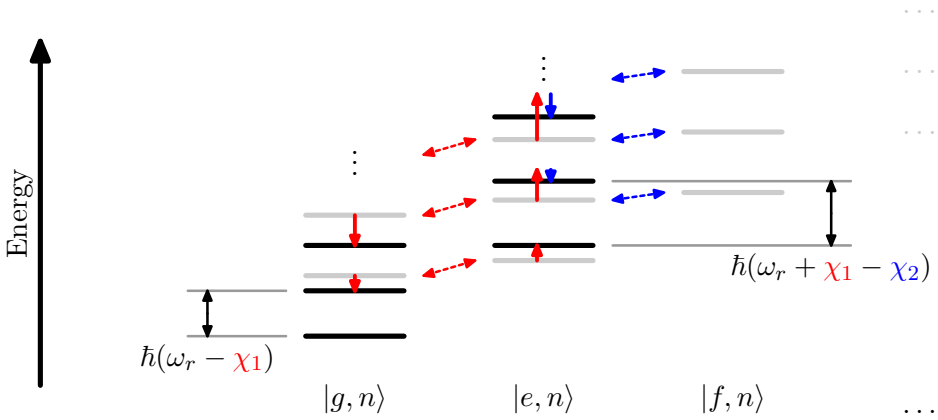

Figure 10: Resonator dispersive shift by a multilevel qubit. The shift can be viewed as a result of level repulsion of the bare energy levels (in grey) – the energies of states $|g,n\rangle$ move to lower values (in the depicted case $\omega_q > \omega_r$) due to their coupling to states $|e,n\rangle$ (red arrows). This coupling also lifts the energies of $|e,n\rangle$ by the same amount χ_1. But unlike in the two-level case, these levels are in addition lowered by their couplings to states $|f,n\rangle$ (blue arrows), which reduces the total energy shift by χ_2. The resulting dressed energy levels are shown in black.

The Jaynes-Cummings Hamiltonian given by Eq. (12) is modified by adding an energy term and a resonator coupling term for the second qubit. These are completely analogous to the two infinite sums in the one-qubit Hamiltonian. One can show that a drive voltage capacitively coupled to the transmission line resonator can be described by a term of the form $\hbar\varepsilon_x(t)(\hat{a}_r^\dagger + \hat{a}_r)$, where $\varepsilon_x(t)$ is a drive strength proportional to the voltage. In summary, the Jaynes-Cummings Hamiltonian takes the form

$$\begin{aligned}\hat{H} =& \hbar \sum_{i=A,B} \sum_{n=0}^{\infty} \omega_{in} |n\rangle\langle n|_i + \hbar\omega_r \hat{a}_r^\dagger \hat{a}_r + \hbar \sum_{i=A,B} \sum_{n=0}^{\infty} g_i(\lambda_{in} \hat{a}_r^\dagger |n\rangle\langle n+1|_i + \text{h.c.}) \\ &+ \hbar\varepsilon_x(t)(\hat{a}_r^\dagger + \hat{a}_r). \end{aligned} \tag{18}$$

The dispersive transformation has the same form as in Eq. (16) except that the argument of the exponential now consists of a sum of the corresponding terms for both qubits. After performing the expansion outlined above for the one-qubit case, one obtains the

approximate dispersive Hamiltonian

$$\begin{aligned}\hat{H}_{\text{disp}} =& \hbar \sum_{i=A,B} \sum_{n=0}^{\infty} (\omega_{in} + \chi_{in}) |n\rangle\langle n|_i + \hbar \left(\omega_r - \sum_{i=A,B} \sum_{n=0}^{\infty} (\chi_{i,n+1} - \chi_{in}) |n\rangle\langle n|_i \right) \hat{a}_r^\dagger \hat{a}_r \\ & - \hbar g_A g_B \sum_{m,n=0}^{\infty} (\eta_{Am} \sqrt{n+1} + \eta_{Bn} \sqrt{m+1}) (|m_A, n+1_B\rangle\langle m+1_A, n_B| + \text{h.c.}) \\ & + \hbar \varepsilon_x(t) (\hat{a}_r^\dagger + \hat{a}_r) \left[1 - \frac{1}{2} \sum_{i=A,B} \sum_{n=0}^{\infty} g_i^2 \left(\eta_{in}^2 - \eta_{i,n-1}^2 \right) |n\rangle\langle n|_i \right] \\ & - \hbar \varepsilon_x(t) \sum_{i=A,B} \sum_{n=0}^{\infty} g_i \eta_{in} (|n\rangle\langle n+1|_i + \text{h.c.}), \end{aligned} \tag{19}$$

where $\eta_{in} = \dfrac{\sqrt{n+1}}{\omega_i + n\alpha_i - \omega_r}$.

The terms in the first line are analogous to those in the one-qubit dispersive Hamiltonian (17a) – the energy levels of each qubit are shifted by χ_{in} given by Eq. (17b) and the dispersive shift of the resonator is simply a sum of contributions from the two qubits. The second line represents an interaction between the qubits mediated by virtual photon exchange through the resonator. This terms has a form similar to that of the Jaynes-Cummings interaction term – it can move excitations between the two qubits. The third line contains the resonator drive term. The drive strength is renormalized by a factor which depends on the qubit state. The last term corresponds to the external signal $\varepsilon_x(t)$ driving the qubits indirectly via the cavity.

The dispersive regime therefore offers a way of driving the qubit alternative to the direct drive described in Eq. (9). If the drive frequency is close to the qubit transition frequency but far detuned from the resonator frequency then the signal can efficiently drive the qubit while only weakly affecting the resonator which in this process acts merely as a mediating channel.

Note that the indirect drive term does not have the same form as the direct drive term in Eq. (9) where the operators $|n\rangle\langle n+1|$ are multiplied by $\lambda_n = \sqrt{n+1}$. This coefficient is in the indirect drive case replaced by $g\eta_n$ which depends on the detuning of the particular $n \leftrightarrow n+1$ transition from the resonator frequency. Not surprisingly, the transitions whose frequencies are closer to the resonator frequency are in this case driven more strongly than if the drive is applied directly to the qubit.

For comparison, as well as for completeness, and in order to better elucidate the aspects of the dispersive Hamiltonian which might get obscured by the multilevel structure of

the transmon qubit, we also present the dispersive Hamiltonian [11] for a two-level qubit

$$\begin{aligned}\hat{H}_{\text{disp}} =& \hbar \sum_{i=A,B} \left(\omega_i + \frac{g_i^2}{\omega_i - \omega_r}\right) |e\rangle\langle e|_i + \hbar \left(\omega_r + \sum_{i=A,B} \frac{g_i^2}{\omega_i - \omega_r}(|e\rangle\langle e|_i - |g\rangle\langle g|_i)\right) \hat{a}_r^\dagger \hat{a}_r \\ & - \hbar g_A g_B \left(\frac{1}{\omega_A - \omega_r} + \frac{1}{\omega_B - \omega_r}\right) (|g_A, e_B\rangle\langle e_A, g_B| + \text{h.c.}) \\ & + \hbar \varepsilon_x(t)(\hat{a}_r^\dagger + \hat{a}_r) \left[1 - \frac{1}{2} \sum_{i=A,B} \left(\frac{g_i}{\omega_i - \omega_r}\right)^2 (|g\rangle\langle g|_i - |e\rangle\langle e|_i)\right] \\ & - \hbar \varepsilon_x(t) \sum_{i=A,B} \frac{g_i}{\omega_i - \omega_r} (|g\rangle\langle e|_i + \text{h.c.}). \end{aligned} \tag{20}$$

Just like in the case of a direct qubit drive discussed in Section 2.1.3, rotating wave approximation can be used to replace a real harmonic drive $\varepsilon_x(t) = \varepsilon(t)\cos(\omega t + \phi)$ with slowly varying amplitude $\varepsilon(t)$ by $\tilde{\varepsilon}(t)/2$ where $\tilde{\varepsilon}(t) = \varepsilon(t)\mathrm{e}^{\mathrm{i}\phi}$ is the complex drive strength. At the same time, transformation into a frame rotating at the drive frequency ω given by the unitary operation $\exp(\mathrm{i}\omega t(\hat{a}^\dagger \hat{a} + \sum_{n,i} |n\rangle\langle n|_i))$ results in replacement of all the frequencies ω_A, ω_B and ω_r by the corresponding detunings δ_A, δ_B and δ_r from the drive frequency.

The dispersive approximation is a useful tool allowing the qubit and the resonator to be treated as two system which do not exchange energy but only couple together by shifting each other's energy levels. The viewpoint in which the resonator is seen as an isolated harmonic oscillator with qubit-dependent frequency and drive strength is particularly convenient for understanding the mechanism of *dispersive readout* and plays a key role in the geometric phase measurement described in this thesis.

2.3 Dispersive readout and Qubit tomography

Apart from mediating interaction between qubits, the resonator in the dispersive regime can also serve as a measurement channel for *quantum non-demolition readout* of the qubits. The resonator is equipped with an output port connected to a series of amplifiers, allowing to measure the electromagnetic field inside. By probing the resonator with a drive signal, its transmission characteristic can be obtained as a function of frequency.

Within the previously introduced simplified model describing the resonator as an LC circuit, the measurement setup can be represented by the circuit diagram shown in Fig. 11. The photons leaking out of the resonator are absorbed and detected. This dissipative process is modelled by the resistance R. The measured signal is then proportional to the output current I_{out}.

If the resonance curve of the LC circuit is sufficiently narrow so that the frequency dependence of the impedances Z_{in} and Z_{out} can be neglected, then the frequency response

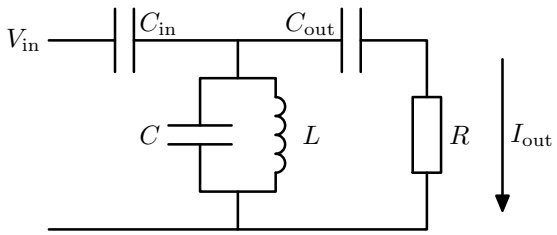

Figure 11: Circuit diagram of resonator response measurement. A drive signal is applied to the resonator (LC circuit). The signal transmitted from the input to the output port is amplified and measured to obtain the transmission characteristics of the resonator.

of the circuit is given by a Lorentzian function centered around the resonant frequency.

As discussed above, the Jaynes-Cummings type interaction between the resonator and the qubit in the dispersive limit leads to a shift of the resonator frequency depending on the state of the qubit. Therefore, information about the qubit state can be inferred from the measured shift of the resonator response curve.

Fig. 12 illustrates how the two qubit states can be distinguished by measuring the steady-state resonator response at a fixed frequency. The differing detunings between the drive and the resonator frequency translate into different powers of the transmitted signal. Alternatively, the measurement can be also based on observing the phase shift of the transmitted field rather than its amplitude.

Although the frequency of the probe signal can be in principle arbitrary as depicted in Fig. 12, it is usually chosen to coincide with one of the resonant frequencies $\omega_r^{(g)}$, $\omega_r^{(e)}$ for convenience. The procedure can be obviously generalized to multiple qubits provided that the individual resonance peaks are well enough separated to be resolved.

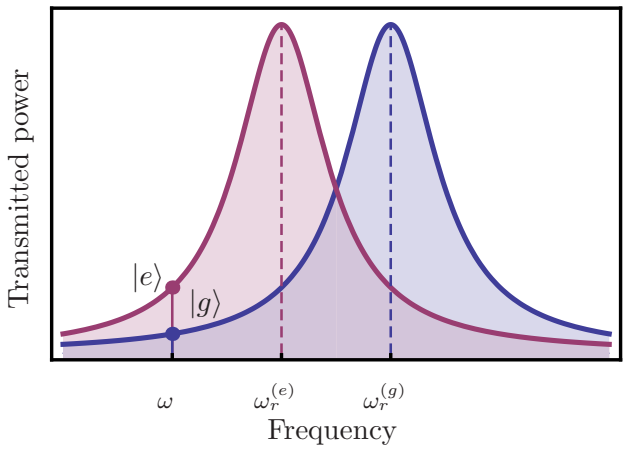

Figure 12: Resonator transmission in a continuous dispersive measurement. The power of the transmitted probe signal at a fixed frequency ω depends on its detuning from the resonator frequency and on the state of the qubit due to the dispersive shift.

The presented picture of the dispersive readout, although illustrative, is somewhat simplistic since it only covers the stationary response case and neglects effects of the resonator-mediated qubit drive. To provide a better model of the resonator response applicable also to the more general case of a time-dependent drive, the evolution equation of the system needs to be solved. As the resonator is now subject to dissipation and the system is thus no longer in a pure state, it has to be described within the mixed state formalism. The equation governing the time evolution of its density matrix $\hat{\rho}$ is the *quantum master equation* [32] which in general has the form

$$\frac{\mathrm{d}\hat{\rho}}{\mathrm{d}t} = -\frac{\mathrm{i}}{\hbar}[\hat{H}, \hat{\rho}] + \frac{1}{2}\sum_m \Gamma_m(\hat{L}_m\hat{\rho}\hat{L}_m^\dagger - \hat{L}_m^\dagger\hat{L}_m\hat{\rho} - \hat{\rho}\hat{L}_m^\dagger\hat{L}_m), \tag{21}$$

where Γ_m are non-negative constants and $\hat{L}_m$ are the so-called *Lindblad operators* describing the non-unitary dynamics associated with dissipation and dephasing. In the case of a dispersively coupled two-level qubit and a resonator, $\hat{H}$ is the dispersive Hamiltonian given by Eq. (20) and there are three Lindblad operators $\hat{L}_1 = \hat{a}_r$, $\hat{L}_2 = |g\rangle\langle e|_q$ and $\hat{L}_3 = |e\rangle\langle e|_q$ with the corresponding coefficients commonly denoted as $\Gamma_1 = \kappa$, $\Gamma_2 = \Gamma$ and $\Gamma_3 = \Gamma_\phi$. These terms represent resonator dissipation, qubit dissipation and qubit dephasing, respectively.

To solve the quantum master equation numerically, one can start by choosing a suitable set of operators $\hat{A}$ and considering the evolution equations for their expectation values

$$\frac{\mathrm{d}\langle\hat{A}\rangle}{\mathrm{d}t} = \frac{\mathrm{i}}{\hbar}\langle[\hat{H}, \hat{A}]\rangle + \frac{1}{2}\sum_m \Gamma_m(\langle\hat{L}_m^\dagger\hat{A}\hat{L}_m\rangle - \langle\hat{L}_m^\dagger\hat{L}_m\hat{A}\rangle - \langle\hat{A}\hat{L}_m^\dagger\hat{L}_m\rangle).$$

This step in general results in a system of infinitely many coupled differential equations because an equation for any given expectation value involves expectation values of even higher order in the ladder operators. To render the system finite, an approximation can be employed whereby higher-order expectation values are factored into products of lower-order ones, e.g. $\langle\hat{a}_r^\dagger\hat{a}_r|e\rangle\langle g|_q\rangle \approx \langle\hat{a}_r^\dagger\hat{a}_r\rangle\langle|e\rangle\langle g|_q\rangle$, $\langle\hat{a}_r^\dagger\hat{a}_r\hat{a}_r|e\rangle\langle e|_q\rangle \approx \langle\hat{a}_r^\dagger\hat{a}_r\rangle\langle\hat{a}_r|e\rangle\langle e|_q\rangle$ etc. In this way, the original master equation can be approximated by the so-called *cavity Bloch equations* [14] – a set of eight differential equations for the expectation values of the eight operators $\hat{a}_r$, $\hat{a}_r^\dagger\hat{a}_r$, $|e\rangle\langle e|_q$, $|e\rangle\langle g|_q$, $|g\rangle\langle e|_q$, $\hat{a}_r|e\rangle\langle e|_q$, $\hat{a}_r|e\rangle\langle g|_q$ and $\hat{a}_r|g\rangle\langle e|_q$.

Once the time evolution of the density matrix is solved, the detected signal which is proportional to the electric field inside the resonator, i.e. to $\hat{a}_r^\dagger + \hat{a}_r$, can be calculated.

Dispersive measurement with time-dependent resonator drive (the so-called *pulsed measurement*) which can be simulated using cavity Bloch equations has several advantages over steady-state continuous probing of the resonator. The drive can be switched on only when the measurement is actually needed and does not have to be on during the qubit manipulation which in turn is not disrupted by the measurement. Consequently, pulsed readout can be performed with higher power and therefore higher signal-to-noise ratio. Also, since the decay rates of the resonator and the qubit are often of the same

order of magnitude, the simpler stationary regime may not be suitable for readout of the final qubit state simply because the qubit relaxes even before the resonator can reach the steady state. In the case of the pulsed measurement, the desired information about the qubit state is encoded in the *dynamical* response of the resonator and cavity Bloch equations can be used to extract this information.

Fig. 13 shows an example of the dynamical resonator response during a pulsed measurement obtained by numerical solution of the cavity Bloch equations with realistic values of the parameters (qubit and resonator frequencies, the dispersive shift and relaxation times). The transmitted power expected for the stationary case from the simple model based on a shift of the Lorentzian transmission profile is shown for comparison. The figure clearly illustrates that as expected, the transmitted signal corresponding to the excited qubit state would only approach the same value as in the continuous measurement in the absence of qubit relaxation. Nevertheless, since the ground state transmission changes on a time scale given by the resonator relaxation time τ whereas the characteristic time for the excited state transmission is the qubit relaxation time T_1, the two dynamical responses are easily distinguishable. This difference can then be indeed used to obtain information about the qubit state at the point when the measurement is switched on.

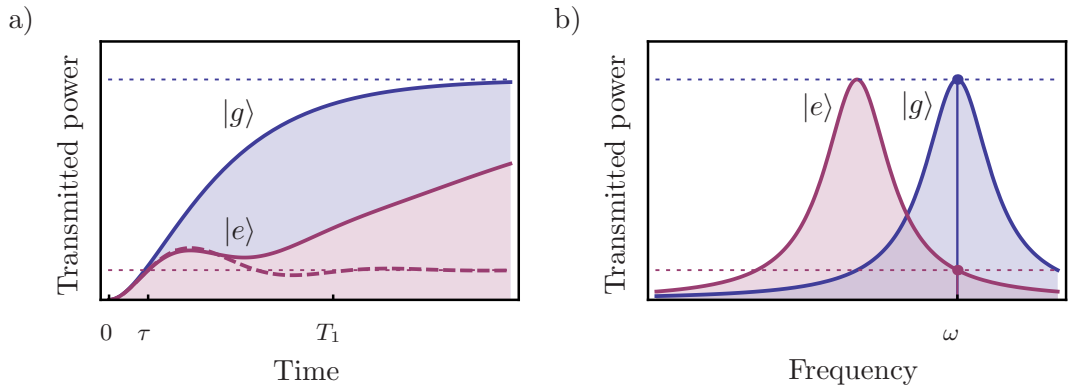

Figure 13: Dynamical resonator transmission in a pulsed dispersive measurement. (a) The power transmitted through the resonator in response to a drive switched on at time $t = 0$. The two signals for the qubits ground (in blue) and excited (in purple) states were obtained by solving the cavity Bloch equations numerically for realistic values of the resonator and qubit relaxation times $\tau \approx 200$ ns and $T_1 \approx 1$ μs, qubit dephasing rate $\gamma = 0$ and dispersive shift $\chi/2\pi \approx 0.7$ MHz. The ground state response and the excited state response in the absence of qubit dissipation (dashed purple line) asymptotically approach values which agree with the simple stationary model based on Lorentzian response curves (b).

Just like any other quantum-mechanical measurement, the dispersive readout also inevitably changes the state of the measured system. However, it does so in a very specific way. If qubit dissipation during the readout process can be neglected then the dispersive measurement can be considered to be *projective* [7]. This special class of processes, upon producing a particular outcome a from the spectrum of the operator $\hat{A}$ representing the measured quantity, projects the state of the system onto the eigenspace corresponding to a. More specifically, the measurement yields the eigenvalue a and changes the density

matrix $\hat{\rho}$ of the system to $\hat{P}_a\hat{\rho}\hat{P}_a$ with probability $p_a = \mathrm{Tr}\,\hat{P}_a\hat{\rho}$, where $\hat{P}_a$ is a projector onto the eigenspace of a.

A projective measurement also obviously preserves the eigenvectors of the measured operator $\hat{A}$, although it reduces general pure superposition states to mixed states. This special property distinguishes projective readout from general measurement processes for which there need not be a complete basis unaffected by the measurement. A simple example of a non-projective process is photodetection – photons registered by the detector are absorbed which means that the only quantum state invariant under this measurement is the vacuum state.

An important subclass of projective measurements are so-called *quantum non-demolition measurements* for which the projectors $\hat{P}_a$ commute with the Hamiltonian. The eigenstates of such a measurement are therefore invariant under the free evolution of the system and the measurement will yield the same result when repeated.

In our case the dispersive qubit readout projects onto the qubit energy eigenstates $|g\rangle$ and $|e\rangle$. If a given qubit state described by a density matrix $\hat{\rho}$ can be prepared and measured repeatedly then the statistics of the measurement outcomes provide an estimate of the probabilities $p_g = \mathrm{Tr}\,|g\rangle\langle g|\hat{\rho}$ and $p_e = \mathrm{Tr}\,|e\rangle\langle e|\hat{\rho}$ to find the qubit in the two eigenstates. This is equivalent to determining the quantity $p_e - p_g = \mathrm{Tr}\,\hat{\sigma}_z\hat{\rho}$, i.e. the expectation value $\langle\hat{\sigma}_z\rangle$ of the Pauli matrix $\hat{\rho}_z$. In the well-known *Bloch vector representation* of the qubit state as $\hat{\rho} = (\mathbb{1} + \hat{\vec{\sigma}}\cdot\vec{n})/2$ this expectation value corresponds to the projection of the vector $\vec{n}$ onto the z-axis, as depicted in Fig. 14a.

The remaining components of the vector can be determined by applying a suitable unitary operation $\hat{U}$ to the qubit prior to measurement. The obtained probability difference $p_e - p_g$ is then equal to $\mathrm{Tr}\,\hat{\sigma}_z\hat{U}\hat{\rho}\hat{U}^\dagger = \langle\hat{U}^\dagger\hat{\sigma}_z\hat{U}\rangle$. By choosing $\hat{U} = \exp(\mathrm{i}\pi\hat{\sigma}_y/4)$ or $\hat{U} = \exp(-\mathrm{i}\pi\hat{\sigma}_x/4)$ the expectation value simplifies to $\langle\hat{\sigma}_x\rangle$ and $\langle\hat{\sigma}_y\rangle$, respectively. The two given unitary operations correspond to rotations of the Bloch vector by $-\pi/2$ around the y-axis and by $\pi/2$ around the x-axis which transform the x and y components of $\vec{n}$ into the measurable z component. The described procedure which allows the Bloch vector to be determined by measuring its three projections separately is for obvious reasons called *qubit tomography* and is schematically outlined in Fig. 14.

Qubit tomography is a useful technique for determining the qubit density matrix. It is a probabilistic process and its result therefore has a non-zero statistical error. However, this uncertainty decreases as $1/\sqrt{N}$ with the number N of measurements and can thus be in principle made arbitrarily small by increasing N.

The method can be also generalized to $n > 1$ qubits. The quantity measured in the dispersive readout then corresponds to some non-trivial combination of the Pauli matrices $\hat{\sigma}_{iz}$ for the individual qubits. By applying $2^{2n} - 1$ different unitary operations before the measurement, one can obtain $2^{2n} - 1$ linearly independent expectation values which can then be used to extract the $2^{2n} - 1$ unknown elements of the $2^n \times 2^n$ density matrix. A more sophisticated way of density matrix reconstruction relies on a maximum

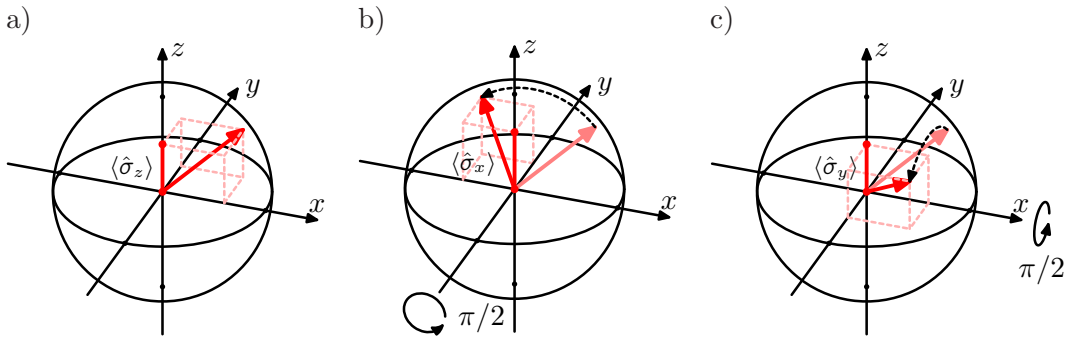

Figure 14: Qubit tomography. (a) Direct dispersive measurement of the qubit state yields the z component of the Bloch vector. Applying rotations by $\pi/2$ around the (b) y and (c) x axis before the readout allows the x and y components to be measured as well.

likelihood fit of the matrix elements. In this way, constraints can be added to avoid unphysical results, e.g. density matrices with negative eigenvalues, which could otherwise arise from a simple solution of the linear equation system for $\hat{\rho}$ due to statistical errors. When using the maximum likelihood method, more than the necessary $2^{2n}-1$ expectation values can be measured. The redundant information then improves the accuracy of the result.

The simple case of one-qubit tomography has been successfully used in an experiment [12] and has since become a standard tool in circuit QED experiments. The two-qubit and three-qubit cases have been demonstrated in Refs. [33] and [34, 35], respectively.

3 Geometric phase

The concept of a geometric phase – a phase accumulated by a quantum system that depends only on the trajectory of the state vector in the Hilbert space – is closely related to *adiabaticity*. It was first described in the context of adiabatic processes by Berry [15] and it was soon discovered to be deeply connected to differential geometry [16].

Adiabatic processes also occur in classical mechanics. Studying them in this context can provide useful insight relevant to the quantum case, as described in Section 3.1.

3.1 Adiabatic limit in classical mechanics

Our experience with the everyday world tells us that objects tend to stay near equilibrium if they are not disturbed too violently. This rather intuitive and vague statement can be made more precise – under very general assumptions, a classical system with a time-dependent Hamiltonian remains in a stationary state if the Hamiltonian varies infinitely slowly. In the special case of periodic systems, this result can be shown to be a rather straightforward consequence of the *action variable* $\oint \vec{p} \cdot \mathrm{d}\vec{q}$ being an *adiabatic invariant* [36]. It remains valid for ergodic processes for which the adiabatic invariant is the phase space volume $\Omega(t)$ enclosed within a constant energy shell [37] characterised by $H(p, q) = E(t)$. In both cases, the adiabatic invariant is zero if and only if the system is in a stationary state.

The notion of an *adiabatic process*, which in its ideal form does not cause deviations from the equilibrium state, can be elucidated using the following real-life analogy. Runners in the popular *egg-and-spoon race* (see Fig. 15a) try to transport the potential energy minimum (the center of the spoon) from its initial position (start) to a given final position (finish) without the egg deviating too much from the equilibrium (falling from the spoon) in the process.

It is rather easy to show that the deviation of the system from equilibrium for this particular example indeed vanishes in the limit of infinitely slow evolution. Let us consider that the runner starts moving instantaneously at $t = 0$, maintains a constant velocity $\vec{v}$ and stops abruptly at the finish line. The egg, initially at rest, starts moving with the velocity $-\vec{v}$ in the reference frame comoving with the runner. As depicted in Fig. 15b, it oscillates around the equilibrium position with the amplitude v/ω, where ω is the angular frequency of its periodic motion in the confining potential (which we assume to be quadratic for simplicity). When the runner stops, the velocity of the egg changes by $+\vec{v}$ and depending on the phase of its periodic motion at this moment, it is left oscillating with an amplitude between 0 and $2v/\omega$. We can see that the maximum deviation from the equilibrium position both during and after the end of the process scales with the ratio v/ω and goes to zero as $v \to 0$.

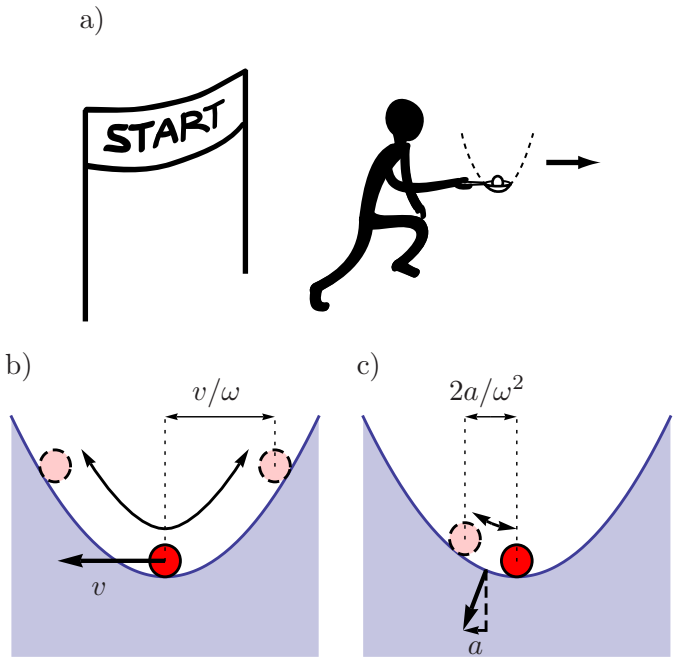

Figure 15: (a) The egg-and-spoon race as an analogy for an adiabatic process. (b) When the runner moves at a constant velocity v changing discontinuously at the start and the finish of the race, the typical deviation of the egg from the equilibrium position is proportional to v/ω. (c) Moving with a constant acceleration a leads to a typical deviation proportional to a/ω^2.

However, as the term egg-and-spoon *race* suggests, going as slowly as possible is not the only way to get the egg across the finish line. Since the source of the egg's motion within the potential well in the described case is obviously the sudden change of the runner's velocity, it might be a good idea to let him/her speed up and slow down gradually. We will consider their acceleration $\vec{a}$ to be constant for a given time after the start, zero for most of the race, then again non-zero, equal to $-\vec{a}$ before the end. As before, we choose to describe the system within the comoving reference frame whose non-inertiality manifests itself in the appearance of a pseudo-force acting on the egg during the runner's acceleration and deceleration. A constant additional force $-m\vec{a}$ causes the equilibrium position inside the confining potential to shift by $\vec{a}/\omega^2$. This shift and the resulting oscillations of the egg around the new equilibrium position with amplitude $\vec{a}/\omega^2$ are shown in Fig. 15c. When the runner stops accelerating the inertial force vanishes and the egg starts moving around the undisturbed potential energy minimum. The amplitude of this motion once again depends on the phase of the egg's oscillations at the moment when the acceleration ends and can range from 0 to $2a/\omega^2$. The motion during the deceleration phase can be analyzed in the same way and the maximum deviation from the equilibrium position after the race is found to be $4a/\omega^2$.

Considering that the minimum acceleration needed to finish a race of length L in total time T scales as L/T^2 whereas the necessary velocity behaves as L/T, we can see that the

maximum deviation from equilibrium is of the order of $L/\omega T$ in the first discussed case with constant velocity and of $L/(\omega T)^2$ for continuously changing velocity and piecewise constant acceleration. Provided that the duration of the race is longer that the period of the egg's oscillations in the spoon, the latter scenario is obviously preferable.

It is relatively easy to see that our assumption of constant acceleration was still not the best choice with regard to adiabaticity. The discontinuity in acceleration causes a *sudden* displacement of the equilibrium position. As we have just seen, performing the displacement gradually rather than instantaneously helps in reducing the amplitude of oscillations around the shifted equilibrium shown in Fig. 15c. Therefore, by making the acceleration continuous in time, the deviation from equilibrium can be lowered to higher than second order in $1/\omega T$.

In fact, there is a direct relation between the asymptotic behaviour of the deviation from equilibrium in the adiabatic limit and differentiability of the equilibrium position. It is not very difficult to show rigorously that for a quadratic potential the *final* amplitude of oscillations around the equilibrium asymptotically behaves as $o(1/T^{k-1})$ for $T \to \infty$ if the position of the runner is a k-times differentiable function of time and all derivatives of order $k-1$ and lower have zero initial and final values. A derivation of this result is presented in Section 4.2 for a quantum oscillator but applies equally well for a classical one.

We should point out that this is a statement about the asymptotic behaviour of the final oscillation amplitude in the adiabatic limit $T \to \infty$ and does not give us any actual comparison between these amplitudes for two evolutions of the Hamiltonian with different degrees of differentiability and a finite time T. A smoother evolution does not necessarily imply better adiabaticity. Also, the asymptotic formula only holds for the *final* deviation from equilibrium and not the deviation *during* the process which is still given by the acceleration and therefore asymptotically behaves as $1/T^2$.

In conclusion of our simple classical example, we have seen that the deviations from equilibrium during a variation of the Hamiltonian are smaller if the variation is slower. The asymptotic behaviour of the deviation at the end of the process depends on the differentiability of the evolution. Therefore, especially if taking the system from the initial to the final equilibrium state with good accuracy is more crucial than the intermediate deviations, it is often advantageous to use smoother variations of the Hamiltonian.

3.2 Adiabatic transport in quantum mechanics and geometric phase

The concept of adiabaticity is not restricted to classical physics applies to quantum mechanics as well. It has been postulated already in the old quantum theory that as the classical adiabatic invariant – the action variable – is related to the integer quantum number by the Bohr-Sommerfeld quantization procedure, the quantum number should be an adiabatic invariant in quantum theory. This *adiabatic theorem* outlived the old

theory and was proven to be correct within the modern operator formalism by Born and Fock [38].

It states that a quantum mechanical system with a time-dependent Hamiltonian $\hat{H}(t)$ initially in an eigenstate belonging to the discrete spectrum of $\hat{H}(t_0)$ remains in the corresponding instantaneous eigenstate of $\hat{H}(t)$ if the Hamiltonian evolves adiabatically, i.e. infinitely slowly. Corresponding eigenstate here means the one with the same quantum numbers as the initial state.

In the simplest case of a non-degenerate Hamiltonian with a discrete spectrum whose eigenstates can be uniquely numbered by their increasing eigenenergy, this means that the system remains in the eigenstate with the same number as the initial state during an adiabatic evolution. This correspondence between eigenstates can be seen as very natural, considering that they change continuously as the Hamiltonian is varied and therefore a jump of the system between eigenstates with different numbers would imply a discontinuous change in the system's state vector.

Of course the adiabatic theorem in the form stated above is not very useful in practice because it assumes infinitely slow evolution. In reality, physical processes cannot proceed infinitely slowly. It is therefore natural to look for some quantitative criterion for adiabaticity, i.e. under what conditions can a real process be considered as *effectively* adiabatic. It turns out that the process needs to be slow with respect to the timescale set by separations between eigenenergies of the Hamiltonian. Somewhat vaguely speaking, the typical rate of change of the Hamiltonian needs to be much slower than the transition frequencies $(E_i - E_j)/\hbar$. For a more detailed treatment of this adiabatic condition, see for example Ref. [39].

Fig. 16 shows an example of an adiabatic process in a harmonic oscillator with a varying strength of the confining potential. It illustrates that in the adiabatic limit the first excited state of the initial Hamiltonian evolves into the corresponding eigenstate, the first excited state of the final Hamiltonian. On the other hand, a non-adiabatic sudden change of the Hamiltonian results in a transition into different energy eigenstates.

If crossing of energy levels occurs during the adiabatic evolution then the simple way of tracking the eigenstates by eigenenergy ordering fails at the crossing point. In this case, however, the requirement of continuous evolution of the state vector usually provides an unambiguous way of connecting the ingoing and outgoing energy levels at the degeneracy point. In some cases, the crossing is facilitated by a special structure of the Hamiltonian $\hat{H}(t)$ for all times t, for example the presence of a conserved quantity $\hat{A}$ which implies that the Hamiltonian does not couple different eigenspaces of $\hat{A}$. As a consequence, the eigenstates can be identified by the value of $\hat{A}$ *and* eigenenergy ordering within the individual eigenspaces of $\hat{A}$. These two quantum numbers are then conserved during an adiabatic evolution.

This behaviour at the degeneracy point can be illustrated by a simple example of a spin 1/2 particle with a magnetic moment in an adiabatically changing magnetic field B_z

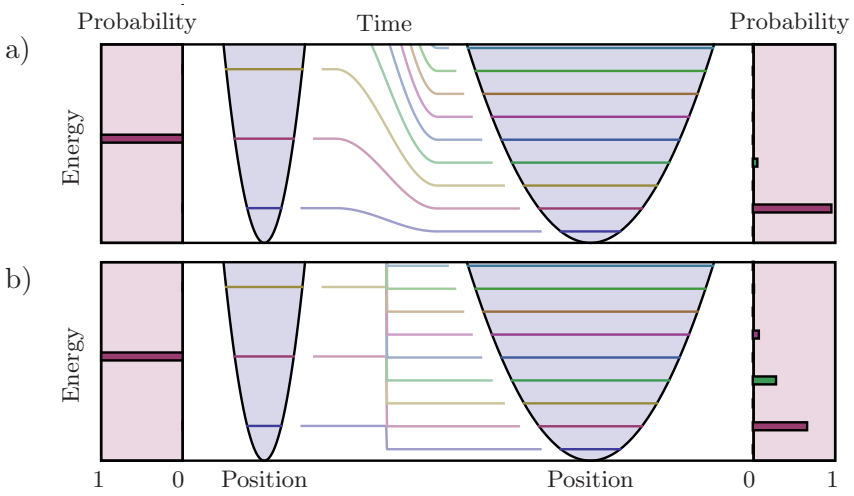

Figure 16: An example of an adiabatic change in a quantum system. A massive particle moving in a 1D harmonic potential with time-dependent strength is initially in the first excited state. The potential then changes so that the particle's oscillation frequency reduces to one third of its initial value. (a) If this variation is performed gradually the system has a very high probability of being found in the corresponding state of the changed Hamiltonian. (b) If the change is sudden there is a significant chance of inducing transitions to other energy eigenstates.

oriented along the z-axis. The z-component of the spin, given by the operator $\hat{\sigma}_z$, commutes with the Hamiltonian and is therefore conserved. As the system crosses the degeneracy point $B_z = 0$, its evolution is uniquely determined by this conservation law. Since the energy of the state is proportional to $B_z\sigma_z$, it crosses from the ground state to the excited state or vice versa as B_z changes its sign.

The existence of a conserved quantity can also cause the spectrum of the Hamiltonian to be degenerate during the whole evolution rather than just at isolated crossing points. Nevertheless, these two cases are in principle not different from the point of view of the adiabatic theorem, as both of them allow the adiabatic evolution of the state vector to be determined by requiring conservation of all the quantum numbers.

An interesting non-trivial situation arises when the degeneracy is present permanently but there is no global conservation law to account for it, i.e. the symmetry corresponding to the degeneracy is not the same during the whole evolution. In such cases, the adiabatic theorem does not uniquely determine the evolution of the state vector within the degenerate energy eigenspaces because there is no conserved quantity to distinguish between the vectors in the subspaces. The result of the adiabatic evolution can then in general depend on the way the Hamiltonian was transformed from its initial to its final value. Or equivalently, a cyclic evolution of the Hamiltonian can result in non-trivial unitary rotations within the degenerate energy eigenspaces, a phenomenon commonly known as non-abelian geometric phase [40] which is the basis of the proposed concept of *holonomic quantum computation* [41].

But even in the case of an adiabatic transport of a non-degenerate eigenstate the adiabatic theorem does not determine its evolution uniquely. The requirement that the system is at all times in the instantaneous energy eigenstate only specifies the state vector up to an unknown complex factor.

The question about the nature of this phase factor has only been addressed as late as 1984 by M.V. Berry [15] who discovered that it contains a non-trivial component connected with the geometric properties of the underlying Hilbert space. Although this observation was essentially new to the field of quantum mechanics, it has been quickly recognized that an analogous concept had been studied earlier in the context of classical light polarization by S. Pancharatnam [42].

The complex phase γ acquired by an eigenstate $|\varphi(t)\rangle$ of an adiabatically changing Hamiltonian $\hat{H}(t)$ corresponding to the eigenenergy $E(t)$ could be naively expected to be given by

$$\gamma(t) = -\frac{1}{\hbar}\int_{t_0}^{t} E(\tau)\,\mathrm{d}\tau. \qquad \text{(INCORRECT)}$$

However, such relation turns out to be incorrect. This can be verified either directly by showing that the state $\mathrm{e}^{\mathrm{i}\gamma(t)}|\varphi(t)\rangle$ does not satisfy the Schrödinger equation or simply based on the following argument. The phase $\gamma(t)$ is not an absolute quantity but is only defined relatively to the reference eigenvectors $|\varphi(t)\rangle$ and as such it should change if this reference frame is redefined. In particular, if the vectors $|\varphi(t)\rangle$ are replaced by $\mathrm{e}^{\mathrm{i}\delta(t)}|\varphi(t)\rangle$ with some arbitrary phase shift $\delta(t)$, the phase $\gamma(t)$ needs to change to $\gamma(t)+\delta(t_0)-\delta(t)$ in order to preserve the evolution of the physical state vector $\mathrm{e}^{\mathrm{i}\gamma(t)}|\varphi(t)\rangle$ which has to be independent of the choice of the reference eigenvectors. Clearly, this is inconsistent with the previous formula which does not involve the vectors $|\varphi(t)\rangle$ at all and is therefore obviously incorrect. The described redefinition of the eigenvectors $|\varphi(t)\rangle$ by an arbitrary phase change which has no observable consequences is usually called *gauge transformation*. Thus a more refined way of stating the argument above is that our incorrect form of the phase $\gamma(t)$ violates gauge invariance of the physical state vector $\mathrm{e}^{\mathrm{i}\gamma(t)}|\varphi(t)\rangle$.

Let us now derive an expression for the complex phase accompanying an *arbitrary* (i.e. not necessarily adiabatic) quantal evolution. We shall assume that the evolution of the state vector is again given up to an unknown phase factor $\mathrm{e}^{\mathrm{i}\gamma(t)}$ by a vector $|\varphi(t)\rangle$ which in this case need not be an energy eigenvector. Substituting the state vector $\mathrm{e}^{\mathrm{i}\gamma(t)}|\varphi(t)\rangle$ into the Schrödinger equation results in

$$\left(\mathrm{i}\frac{\mathrm{d}\gamma(t)}{\mathrm{d}t} + \frac{\mathrm{d}}{\mathrm{d}t}\right)|\varphi(t)\rangle = -\frac{\mathrm{i}}{\hbar}\hat{H}(t)|\varphi(t)\rangle.$$

After multiplying this equation by the bra vector $\langle\varphi(t)|$ and integrating from the initial time t_0 to the time t we obtain

$$\gamma(t) = -\frac{1}{\hbar}\int_{t_0}^{t}\langle\varphi(\tau)|\hat{H}(\tau)|\varphi(\tau)\rangle\,\mathrm{d}\tau + \mathrm{i}\int_{t_0}^{t}\langle\varphi(\tau)|\frac{\mathrm{d}}{\mathrm{d}\tau}|\varphi(\tau)\rangle\,\mathrm{d}\tau.$$

We can see that apart from the expected term given by the energy integral, there is an additional gauge-dependent contribution to the phase. It is easy to show that the presence of this additional term results in the correct behaviour of the phase under gauge transformations as described above. Also, the new term is clearly independent of the way the evolution of the vector $|\varphi(t)\rangle$ is parametrized. In other words, using any parameter λ in place of time in the integral $\int_{t_0}^{t} \langle\varphi(\tau)|\mathrm{d}/\mathrm{d}\tau|\varphi(\tau)\rangle \,\mathrm{d}\tau$ yields the same result. The integral therefore only depends on the trajectory of the vector in the Hilbert space and not on the dynamical quantities – energy and time. Based on this observation, the phase $\gamma(t)$ can be split into a *geometric* part $\gamma_g(\lambda)$ and a *dynamical* part $\gamma_d(t)$ defined as

$$\gamma_d(t) = -\frac{1}{\hbar}\int_{t_0}^{t} \langle\varphi(\tau)|\hat{H}(\tau)|\varphi(\tau)\rangle \,\mathrm{d}\tau, \tag{22a}$$

$$\gamma_g(\lambda) = \mathrm{i}\int \langle\varphi(\lambda)|\frac{\mathrm{d}}{\mathrm{d}\lambda}|\varphi(\lambda)\rangle \,\mathrm{d}\lambda. \tag{22b}$$

These two generally valid equations, first derived by Aharonov and Anandan [43] for cyclic evolution, can of course be applied to adiabatic processes in which case they transform into the form used originally by Berry [15]. The vector $|\varphi(t)\rangle$ is then simply the eigenvector of the Hamiltonian $\hat{H}(t)$ and the expectation value $\langle\varphi(\tau)|\hat{H}(\tau)|\varphi(\tau)\rangle$ can be replaced by the eigenenergy $E(\tau)$.

Even though we have obtained an additional geometric phase term which can be seen as a necessary ingredient ensuring gauge invariance of the adiabatically evolving state vector, it is perhaps not immediately obvious whether the presence of this new term has any physically observable consequences.

Maybe the only effect the geometric term has is to cancel the phase changes induced by gauge transformations? In that case, the geometric phase would indeed be quite uninteresting because it could be completely cancelled by choosing an appropriate gauge for the eigenvectors $|\varphi(\lambda)\rangle$. Fortunately, there is more to the geometric phase than that. Let us imagine a *cyclic* adiabatic evolution. The reference eigenvectors $|\varphi(\lambda)\rangle$ at the beginning and at the end of the process are identical and the phase γ is therefore a gauge-invariant quantity. If the system is transported along a non-trivial loop (i.e. one enclosing a non-zero area) in the Hilbert space then the line integral in Eq. (22b) can in general be non-zero. This cyclic geometric phase, being gauge-invariant, cannot be eliminated by a gauge transformation and if it is not identical for all energy eigenstates, its presence can be observed experimentally since phase differences are quantities measurable in an interference experiment.

The fact that the geometric phase only depends on the path traced by the eigenvector is generally believed to make it less susceptible to unwanted fluctuations in control parameters of the Hamiltonian [44]. For example, it is not affected by errors in dynamical parameters such as speed of the evolution or eigenenergies of the Hamiltonian, as long as the adiabatic approximation can still be used. Such resilience to noise is obviously a highly desirable property for quantum information processing. As any unitary operation is just a multiplication by phase factors in its eigenbasis, a universal set of gates

needed for quantum computation can in principle be realized using the geometric phase simply by designing an appropriate adiabatically changing Hamiltonian. The experimental realization of this seemingly simple task can of course be quite challenging. It might be difficult to find a suitable system with a well-controllable Hamiltonian or the presence of decoherence effects might force the operation time of the device to be as short as possible, thus making it potentially problematic to satisfy the requirement of adiabaticity. Another obstacle for using the geometric phase in quantum computation is the need to eliminate the dynamical phase given by Eq. (22a), an inevitable part of the total phase. This is usually accomplished by using the spin-echo technique. Another, conceptually simpler approach, is offered by the *non-abelian geometric phase* which arises during adiabatic transport of *degenerate* eigenstates. If all the computational states have equal eigenenergies they acquire the same dynamical phase which can then be neglected.

To compute the geometric phase using Eq. (22b), we parametrize the space of all possible Hamiltonians of the system by some coordinate system $x_1, x_2, \ldots, x_d$. If the adiabatically changing Hamiltonian follows a path P given parametrically by a vector function $\mathbf{x}(\lambda) = (x_1(\lambda), x_2(\lambda), \ldots, x_d(\lambda))$, then the geometric phase can be expressed as a line integral in the d-dimensional parameter space

$$\gamma_g(\lambda) = \mathrm{i} \int_P \langle \varphi(\mathbf{x}) | \nabla | \varphi(\mathbf{x}) \rangle \cdot \mathrm{d}\mathbf{x}. \tag{23}$$

The vector field $\mathrm{i}\langle \varphi(\mathbf{x}) | \nabla | \varphi(\mathbf{x}) \rangle$ therefore fully characterises the geometric phase in the given system. If the path P traced by the Hamiltonian is closed then the cyclic geometric phase can be rewritten using Stokes' theorem and a few elementary algebraic manipulations as

$$\gamma_g = \mathrm{i} \int_\Sigma \nabla \langle \varphi(\mathbf{x}) | \times \nabla | \varphi(\mathbf{x}) \rangle \cdot \mathrm{d}\mathbf{\Sigma}, \tag{24}$$

where Σ is the surface enclosed by P. We can express the vector field in the integrand with the help of the following identity:

$$\langle \varphi'(\mathbf{x}) | \nabla | \varphi(\mathbf{x}) \rangle = \frac{\langle \varphi'(\mathbf{x}) | (\nabla \hat{H}(\mathbf{x})) | \varphi(\mathbf{x}) \rangle}{E(\mathbf{x}) - E'(\mathbf{x})},$$

which holds for any two distinct eigenvectors $|\varphi(\mathbf{x})\rangle$, $|\varphi'(\mathbf{x})\rangle$ with the respective eigenvalues $E(\mathbf{x})$, $E'(\mathbf{x})$ and can be very simply derived by applying the operator ∇ to the identity $\langle \varphi'(\mathbf{x}) | \hat{H}(\mathbf{x}) | \varphi(\mathbf{x}) \rangle = 0$. The resulting expression for the cyclic geometric phase is then

$$\gamma_g = \mathrm{i} \sum_{\varphi' \neq \varphi} \int_\Sigma \frac{\langle \varphi(\mathbf{x}) | (\nabla \hat{H}(\mathbf{x})) | \varphi'(\mathbf{x}) \rangle \times \langle \varphi'(\mathbf{x}) | (\nabla \hat{H}(\mathbf{x})) | \varphi(\mathbf{x}) \rangle}{(E(\mathbf{x}) - E'(\mathbf{x}))^2} \cdot \mathrm{d}\mathbf{\Sigma}, \tag{25}$$

where the summation extends over all eigenvectors $|\varphi'(\mathbf{x})\rangle$ of $\hat{H}(\mathbf{x})$ distinct from $|\varphi(\mathbf{x})\rangle$. Whereas the original Eq. (24) is simpler in its form, Eq. (25) does not involve derivatives of the eigenvectors but only matrix elements of the operator $\nabla \hat{H}(\mathbf{x})$ in the energy eigenbasis, which is in many cases easier to calculate. Moreover, Eq. (25) is also manifestly gauge-invariant.

3.3 Geometric phase in simple quantum systems

We will now use the general formulas derived in the previous Section to calculate the geometric phase for three simple quantum-mechanical system – a qubit, a harmonic oscillator and a tripod system. While the first and the last one are included only to illustrate the results discussed above with concrete examples, the derivation of the harmonic oscillator geometric phase is relevant to the experiment described in detail in Sections 4 and 5 of this thesis.

3.3.1 Two-level system

Let us first take a look at a simple two-level system which represents the elementary unit of quantum information – a qubit. A general Hamiltonian of such system can be expressed up to a trivial overall energy shift as a linear combination of the Pauli matrices

$$\hat{H} = a_x\hat{\sigma}_x + a_y\hat{\sigma}_y + a_z\hat{\sigma}_z, \tag{26}$$

where a_x, a_y and a_z are arbitrary real coefficients, forming a three-dimensional vector $\vec{a}$. Similarly, vectors in a two-dimensional Hilbert space can be up to a complex phase factor parametrized by two angles ϑ and φ as

$$|\psi\rangle = \cos\frac{\vartheta}{2}\mathrm{e}^{-\mathrm{i}\varphi/2}|z+\rangle + \sin\frac{\vartheta}{2}\mathrm{e}^{+\mathrm{i}\varphi/2}|z-\rangle, \tag{27}$$

where $|z\pm\rangle$ are the eigenvectors of $\hat{\sigma}_z$ corresponding to eigenvalues ±1. The angles ϑ and φ can be also viewed as spherical coordinates of a unit vector $\vec{n}$ with components $n_x = \sin\vartheta\cos\varphi$, $n_y = \sin\vartheta\sin\varphi$ and $n_z = \cos\vartheta$ – the so-called *Bloch vector*. This natural correspondence between three-dimensional real unit vectors $\vec{n}$ and two-dimensional complex vectors $|\vec{n}\rangle$ gives rise to the well-known pictorial representation of states of a two level quantum system as points on a *Bloch sphere* (see Fig. 17).

The described parametrizations of hermitian operators and vectors in a two-dimensional Hilbert space are closely interlinked. It can be shown that a Hamiltonian given by a vector $\vec{a}$ has eigenvalues $\pm|\vec{a}|$ with corresponding eigenvectors $|\pm\vec{n}\rangle$, where $\vec{n} = \vec{a}/|\vec{a}|$.

If the Hamiltonian evolves adiabatically and the varying direction of the vector parameter $\vec{a}(t)$ is described by the spherical coordinates $\vartheta(t)$ and $\varphi(t)$, then the evolution of the eigenvector $|\vec{n}(t)\rangle$ is given simply by Eq. (27). For the eigenvector $|-\vec{n}(t)\rangle$, whose corresponding Bloch vector has the opposite sign, the angle ϑ needs to be replaced by $\vartheta+\pi$. Using Eq. (23), we easily obtain an expression for the geometric phase acquired by the eigenvectors $|\pm\vec{n}\rangle$ during a cyclic adiabatic evolution

$$\begin{aligned}\gamma_g^{\pm} &= \mathrm{i}\oint_P \langle\pm\vec{n}|\frac{\partial}{\partial\vartheta}|\pm\vec{n}\rangle\,\mathrm{d}\vartheta + \langle\pm\vec{n}|\frac{\partial}{\partial\varphi}|\pm\vec{n}\rangle\,\mathrm{d}\varphi \\ &= \pm\frac{1}{2}\oint_P \cos\vartheta\,\mathrm{d}\varphi.\end{aligned}$$

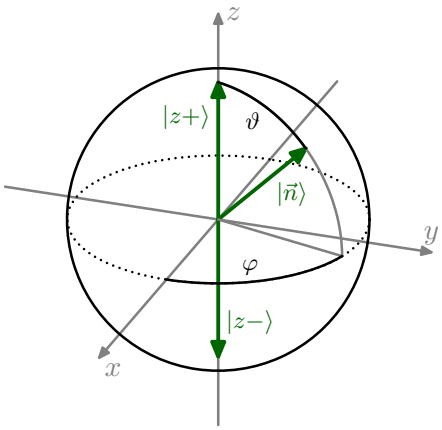

Figure 17: The Bloch sphere. The two eigenvectors $|z\pm\rangle$ of $\hat{\sigma}_z$ are represented by unit vectors collinear and anticollinear with the z-axis. A general superposition $|\vec{n}\rangle$ of these basis vectors in the form given by Eq. (27) corresponds to a unit vector $\vec{n}$ characterised by spherical coordinates ϑ and φ.

It is easy to derive that the integral $\oint_P (1-\cos\vartheta)\,\mathrm{d}\varphi$ equals the solid angle $\mathcal{A}$ enclosed by the path of the unit vector $\vec{n}$. The geometric phase is then given by $\pm\frac{1}{2}(2\pi\nu - \mathcal{A})$, where $\nu = \oint_P \mathrm{d}\varphi/2\pi$ is the winding number of the path P, i.e. the number of times it encircles the z-axis. The appearance of ν in the formula for the geometric phase might seem paradoxical at first glance because it privileges the z-axis, although we expect the result to be isotropic. However, the vector given by Eq. (27), which we chose to parametrize the eigenvectors, changes its sign when φ is increased by 2π. The geometric phase derived above is therefore taken with respect to initial and final eigenvectors with opposite signs if ν is odd. If we want to express the cyclic geometric phase properly, that is with respect to the same initial and final eigenvector, we need to multiply the phase factor $\mathrm{e}^{\mathrm{i}\gamma_g}$ by $(-1)^\nu$ which effectively eliminates the dependence of the geometric phase on ν. We could have also avoided this little complication by calculating the geometric phase using Eq. (24) instead of Eq. (23). We would have of course arrived at the same result which is

$$\gamma_g^{\pm} = \mp\frac{1}{2}\mathcal{A}. \tag{28}$$

This simple relation between the geometric phase acquired by a two-level system and the solid angle (see Fig. 18) enclosed by the trajectory of the system on the Bloch sphere was first derived in Berry's original paper [15].

3.3.2 Harmonic oscillator

Let us now look at the geometric phase in another simple quantum system – a harmonic oscillator. We will consider a driven oscillator whose Hamiltonian is given by

$$\hat{H}(t) = \hbar\omega\hat{a}^\dagger\hat{a} + \frac{1}{2}\hbar(\tilde{\varepsilon}(t)\hat{a}^\dagger + \tilde{\varepsilon}^*(t)\hat{a}),$$

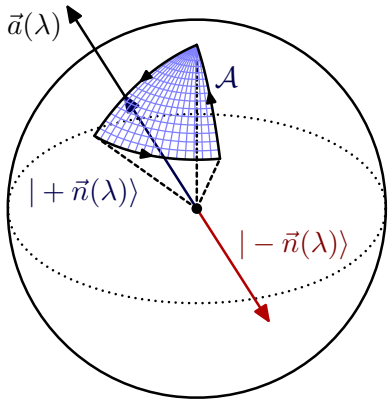

Figure 18: Solid angle traced by a state vector on the Bloch sphere. The three-dimensional vector $\vec{n}$ (in blue) representing the eigenvector $|+\vec{n}\rangle$ of the two-level Hamiltonian traces a trajectory on the unit Bloch sphere. The solid angle $\mathcal{A}$ is defined as the area of the spherical segment enclosed by this trajectory.

where $\tilde{\varepsilon}(t)$ is the (complex) drive strength. The Hamiltonian can be also expressed as

$$\hat{H}(t) = \hbar\omega \left(\hat{a} + \frac{\tilde{\varepsilon}(t)}{2\omega}\right)^\dagger \left(\hat{a} + \frac{\tilde{\varepsilon}(t)}{2\omega}\right) - \hbar\frac{|\tilde{\varepsilon}(t)|^2}{4\omega}.$$

This has the same form as the free harmonic oscillator Hamiltonian $\hat{H}_0 = \hbar\omega\hat{a}^\dagger\hat{a}$ but with the overall energy shifted by $-|\tilde{\varepsilon}(t)|^2/4\omega$ and the ladder operator $\hat{a}$ replaced by $\hat{a}+\tilde{\varepsilon}(t)/2\omega$. This displacement process can be illustrated with a simple classical analogy as depicted in Fig. 19 – a quadratic potential whose equilibrium point is shifted after addition of a constant force. The "shifted" ladder operators obviously satisfy the same commutation relation as $\hat{a}$ and $\hat{a}^\dagger$. The spectrum of the driven oscillator has the same harmonic structure as the free oscillator and its ground state $|\alpha(t)\rangle$ is annihilated by the operator $\hat{a} + \tilde{\varepsilon}(t)/2\omega$. In other words, it is an eigenvector of $\hat{a}$ with an eigenvalue $\alpha(t) = -\tilde{\varepsilon}(t)/2\omega$.

Eigenvectors of $\hat{a}$ are usually called *coherent states* and they can be expressed in the free oscillator eigenbasis as

$$|\alpha\rangle = \mathrm{e}^{-|\alpha|^2/2} \sum_{n=0}^{\infty} \frac{\alpha^n}{\sqrt{n!}} |n\rangle. \tag{29}$$

More generally, the n-th eigenstate $|\varphi_n(t)\rangle$ of $\hat{H}(t)$ is related to $|n\rangle$ by the so-called *displacement operator*

$$\hat{D}(\alpha) = \exp(\alpha\hat{a}^\dagger - \alpha^*\hat{a}), \tag{30}$$

which is unitary and satisfies $\hat{D}^\dagger(\alpha)\hat{a}\hat{D}(\alpha) = \hat{a} + \alpha$ and therefore

$$\hat{H}(t)\underbrace{\hat{D}(\alpha(t))|n\rangle}_{|\varphi_n(t)\rangle} = \overbrace{\hbar\left(\omega n - \frac{|\tilde{\varepsilon}(t)|^2}{4\omega}\right)}^{E_n(t)} \underbrace{\hat{D}(\alpha(t))|n\rangle}_{|\varphi_n(t)\rangle}.$$

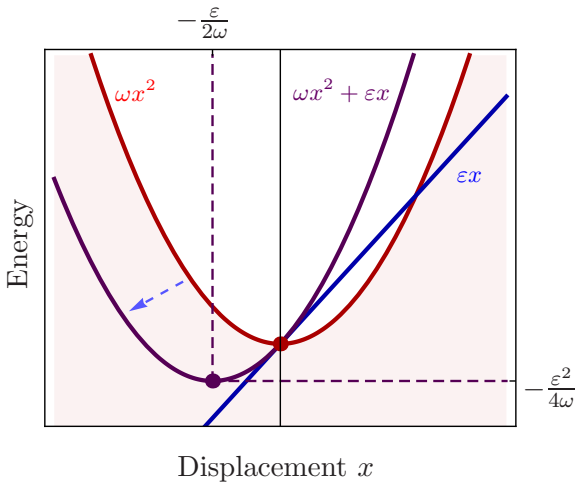

Figure 19: Shift of a harmonic potential by a linear term. An additional linear term εx (in blue) is added to a classical quadratic potential ωx^2 (in red). The resulting quadratic potential (in purple) has an equilibrium point which is shifted by $-\varepsilon/2\omega$ from its original position and its energy is lowered by $\varepsilon^2/4\omega$. This can be seen as a simple classical analogy of the quantum harmonic oscillator displacement.

If the drive strength $\tilde{\varepsilon}(t)$ changes adiabatically, the state vector of the harmonic oscillator initially in the Fock state $|n\rangle$ – according to the adiabatic theorem – follows the displaced eigenvector $|\varphi_n(t)\rangle = \hat{D}(\alpha(t))|n\rangle$. The dynamical and geometric phases acquired during the adiabatic evolution can then be calculated using Eqs. (22). After substituting the eigenvector $|\varphi_n(t)\rangle$ we obtain

$$\gamma_d^{(n)}(t) = \int_{t_0}^{t} \left(\frac{|\tilde{\varepsilon}(\tau)|^2}{4\omega} - \omega n \right) \mathrm{d}\tau, \tag{31a}$$

$$\gamma_g^{(n)}(\lambda) = \mathrm{i} \int \langle n|\hat{D}^\dagger(\alpha(\lambda)) \frac{\mathrm{d}}{\mathrm{d}\lambda} \hat{D}(\alpha(\lambda))|n\rangle \, \mathrm{d}\lambda. \tag{31b}$$

The derivative $\mathrm{d}\hat{D}(\alpha(\lambda))/\mathrm{d}\lambda$ can be calculated using the well-known *Baker-Campbell-Hausdorff formula*

$$\exp(\hat{A} + \hat{B}) = \exp \hat{A} \exp \hat{B} \exp \frac{1}{2}[\hat{B}, \hat{A}], \tag{32}$$

which is valid for any operators $\hat{A}, \hat{B}$ satisfying $[\hat{A}, [\hat{A}, \hat{B}]] = [\hat{A}, [\hat{A}, \hat{B}]] = 0$. This condition obviously holds for any linear combinations of the ladder operators since their commutator is a c-number. Applying this formula to the operators $\hat{A} = \alpha\hat{a}^\dagger - \alpha^*\hat{a}$ and $\hat{B} = \mathrm{d}\alpha\hat{a}^\dagger - \mathrm{d}\alpha^*\hat{a}$ then yields

$$\hat{D}(\alpha + \mathrm{d}\alpha) = \hat{D}(\alpha)\hat{D}(\mathrm{d}\alpha) \exp \frac{\alpha^* \, \mathrm{d}\alpha - \alpha \, \mathrm{d}\alpha^*}{2}$$

and consequently

$$\begin{aligned} \hat{D}^\dagger(\alpha) \, \mathrm{d}\hat{D}(\alpha) =& \hat{D}(\mathrm{d}\alpha) \exp \frac{\alpha^* \, \mathrm{d}\alpha - \alpha \, \mathrm{d}\alpha^*}{2} - \mathbb{1} \\ =& \hat{a}^\dagger \, \mathrm{d}\alpha - \hat{a} \, \mathrm{d}\alpha^* + \frac{1}{2}\alpha^* \, \mathrm{d}\alpha - \frac{1}{2}\alpha \, \mathrm{d}\alpha^*. \end{aligned}$$

Since the Fock states satisfy $\langle n|\hat{a}|n\rangle = \langle n|\hat{a}^\dagger|n\rangle = 0$ we obtain for the geometric phase an equation

$$\gamma_g(\lambda) = -\int \operatorname{Im}\alpha^*(\lambda)\frac{\mathrm{d}\alpha(\lambda)}{\mathrm{d}\lambda}\,\mathrm{d}\lambda. \tag{33}$$

Interestingly, the accumulated phase does not depend on the Fock state number n and is therefore completely independent of the initial state of the resonator. It can be observed even if the resonator is initially in a mixed state (e.g. a thermal state with non-zero temperature).

If the adiabatic evolution is cyclic this integral has a natural interpretation in terms of the area A_α enclosed by the curve $\alpha(\lambda)$ in the complex plane (see Fig. 20). Equivalently, the phase can be expressed using the area $A_{\tilde{\varepsilon}}$ enclosed by the trajectory of the complex drive strength $\tilde{\varepsilon}(\lambda)$ which is related to $\alpha(\lambda)$ by the equation $\alpha = -\tilde{\varepsilon}/2\omega$ derived above. The resulting expressions for the geometric phase are

$$\gamma_g = -2A_\alpha = -\frac{1}{2\omega^2}A_{\tilde{\varepsilon}}. \tag{34}$$

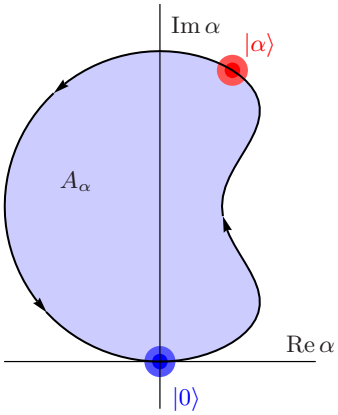

Figure 20: Path of the coherent state quadrature in the complex plane. The quadrature $\alpha = \langle\hat{a}\rangle$ of a coherent state of an adiabatically driven harmonic oscillator follows a path $\alpha(\lambda)$ in the complex plane. The area A_α enclosed by this curve determines the geometric phase acquired by the oscillator during the cyclic adiabatic evolution.

The harmonic oscillator geometric phase has been experimentally implemented in a trapped-ion two-qubit geometric gate [21]. There are also theoretical proposals for a similar experiment in a cavity QED system with two three-level atoms coupled to an electromagnetic mode [45]. Both of these experiments make use of the non-adiabatic geometric phase. A careful inspection of these cases raises an interesting question about the definition of the geometric and dynamical which – as it turns out – transform into each other if the rotating reference frame in which the system is described changes. We will address this issue in more detail in Section 3.4.

In this thesis, we have studied the *adiabatic* harmonic oscillator geometric phase in a circuit QED setup with transmon qubits, both theoretically (Section 4) and experimentally (Section 5).

3.3.3 The tripod system – non-abelian geometric phase

To illustrate the concept of non-abelian geometric phase, we will now describe one of the simplest systems in which it can be observed – the so-called *tripod system*, originally proposed in Ref. [46]. It is a four-level system with a Hamiltonian of the form

$$\hat{H} = \Omega_a|a\rangle\langle 0| + \Omega_b|b\rangle\langle 0| + \Omega_c|c\rangle\langle 0| + \text{h.c.}, \tag{35}$$

where $|a\rangle$, $|b\rangle$, $|c\rangle$ and $|0\rangle$ are four basis states of the system and Ω_a, Ω_b, Ω_c are complex coupling constants. The name *tripod* refers to the structure of the Hamiltonian shown in Fig. 21 – it couples the three states $|a\rangle$, $|b\rangle$ and $|c\rangle$ to $|0\rangle$ but not to each other.

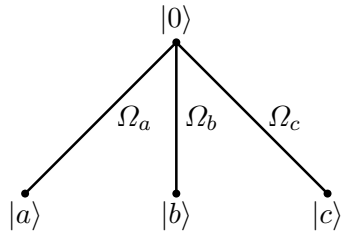

Figure 21: Structure of the tripod system. Three basis states $|a\rangle$, $|b\rangle$ and $|c\rangle$ couple to the fourth basis state $|0\rangle$ but not to each other.

All diagonal matrix elements of the Hamiltonian are zero, i.e. the basis states have the same (zero) energy. However, a Hamiltonian with the structure shown in Fig. 21 can be transformed into the off-diagonal form given by Eq. (35) even if the four states are not degenerate. The energy differences between them can be effectively eliminated by making the couplings Ω_a, Ω_b and Ω_c oscillating functions of time, transforming the Hamiltonian into a rotating frame and performing the rotating wave approximation.

If we define a normalized vector

$$|\Omega\rangle = \frac{\Omega_a|a\rangle + \Omega_b|b\rangle + \Omega_c|c\rangle}{\sqrt{|\Omega_a|^2 + |\Omega_b|^2 + |\Omega_c|^2}}$$

and rewrite the Hamiltonian in the form $\hat{H} = \sqrt{|\Omega_a|^2 + |\Omega_b|^2 + |\Omega_c|^2}|\Omega\rangle\langle 0| + \text{h.c.}$, it becomes obvious that it has two eigenvectors $|\varphi_\pm\rangle = (|0\rangle \pm |\Omega\rangle)/\sqrt{2}$ with eigenenergies $\pm\sqrt{|\Omega_a|^2 + |\Omega_b|^2 + |\Omega_c|^2}$ and a two-dimensional degenerate eigenspace with zero eigenenergy orthogonal to $|0\rangle$ and $|\Omega\rangle$ which can be used to encode the two computational states of a qubit.

The degenerate eigenspace $\mathscr{S}$ is restricted to the three-dimensional subspace spanned by $|a\rangle$, $|b\rangle$ and $|c\rangle$. If the couplings Ω_a, Ω_b and Ω_c are real, $\mathscr{S}$ can be easily visualized

as a two-dimensional plane in a three-dimensional Euclidean space in the following way. We can map state vectors $|\varphi\rangle = A|a\rangle + B|b\rangle + C|c\rangle$ with real coefficients A, B, C to Euclidean vectors $\vec{\varphi} = A\vec{e}_x + B\vec{e}_y + C\vec{e}_z$. The degenerate subspace is then simply a plane σ perpendicular to the vector $\vec{\Omega} = \Omega_a\vec{e}_x + \Omega_b\vec{e}_y + \Omega_c\vec{e}_z$. In this geometric picture, a state vector $|\varphi\rangle$ starting in the degenerate eigenspace and evolving under adiabatic variation of the couplings Ω_a, Ω_b and Ω_c is represented by a vector $\vec{\varphi}$ which is being continuously projected onto the moving plane σ. This process can be also seen as a parallel transport on a sphere where the varying vector $\vec{\Omega}$ determines a path and the plane σ is a tangent plane at each point of the path.

This shows that one can realize arbitrary rotations in the plane σ. For example, to rotate a vector by $\pi/2$, we can simply transport it along an equilateral spherical triangle with sides of length $\pi/2$. However, if the couplings Ω_a, Ω_b and Ω_c are kept real, one can implement only orthogonal transformations $O(2)$ in the eigenspace $\mathscr{S}$. To extend the possible operations to all elements of the *unitary* group $SU(2)$, Ω_a, Ω_b and Ω_c need to be complex and the convenient direct analogy with parallel transport on a sphere has to be abandoned.

Nevertheless, by choosing an appropriate path in the parameter space of Ω_a, Ω_b and Ω_c, one can in principle implement any unitary operation in the degenerate eigenspace of the tripod system. Unlike in the non-degenerate case, no additional manipulation is needed to cancel the dynamical phase, simply because the eigenenergies of the two computational states are equal.

3.4 Ambiguity of the non-adiabatic geometric and dynamical phase

Circuit QED systems are often described by an effective Hamiltonian in a rotating reference frame. It is important to note that time-dependent unitary transformations do not preserve the geometric phase. Upon replacing a state vector $|\varphi(t)\rangle$ by its rotating frame form $\hat{U}(t)|\varphi(t)\rangle$, the integrand in Eq. (22b) which determines the geometric phase transforms as

$$\begin{aligned}\langle\varphi(t)|\frac{\mathrm{d}}{\mathrm{d}t}|\varphi(t)\rangle &\to \langle\varphi(t)|\hat{U}^\dagger(t)\frac{\mathrm{d}}{\mathrm{d}t}\hat{U}(t)|\varphi(t)\rangle \\ &\to \langle\varphi(t)|\frac{\mathrm{d}}{\mathrm{d}t}|\varphi(t)\rangle + \langle\varphi(t)|\hat{U}^\dagger(t)\frac{\mathrm{d}\hat{U}(t)}{\mathrm{d}t}|\varphi(t)\rangle.\end{aligned}$$

If we describe the system without using rotating reference frames, the geometric phase is of course defined uniquely. Otherwise, however, it depends on the reference frame we choose to describe the system in. What frame should we use to define the geometric phase in a meaningful way? In the adiabatic case, it is natural to require that the trajectory of the adiabatically evolving eigenvector as well as its eigenenergy are invariant under a mere change of the timescale of the process. This criterion is enough to uniquely specify the phases.

However, it obviously cannot be used for non-adiabatic processes. In this case, the definition of the geometric and dynamical phase by Eqs. (22) remains ambiguous, as we will now illustrate with an example.

There is a proposal by Zheng [45] to implement the so-called *unconventional geometric phase gate*. It relies on the non-adiabatic geometric and dynamical phases associated with driving a coherent state of a harmonic oscillator resonantly along a circular path in the quadrature plane. In the frame rotating at the frequency of the harmonic oscillator, the Hamiltonian is

$$\hat{H}(t) = \frac{1}{2}\hbar(\tilde{\varepsilon}(t)\hat{a}^\dagger + \tilde{\varepsilon}^*(t)\hat{a}),$$

where $\tilde{\varepsilon}(t)$ is the complex drive strength in the oscillator-corotating frame. In the case of constant magnitude ε_0 and one rotation in the complex plane (see Fig. 22a) with angular frequency Ω, i.e. $\tilde{\varepsilon}(t) = \varepsilon_0 \exp(\mathrm{i}\Omega t)$, the quadrature $\alpha = \langle\hat{a}\rangle$ obeys the Heisenberg equation

$$\frac{\mathrm{d}\alpha(t)}{\mathrm{d}t} = \frac{\mathrm{i}}{\hbar}\langle[\hat{H}(t), \hat{a}]\rangle = -\frac{\mathrm{i}}{2}\tilde{\varepsilon}(t).$$

Its solution with the initial condition $\alpha(t) = 0$ is

$$\alpha(t) = \frac{\varepsilon_0}{2\Omega}(1 - \exp(\mathrm{i}\Omega t)).$$

The quadrature traces in the complex plane a circle with radius $\varepsilon_0/2\Omega$ (see Fig. 22a). Using Eq. (34) we obtain the geometric phase

$$\gamma_g = -\frac{\pi\varepsilon_0^2}{2\Omega^2}.$$

The dynamical phase can be expressed in terms of the energy expectation value using Eq. (22a)

$$\begin{aligned}\gamma_d &= -\frac{1}{\hbar}\int_0^{2\pi/\Omega} \langle\alpha(t)|\hat{H}(t)|\alpha(t)\rangle \,\mathrm{d}t = -\frac{1}{2}\int_0^{2\pi/\Omega} (\tilde{\varepsilon}(t)\alpha^*(t) + \tilde{\varepsilon}^*(t)\alpha(t)) \,\mathrm{d}t \\ &= \frac{\pi\varepsilon_0^2}{\Omega^2}.\end{aligned}$$

We can see that there is a relation between the geometric and the dynamical phase, namely $\gamma_d = -2\gamma_g$. It is this special property that the name *unconventional* geometric phase refers to.

Let us now look at the same process in another reference frame – the one corotating at the *drive* frequency. In this case the Hamiltonian takes the form

$$\hat{H}'(t) = \hbar\Omega\hat{a}^\dagger\hat{a} + \frac{1}{2}\hbar\varepsilon_0(\hat{a}^\dagger + \hat{a}) = \hbar\Omega\left(\hat{a} + \frac{\varepsilon_0}{2\Omega}\right)^\dagger\left(\hat{a} + \frac{\varepsilon_0}{2\Omega}\right) - \hbar\frac{\varepsilon_0^2}{4\Omega}.$$

This is just the displaced harmonic oscillator Hamiltonian discussed in Section 3.3.2. If we denote the displaced ladder operators by $\hat{b}$ and $\hat{b}^\dagger$, the initial vacuum state of the

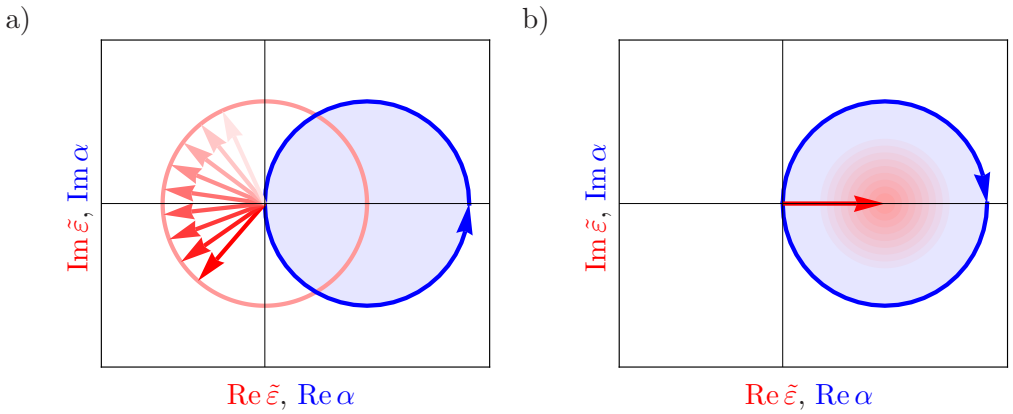

Figure 22: Two interpretations of the unconventional geometric phase. (a) In the oscillator-corotating frame, the drive $\tilde{\varepsilon}$ (in red) undergoes one rotation in the complex plane. The coherent state quadrature α (in blue) whose time derivative is proportional to $\tilde{\varepsilon}$ traces out a circle with the same orientation. (b) In the drive-corotating frame, the drive is time-independent and displaces the vacuum state of the oscillator. The coherent state $|\alpha\rangle$ then rotates around this displaced vacuum state in the *opposite* direction than in the oscillator-corotating frame.

original oscillator is simply a coherent state $|\beta\rangle$ of the new Hamiltonian where $\beta = \langle \hat{b} \rangle = \varepsilon_0/2\Omega$. Its evolution is given by the Heisenberg equation

$$\frac{\mathrm{d}\beta(t)}{\mathrm{d}t} = \frac{\mathrm{i}}{\hbar}\langle[\hat{H}'(t), \hat{b}]\rangle = -\mathrm{i}\Omega\beta(t),$$

which gives us $\beta(t) = \varepsilon_0 \exp(-\mathrm{i}\Omega t)/2\Omega$. Once again, the coherent state traces a circle of radius $\varepsilon_0/2\Omega$ but this time in the opposite direction than before (see Fig. 22b). The geometric phase is therefore

$$\gamma_g' = \frac{\pi\varepsilon_0^2}{2\Omega^2},$$

whereas the dynamical phase is

$$\gamma_d' = -\frac{1}{\hbar}\int_0^{2\pi/\Omega} \langle\beta(t)|\hat{H}'(t)|\beta(t)\rangle \,\mathrm{d}t = -\int_0^{2\pi/\Omega} \left(\Omega|\beta|^2 - \frac{\varepsilon_0^2}{4\Omega}\right) \mathrm{d}t = 0.$$

We can see that whereas the total phase remains the same in both reference frames, the way it is divided between the geometric and dynamical part differs. If we adopt yet another viewpoint and calculate the evolution operator of the oscillator directly from the time-independent Hamiltonian $\hat{H}'$, we get

$$\hat{U}'(T) = \exp(-\mathrm{i}\Omega T\hat{b}^\dagger\hat{b}) \exp\left(\mathrm{i}\frac{\varepsilon_0^2}{4\Omega}T\right).$$

After using the relation $\Omega T = 2\pi$ which implies $\exp(-\mathrm{i}\Omega T\hat{b}^\dagger\hat{b}) = \mathbb{1}$, we obtain simply

$$\hat{U}'(T) = \exp\left(\mathrm{i}\frac{\pi\varepsilon_0^2}{2\Omega^2}\right).$$

This is the same phase factor we calculated using the two previous approaches but now the phase originates from the overall energy shift $-\hbar\varepsilon_0^2/4\Omega$ of the displaced Hamiltonian $\hat{H}'$ and the connection with geometry seems to have disappeared altogether.

By deriving the non-adiabatic phase for this particular process in three different ways and showing how it can be interpreted rather arbitrarily as either geometric or dynamical, we have hopefully demonstrated that finding a proper definition of the non-adiabatic geometric phase may pose some problems.

This becomes even more apparent if we consider the question of measurement of the geometric phase. In the adiabatic case, reversing the evolution of the Hamiltonian, i.e. replacing $\hat{H}(t)$ by $\hat{H}(T-t)$, simply changes the direction of the trajectory traced by the adiabatically evolving eigenstate. This implies that the geometric phase given by Eq. (22b) changes its sign whereas the dynamical phase expressed in Eq. (22a) remains unchanged. One can therefore isolate the geometric part of the total phase simply by taking the difference between the phases for the two opposite orientations of the path.

Quite obviously, the situation becomes more complicated for a general non-adiabatic evolution. Reversing the variation of the Hamiltonian does not simply lead to a time-reversal of the state vector trajectory and the energy expectation value. Consequently, it is not possible to measure the geometric phase in the same way as for the adiabatic case.

It is considerably more difficult to control the evolution of the state vector and the energy expectation value *at the same time* for non-adiabatic processes. This shows us that the separation of the total phase into a geometric and a dynamical part given by Eqs. (22) might not be the most convenient way from an experimentalist's point of view.

As we would still like to study the geometric phase even in the non-adiabatic regime, we could perhaps adopt a slightly different definition which does not rely on our ability to find a special time-dependent Hamiltonian which exactly reverses the evolution of the state vector and its energy expectation value. Let us generalize the simple way of determining the geometric phase in the adiabatic limit discussed above and define a modified "geometric phase" in this way even for a general non-adiabatic evolution, i.e.

$$\gamma_g^{\mathrm{exp}} = \frac{\gamma - \gamma_{\mathrm{rev}}}{2}, \tag{36}$$

where γ and γ_{rev} are the phases accumulated by the state vector under the influence of the original Hamiltonian $\hat{H}(t)$ and the time-reversed one $\hat{H}(T-t)$, respectively. This "experimental definition" and the one derived from Schrödinger equation expressed in Eq. (22b) differ for non-adiabatic processes but they are clearly equivalent in the adiabatic limit.

We will touch on the difference between these two definitions again in Section 4 when we analytically calculate the phase acquired during a non-adiabatic evolution of the harmonic oscillator.

3.5 Generalizations of the geometric phase

Since the first description of the quantum-mechanical geometric phase by Berry [15], various generalized schemes have been proposed to extend its definition past the special case of cyclic adiabatic unitary evolution.

Aharonov and Anandan [43] made the important observation that the phase acquired by a state vector can be decomposed into a geometric and a dynamical term not only for the adiabatic case considered by Berry but for any cyclic unitary evolution. This generalization only requires a change in the definition of the dynamical phase which, instead of being expressed in terms of the adiabatically changing *eigenenergy*, is given by the energy *expectation value* $\langle\varphi(t)|\hat{H}(t)|\varphi(t)\rangle$ (see Eqs. (22)). Their paper also pointed out an interesting connection between the *Aharonov-Bohm effect* [47] and the geometric phase.

Another generalization emerged in a paper by Samuel and Bhandari [48] who extend the concept of geometric phase to non-cyclic and certain non-unitary processes. As we have seen, the phase accumulated during the evolution of a quantum system is in general not gauge-invariant, unless the evolution is cyclic. However, the phase for a non-cyclic process taking an initial state $|\varphi_1\rangle$ to a final state $|\varphi_2\rangle$ can be specified relatively to the phase of the inner product $\langle\varphi_2|\varphi_1\rangle$. Both of these phases transform in the same way under a change of gauge which implies that the non-cyclic phase defined as

$$\tilde{\gamma}_g = \gamma_g - \arg\langle\varphi_2|\varphi_1\rangle$$

is a gauge-invariant quantity. It is possible to show that this modified phase can be expressed as a cyclic geometric phase corresponding to a closed trajectory obtained by concatenation of the original path going from $|\varphi_1\rangle$ to $|\varphi_2\rangle$ with a *geodesic path* going back from $|\varphi_2\rangle$ to $|\varphi_1\rangle$.

The geodesic property is expressed in the usual way with respect to a gauge-invariant metric defined on the unit sphere in the Hilbert space $\mathscr{H}$ as

$$d^2(|\varphi\rangle, |\varphi\rangle + \mathrm{d}|\varphi\rangle) = \langle \mathrm{d}\varphi|(\mathbb{1} - \hat{P}_\varphi)|\mathrm{d}\varphi\rangle.$$

They also discuss the case of non-unitary evolution induced by projective measurements. They show that the geometric phase can be once again calculated as a cyclic phase by connecting the states before and after the measurement operations by geodesic paths.

The non-cyclic geometric phase described above is undefined if the initial and final states $|\varphi_1\rangle$ and $|\varphi_2\rangle$ are orthogonal. However, it was shown [49] that even in this case one can construct gauge-invariant objects containing non-trivial phase information. This so-called *off-diagonal geometric phase* involves relative phases of two or more energy eigenstates evolving at the same time.

An extension of the geometric phase to systems governed by non-hermitian Hamiltonians was described by Garrison and Wright [50]. The phase in their approach becomes a complex quantity whose imaginary part contributes to dissipation.

Generalization of the geometric phase from pure to mixed states has proven to be rather difficult. A treatment motivated by interferometric measurements was delineated in a paper by Sjöqvist et al. [51] and later extended to the off-diagonal phase in [52].

4 Geometric phase of a resonator in circuit QED

In the following section, we will theoretically describe an experiment in which we measure the geometric phase of a harmonic oscillator in circuit QED and whose practical realization and results will be presented in Section 5. The harmonic oscillator in our circuit QED setup is the microwave transmission line resonator used to read-out and couple qubits. The resonator is driven by an externally applied microwave signal and the system is then described by the rotating frame Hamiltonian

$$\hat{H}(t) = \hbar\delta\hat{a}^\dagger\hat{a} + \frac{1}{2}\hbar(\tilde{\varepsilon}(t)\hat{a}^\dagger + \tilde{\varepsilon}^*(t)\hat{a}). \tag{37}$$

$\delta = \omega_r - \omega$ is the detuning between the resonator frequency and the frequency of the drive signal and $\tilde{\varepsilon}(t)$ is the complex drive amplitude in the rotating frame, related to the oscillating value of the drive $\varepsilon_x(t)$ by $\varepsilon_x(t) = \mathrm{Re}\left(\tilde{\varepsilon}(t)\mathrm{e}^{-\mathrm{i}\omega t}\right)$.

This Hamiltonian is identical to the one discussed in Section 3.3.2, except for the frequency ω of the oscillator being replaced by the detuning δ. If the drive amplitude $\tilde{\varepsilon}(t)$ is varied adiabatically along a closed path in the complex plane the resonator accumulates a phase whose dynamical and geometric parts are given by Eqs. (31a) and (34), respectively.

However, as we have seen, this geometric phase and the drive-dependent part of the dynamical phase do not depend on the energy eigenvector being transported around. Since only differences between phases are actually measurable, the geometric phase of a harmonic oscillator cannot be directly observed [17, 18] by preparing a superposition of different eigenvalues of a two-level system which then acquire different phases.

In order to be able to measure a difference between geometric phases, one needs to have access to a control parameter to change the phase. In our case, this parameter is the detuning between the drive signal and the resonator frequency. If a qubit is dispersively coupled to the resonator, the Hamiltonian of the system is given by Eq. (20), originally derived for two qubits but we will now simply ignore the second qubit. As it turns out, we can also omit the resonator-mediated qubit drive term because in our case the resonator drive signal is far detuned from the qubit frequency. We will justify this step later at the end of this section. Finally, a careful inspection shows that the qubit-dependent correction to the resonator drive can be neglected as well and the qubit energy term $\hbar(\omega_q + \chi)|e\rangle\langle e|$ can be eliminated by a transformation into the qubit-corotating frame. In the end we are left with the simple Hamiltonian

$$\hat{H} = \hbar(\delta + 2\chi|e\rangle\langle e|)\hat{a}^\dagger\hat{a} + \frac{1}{2}\hbar(\tilde{\varepsilon}(t)\hat{a}^\dagger + \tilde{\varepsilon}^*(t)\hat{a}),$$

where δ is now the detuning between the resonator drive signal and the resonator frequency if the qubit is in the ground state. The only difference from the bare resonator Hamiltonian is the presence of the resonator frequency dispersive shift by 2χ if the qubit is in the excited state. The dispersive shift parameter χ is given by $\chi = g^2/(\omega_q - \omega_r)$

for a two-level qubit or – in the case of a multi-level qubit which is more relevant to our experimental setup,

$$\chi = \frac{g^2}{\omega_q - \omega_r} - \frac{g^2}{\omega_q + \alpha - \omega_r},$$

as derived in Section 2.2.2.

Note that no matter if the qubit is an ideal two-level system or not, our system can be still described by the same type of Hamiltonian, as long as the dispersive limit is valid. The details of the qubit structure are "hidden" in the single parameter χ.

As a consequence of the dispersive shift, the detuning between the resonator drive signal and the resonator frequency depends on the state of the qubit – it is either δ if the qubit is in the ground state or $\delta + 2\chi$ if it is in the excited state. The trajectory $\alpha(t)$ traced by an adiabatically transported state of the resonator in the quadrature plane is given by $\alpha(t) = -\tilde{\varepsilon}(t)/2\delta$ and therefore depends on the qubit state as well. The different areas enclosed by the trajectories for the two qubit states (see Fig. 23) then lead to a difference between the accumulated geometric phases, a quantity which is measurable unlike the phases themselves.

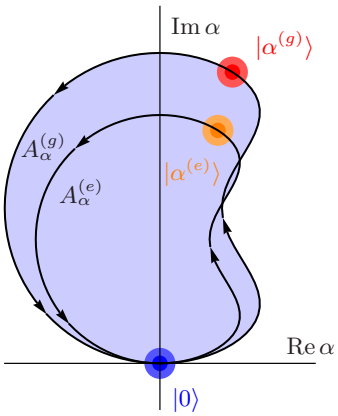

Figure 23: Qubit-dependent path of the coherent state quadrature. The path $\alpha(\lambda)$ traced by the quadrature $\alpha = \langle \hat{a} \rangle$ of an adiabatically driven resonator in the complex plane depends on the resonator-drive detuning. Since the qubit dispersively shifts the resonator frequency, the enclosed area A_α and the geometric phase depends on the qubit state.

Using Eqs. (31a) and (34) we can express the differences between the dynamical and geometric phases acquired for the two different qubit states as

$$\Delta\gamma_d = \gamma_d^{(e)} - \gamma_d^{(g)} = \left(\frac{1}{\delta + 2\chi} - \frac{1}{\delta}\right) \int_0^T \frac{|\tilde{\varepsilon}(t)|^2}{4}\, \mathrm{d}t, \tag{38a}$$

$$\Delta\gamma_g = \gamma_g^{(e)} - \gamma_g^{(g)} = -\left(\frac{1}{(\delta + 2\chi)^2} - \frac{1}{\delta^2}\right) \frac{A_{\tilde{\varepsilon}}}{2}, \tag{38b}$$

where $A_{\tilde{\varepsilon}}$ is the area enclosed by the path of $\tilde{\varepsilon}$ in the complex plane.

We can now have a look at a specific example of the drive amplitude trajectory $\tilde{\varepsilon}(t)$ and calculate the phase differences expressed by Eqs. (38). Let the drive amplitude be given as

$$\tilde{\varepsilon}(t) = \frac{1}{2}\varepsilon_0(1 - \mathrm{e}^{\mathrm{i}\Omega t}). \tag{39}$$

The corresponding trajectory is a simple circle going through the origin, centered at $\varepsilon_0/2$, as shown in Fig. 24. The maximum drive amplitude during the cycle is ε_0 and its duration is $T = 2\pi/|\Omega|$. This was the type of drive signal typically used in our experiment.

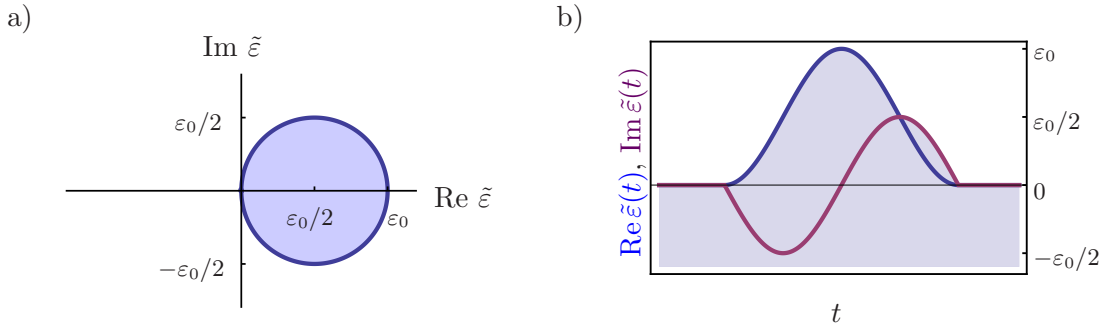

Figure 24: Resonator drive with a circular trajectory. (a) The complex drive strength $\tilde{\varepsilon}(t)$ given by Eq. (39) traces a circle in the complex plane. (b) Time dependence of the real and imaginary parts of $\tilde{\varepsilon}(t)$.

The integral $\int_0^T |\tilde{\varepsilon}(t)|^2 \,\mathrm{d}t$ as well as the area $A_{\tilde{\varepsilon}}$ are very easy to calculate. The resulting phases are

$$\Delta\gamma_d = \frac{1}{8}\left(\frac{1}{\delta + 2\chi} - \frac{1}{\delta}\right)|\varepsilon_0|^2 T, \tag{40a}$$

$$\Delta\gamma_g = \mp\frac{\pi}{8}\left(\frac{1}{(\delta + 2\chi)^2} - \frac{1}{\delta^2}\right)|\varepsilon_0|^2, \tag{40b}$$

where the signs $-$ and $+$ in $\mp$ correspond respectively to the counterclockwise and clockwise orientations of the cycle.

We can now briefly return to our previous claim that the qubit drive term mediated by the resonator can be neglected. The term in question is $g\tilde{\varepsilon}\hat{\sigma}_+/2\Delta + \mathrm{h.c.}$, where Δ is the detuning between the resonator and the qubit frequency. If we use the analogy between the qubit and a spin 1/2 particle, the magnetic field to which the spin is subjected forms an angle $\vartheta = \arctan g|\tilde{\varepsilon}|/\Delta^2$ with the z axis. Here we have used the fact that the difference between the resonator frequency ω_r and the drive frequency ω is much smaller than Δ which allows us to approximate the qubit-drive detuning $\omega_q - \omega$ by Δ. Using Eq. (40b) and assuming for simplicity that $\chi \ll \delta$, we can show that $\tan^2\vartheta$ is of the same order of magnitude as $\Delta\gamma_g\delta^3 g^2/\chi\Delta^4$. We can further express the dispersive shift parameter of a transmon qubit approximately as $\chi = \alpha g^2/\Delta^2$ and rewrite the estimate above as $\Delta\gamma_g\delta^3/\alpha\Delta^2$. Since in our experiment we have $\delta \ll \alpha, \Delta$ and the

observed geometric phase is of the order of unity, we get $\vartheta \ll 1$. This implies that the resonator drive signal does not significantly affect the state of the qubit. Additionally, the geometric phase accumulated by the qubit is comparable with $\tan^2\vartheta$ and is therefore much smaller than the resonator geometric phase. Hence, neglecting the qubit drive by the resonator field is indeed justifiable.

4.1 Ramsey measurement of the phase

One of the simplest and most commonly used ways of measuring a difference between phases accumulated by two given quantum states is the *Ramsey measurement*. It starts by preparing an equal superposition of the two states – in our case the ground and the excited qubit state. This can be done for example by applying the unitary transformation $\hat{R}^y_{-\pi/2} = \exp(\mathrm{i}\pi\hat{\sigma}_y/4)$ to the qubit which is initialized in its ground state. This operation, which can be represented as a rotation by $-\pi/2$ around the y-axis on the Bloch sphere, can be represented in the computational qubit basis by the matrix

$$\hat{R}^y_{-\pi/2} = \frac{1}{\sqrt{2}} \begin{pmatrix} 1 & 1 \\ -1 & 1 \end{pmatrix}.$$

In this way, we obtain the superposition state $(|g\rangle + |e\rangle)/\sqrt{2}$. So far, we have not considered that our system consists of the qubit and the resonator. The latter is initially in the vacuum state $|0\rangle$, independently of the qubit. The state of the whole system is therefore simply an equal superposition of the states $|g\rangle \otimes |0\rangle$ and $|e\rangle \otimes |0\rangle$.

When we then drive the state of the resonator adiabatically along a closed path starting and ending in the vacuum state, the two states $|g\rangle \otimes |0\rangle$ and $|e\rangle \otimes |0\rangle$ acquire phases $\gamma^{(g)}$ and $\gamma^{(e)}$, respectively. The fact that the resonator ends up back in the vacuum state for both states of the qubit is actually very important – it allows us to write the resulting state vector as a product state

$$\frac{1}{\sqrt{2}}(\mathrm{e}^{\mathrm{i}\gamma^{(g)}}|g\rangle + \mathrm{e}^{\mathrm{i}\gamma^{(e)}}|e\rangle) \otimes |0\rangle. \tag{41a}$$

The resonator is disentangled from the qubit just as it was in the beginning. We can therefore forget about its existence again and concentrate on the qubit. If we apply the operation $\hat{R}^y_{-\pi/2}$ once again, we get the final qubit state

$$\mathrm{e}^{\mathrm{i}(\gamma^{(e)}+\gamma^{(g)})/2} \left(\cos\frac{\gamma^{(e)} - \gamma^{(g)}}{2}|e\rangle - \mathrm{i}\sin\frac{\gamma^{(e)} - \gamma^{(g)}}{2}|g\rangle \right). \tag{41b}$$

By measuring the population of the excited state, we obtain

$$p_e = \cos^2\frac{\Delta\gamma}{2}, \tag{42}$$

where $\Delta\gamma = \gamma^{(e)} - \gamma^{(g)} = \Delta\gamma_d + \Delta\gamma_g$. This simple measurement allows us to determine the phase difference $\Delta\gamma$ up to sign reversal and unphysical shift by multiples of 2π.

The described measurement sequence together with the qubit states between the individual steps is illustrated in Fig. 25.

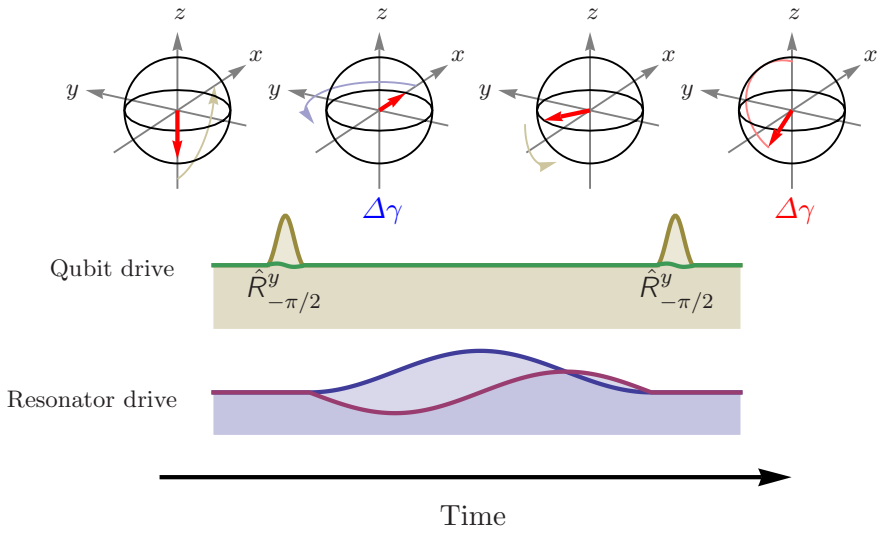

Figure 25: Ramsey measurement. The two pulses applied to the qubit realize the unitary operation $\hat{R}^y_{-\pi/2}$. The enclosed adiabatic resonator pulse drives the resonator state along a closed path. The Bloch state pictures schematically show the initial and the final state of the qubit as well as the states between the pulses. The axial angle $\Delta\gamma$ accumulated during the adiabatic cycle is mapped to an inclination angle with respect to the z-axis by the second qubit pulse.

If we want to determine the sign of $\Delta\gamma$ as well, we can simply remove the second Bloch sphere rotation and perform qubit tomography on the state immediately after the adiabatic resonator pulse (Eq. (41a)). The resulting expectation values $\langle\hat{\sigma}_x\rangle$ and $\langle\hat{\sigma}_y\rangle$ are

$$\begin{aligned}\langle\hat{\sigma}_x\rangle &= \cos\Delta\gamma,\\ \langle\hat{\sigma}_y\rangle &= -\sin\Delta\gamma,\end{aligned}$$

while $\langle\hat{\sigma}_z\rangle = 0$. These results can be used to reconstruct the phase difference $\Delta\gamma$ up to a multiple of 2π.

The question of how one can measure the geometric phase separately from the dynamical one using a spin echo technique will be discussed later in Section 5.3.5.

4.2 Exact solution of the harmonic oscillator evolution

One of the great advantages of dealing with a harmonic oscillator is its simplicity. Its evolution operator can be calculated exactly which makes investigation of effects such as non-adiabaticity rather easy.

We will now derive expressions for the displacement and the phase accumulated by a state of a harmonic oscillator evolving under the influence of an arbitrary time-dependent drive $\tilde{\varepsilon}(t)$.

By a transformation of the Hamiltonian (37) into the qubit-corotating frame, we obtain a Hamiltonian

$$\hat{H}(t) = \frac{1}{2}\hbar(\tilde{\varepsilon}(t)\mathrm{e}^{\mathrm{i}\delta t}\hat{a}^\dagger + \tilde{\varepsilon}^*(t)\mathrm{e}^{-\mathrm{i}\delta t}\hat{a}), \tag{43}$$

which contains only terms linear in the ladder operators $\hat{a}$ and $\hat{a}^\dagger$. This allows us to simplify the evolution operator

$$\hat{U}(t) = \mathsf{T}\exp\left(-\frac{\mathrm{i}}{2}\int_0^t (\tilde{\varepsilon}(\tau)\mathrm{e}^{\mathrm{i}\delta\tau}\hat{a}^\dagger + \tilde{\varepsilon}^*(\tau)\mathrm{e}^{-\mathrm{i}\delta\tau}\hat{a})\,\mathrm{d}\tau\right)$$

using the identity

$$\mathsf{T}\exp\left(\int_0^t \hat{A}(\tau)\,\mathrm{d}\tau\right) = \exp\left(\int_0^t \hat{A}(\tau)\,\mathrm{d}\tau\right)\exp\left(\frac{1}{2}\int_0^t\int_0^\tau [\hat{A}(\tau),\hat{A}(\tau')]\,\mathrm{d}\tau'\,\mathrm{d}\tau\right), \tag{44}$$

which holds for any time-dependent operator $\hat{A}(t)$ satisfying $[\hat{A}(t_1),[\hat{A}(t_2),\hat{A}(t_3)]] = 0$ for all $t_1,t_2,t_3 \in (0,t)$. This relation is a straightforward generalization of the Baker-Campbell-Hausdorff formula in Eq. (32).

As the interaction Hamiltonian is a linear combination of ladder operators, its nested commutators vanish and the identity (44) can be used to calculate the evolution operator

$$\hat{U}(t) = \exp\left(-\frac{\mathrm{i}}{2}\int_0^t (\tilde{\varepsilon}(\tau)\mathrm{e}^{\mathrm{i}\delta\tau}\hat{a}^\dagger + \tilde{\varepsilon}^*(\tau)\mathrm{e}^{-\mathrm{i}\delta\tau}\hat{a})\,\mathrm{d}\tau\right)\exp(\mathrm{i}\gamma(t)),$$

where the phase $\gamma(t)$ is given by

$$\gamma(t) = -\frac{1}{4}\int_0^t\int_0^\tau \operatorname{Im}\tilde{\varepsilon}^*(\tau)\tilde{\varepsilon}(\tau')\mathrm{e}^{-\mathrm{i}\delta(\tau-\tau')}\,\mathrm{d}\tau'\,\mathrm{d}\tau. \tag{45a}$$

We will transform the evolution operator back to the drive-corotating frame to be able to compare the exact result with that obtained using the adiabatic theorem. After replacing $\hat{U}(t)$ by $\exp(-\mathrm{i}\delta\hat{a}^\dagger\hat{a}t)\hat{U}(t)$ we use simple algebra to rewrite the evolution operator in the form

$$\hat{U}(t) = \hat{D}(\alpha(t))\mathrm{e}^{\mathrm{i}\gamma(t)}\exp(-\mathrm{i}\delta\hat{a}^\dagger\hat{a}t), \tag{45b}$$

where $\hat{D}$ is the displacement operator defined by Eq. (30) and the displacement $\alpha(t)$ is given by

$$\alpha(t) = -\frac{\mathrm{i}}{2}\mathrm{e}^{-\mathrm{i}\delta t}\int_0^t \tilde{\varepsilon}(\tau)\mathrm{e}^{\mathrm{i}\delta\tau}\,\mathrm{d}\tau. \tag{45c}$$

Eqs. (45) describe the evolution of the harmonic oscillator *exactly* within the rotating wave approximation which was used to obtain the Hamiltonian (37).

We can easily check that Eq. (45c) is consistent with the results obtained in Section 3.3.2 for adiabatic processes, specifically that an adiabatic change of the drive from 0 to $\tilde{\varepsilon}$ transports the vacuum state into a coherent state $|\alpha\rangle$ with $\alpha = -\tilde{\varepsilon}/2\delta$ which is the vacuum state of the displaced Hamiltonian. Integrating the expression in Eq. (45c) by parts results in

$$\alpha(t) = -\frac{\tilde{\varepsilon}(t)}{2\delta} + \frac{1}{2\delta}\mathrm{e}^{-\mathrm{i}\delta t}\int_0^t \dot{\tilde{\varepsilon}}(\tau)\mathrm{e}^{\mathrm{i}\delta\tau}\,\mathrm{d}\tau.$$

The first term is exactly the adiabatic result while the second one represents non-adiabatic corrections. Its dependence on the characteristic time scale T of the adiabatic process can be extracted by writing the drive amplitude in the form $\tilde{\varepsilon}(\tau) = f(\tau/T)$ where $f(u)$ is a function of a dimensionless argument $u = t/T$. The integral then takes the form

$$\int_0^{t/T} \dot{f}(u)\mathrm{e}^{\mathrm{i}\delta T u}\,\mathrm{d}u,$$

which can be shown to approach zero in the limit $T \to \infty$, assuming that $\dot{f}(u)$ is an L^1 integrable function[3].

This result can be easily generalized to derive the relation between adiabaticity and differentiability of the drive discussed for a classical harmonic oscillator in the context of the "egg-and-spoon race analogy" in Section 3.1. Let us assume that $\tilde{\varepsilon}(\tau)$ is k-times differentiable and the derivatives satisfy $\tilde{\varepsilon}^{(j)}(0) = \tilde{\varepsilon}^{(j)}(t) = 0$ for all $j < k$.

To obtain the displacement of the resonator state, we can integrate the expression in Eq. (45c) by parts k-times and get

$$\alpha(t) = -\frac{\tilde{\varepsilon}(t)}{2\delta} - \frac{\mathrm{i}}{2}\left(\frac{\mathrm{i}}{\delta}\right)^k \mathrm{e}^{-\mathrm{i}\delta t}\int_0^t \tilde{\varepsilon}^{(k)}(\tau)\mathrm{e}^{\mathrm{i}\delta\tau}\,\mathrm{d}\tau,$$

where the second term on the right-hand side is the non-adiabatic correction. By the same argument as before, the integral can be cast into the form

$$\frac{1}{T^{k-1}}\int_0^{t/T} f^{(k)}(u)\mathrm{e}^{\mathrm{i}\delta T u}\,\mathrm{d}u,$$

which obviously behaves as $o(1/T^{k-1})$ for $T \to \infty$. This confirms our previous observation based on the classical analogy – namely that a smoother variation of the Hamiltonian leads to a faster asymptotic decrease of the non-adiabatic corrections with increasing length of the process.

[3]This statement is sometimes known as the *Riemann-Lebesgue lemma*.

4.2.1 Example – circular trajectory drive

Let us now illustrate these general results with a simple example – the drive along a circular trajectory expressed by Eq. (39) – and use Eqs. (45a) and (45c) to calculate the phase accumulated by the resonator state as well as its trajectory in the quadrature plane.

Substituting the drive amplitude into Eq. (45c) gives us the displacement

$$\alpha(t) = -\frac{\varepsilon_0}{4\delta}(1 - \mathrm{e}^{\mathrm{i}\Omega t}) - \frac{\varepsilon_0 \Omega}{4\delta(\delta + \Omega)}(\mathrm{e}^{\mathrm{i}\Omega t} - \mathrm{e}^{-\mathrm{i}\delta t}). \tag{46}$$

The first term on the right-hand side is again the adiabatic result $-\tilde{\varepsilon}(t)/2\delta$ while the other one is the non-adiabatic correction. In the adiabatic limit as $\Omega/\delta \to 0$, the second term obviously vanishes as expected.

The shape of the trajectory traced by the resonator state is determined by the dimensionless ratio $N = \delta/\Omega$ which can be interpreted as the number of resonator oscillations that fit into the adiabatic cycle. The higher N, the closer the process is to the ideal adiabatic limit.

Some examples of the trajectories given by Eq. (46) are shown in Fig. 26. These curves,

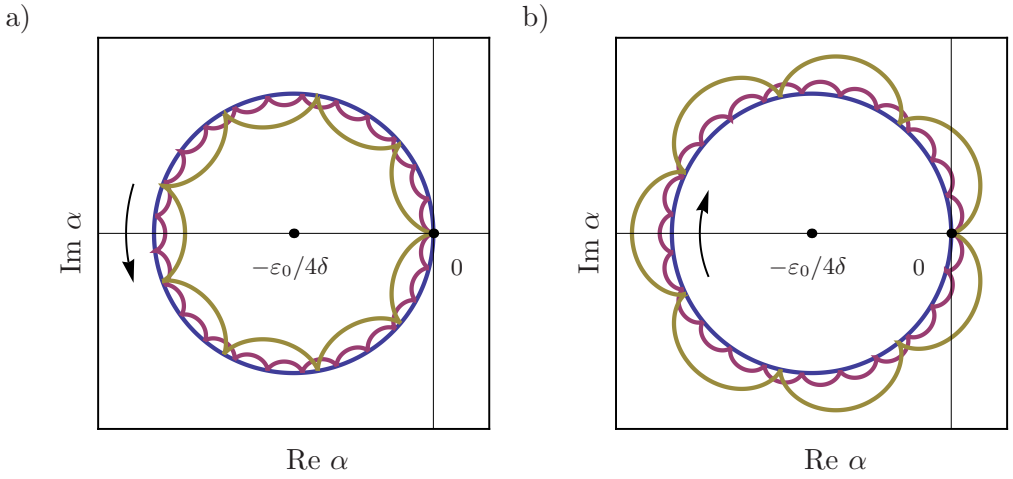

Figure 26: Exact trajectories of the resonator state driven by a circular pulse. (a) The coherent state quadrature of a harmonic oscillator evolving under the influence of the drive given by Eq. (39) follows a hypocycloid curve if $\delta/\Omega > 0$. The curves shown in the plot correspond to the ideal adiabatic case $\delta/\Omega \to \infty$ (in blue), $\delta/\Omega = 24$ (in purple) and $\delta/\Omega = 8$ (in yellow). (b) If $\delta/\Omega < 0$, the trajectory is an epicycloid. The values of δ/Ω for the plots are the same as in (a) except for a change of sign.

commonly known as *hypocycloids* and *epicycloids*, naturally emerge in geometry as trajectories of points on a circle rolling along the circumference of another circle (see Fig. 27). The size of their "lobes" decreases with increasing length of the drive pulse and their number is $|\delta/\Omega + 1|$. The trajectories are closed only if δ/Ω is an integer number. In

general, the drive pulse given by Eq. (39) leads to a final displacement of the resonator state by

$$\alpha(T) = -\frac{\varepsilon_0 \Omega}{4\delta(\delta+\Omega)}(1 - \mathrm{e}^{-2\pi \mathrm{i}\delta/\Omega}). \tag{47}$$

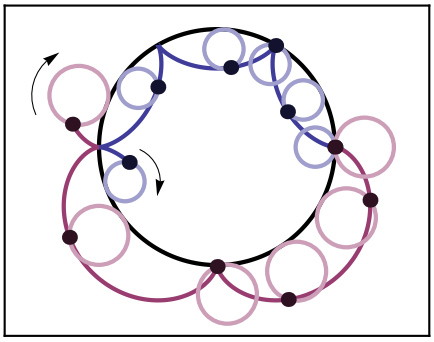

Figure 27: Geometric interpretation of the exact resonator state trajectories. The trajectories of the resonator state described by Eq. (46) can be seen as curves traced by a point on a circle rolling on the inside (for $\delta/\Omega > 0$, shown in blue) or the outside (for $\delta/\Omega < 0$, shown in purple) of a larger circle. The curves shown here correspond to $\delta/\Omega = 5$. The fixed circle is the ideal adiabatic trajectory with radius $|\varepsilon_0/4\delta|$. The rolling circle has a radius $|\varepsilon_0\Omega/4\delta(\delta+\Omega)|$ and the point at which the two circles touch is the displaced ground state quadrature $-\tilde{\varepsilon}(t)/2\delta$. At each point in time, the resonator state rotates around this touching point with angular velocity δ.

We can calculate the geometric phase accumulated by the resonator state by substituting the displacement $\alpha(t)$ from Eq. (46) into Eq. (33) which holds even for non-adiabatic processes. To evaluate the dynamical phase, we need to use the general equation (22a) instead of Eq. (31a) which is valid only in the adiabatic limit. The final results that we obtain are

$$\gamma_g = \frac{|\varepsilon_0|^2\Omega}{16\delta(\delta+\Omega)^2}\left((\Omega-\delta)T - \frac{\Omega(\Omega+3\delta)}{\Omega+\delta}\frac{\sin\delta T}{\delta}\right), \tag{48a}$$

$$\gamma_d = \frac{|\varepsilon_0|^2\Omega}{16\delta(\delta+\Omega)^2}\left(\frac{2\delta(2\Omega+\delta)}{\Omega}T + \frac{2\Omega\delta}{\Omega+\delta}\frac{\sin\delta T}{\delta}\right). \tag{48b}$$

If we were interested only in the *total* phase, we could of course obtain it also using Eq. (45a).

In order to distinguish the adiabatic limit from the non-adiabatic corrections, we will substitute $\Omega = \pm 2\pi/T$, where the signs $\pm$ correspond to the two possible directions of the drive cycle, and expand the phases in powers of T. We get the following series:

$$\gamma_g = \frac{|\varepsilon_0|^2}{8\delta^2}\left(\mp\pi + \frac{6\pi^2}{\delta T} - \frac{2\pi^2}{(\delta T)^2}(\pm 10\pi + 3\sin\delta T) + \dots\right),$$

$$\gamma_d = \frac{|\varepsilon_0|^2}{8\delta^2}\left(\delta T - \frac{4\pi^2}{\delta T} + \frac{4\pi^2}{(\delta T)^2}(\pm 4\pi + \sin\delta T) + \dots\right).$$

As expected, the dynamical phase contains a term linear in time while the leading term of the geometric phase is constant and its sign depends on the direction of the cycle. The non-adiabatic corrections to both phases are of the order $\mathcal{O}(1/T)$.

Both γ_g and γ_d contain terms whose sign depends on the direction of the drive trajectory as well as those which are invariant under a reversal of the path. This confirms that it is not possible to separate γ_g from γ_d simply by taking the difference between the total phases accumulated for the two different orientations of the drive path, in accordance with what we have learned about practical aspects of non-adiabatic geometric phase measurement in Section 3.4.

If we adopt a modified definition of the "experimental geometric phase" by Eq. (36) in terms of the difference between the phases for a clockwise and a counterclockwise cycle, it will be given exactly by the part of the total phase which is antisymmetric in Ω, i.e.

$$\gamma_g^{\mathrm{exp}} = \mp \frac{|\varepsilon_0|^2}{8\delta^2} \left(\pi + \frac{4\pi^3}{(\delta T)^2} + \dots \right),$$

while the dynamical phase in this definition is the symmetric part

$$\gamma_d^{\mathrm{exp}} = \frac{|\varepsilon_0|^2}{8\delta^2} \left(\delta T + \frac{2\pi^2}{\delta T} - \frac{2\pi^2}{(\delta T)^2} \sin \delta T + \dots \right).$$

A rather interesting difference between the "proper" (Eq. (22b)) and the "experimental" (Eq. (36)) geometric phase is that the latter includes only non-adiabatic terms of second and higher order in $1/T$. The missing term proportional to $1/T$ can be understood as a contribution from the area of the "lobes". For $\delta/\Omega < 0$, they extend outwards, thus increasing the absolute value of the area enclosed by the trajectory. When taking into account the orientation of the path, the area is actually negative and the lobes in fact *decrease* it. Similarly, if $\delta/\Omega > 0$, the area is positive and the inwards extending lobes decrease it again. Since the area of the lobes is to first order in $1/T$ identical for both orientations of the trajectory, their leading-order contribution to the phase gets cancelled when we subtract the phases.

To measure only the dynamical part of the adiabatic phase, a drive with fixed phase obtained by replacing $\tilde{\varepsilon}(t) \to |\tilde{\varepsilon}(t)|$ can be used. In this case, the area enclosed by the trajectory of the resonator state is zero and the geometric phase therefore vanishes. However, the dynamical phase, which only depends on the absolute value of the drive amplitude, is the same as for the original path. For the circular trajectory (Eq. (39)), the fixed-phase drive is

$$\tilde{\varepsilon}(t) = \frac{1}{2} |\varepsilon_0 (1 - \mathrm{e}^{\mathrm{i}\Omega t})| = |\varepsilon_0| \sin \frac{\Omega t}{2}. \tag{49}$$

Here we assume that $\Omega > 0$ and $0 \le t \le T$. Using Eq. (45a), we obtain the total phase

$$\gamma = \frac{|\varepsilon_0|^2}{2(4\delta^2 - \Omega^2)} \left(\delta T + \frac{2\Omega^2}{4\delta^2 - \Omega^2} \sin \delta T \right), \tag{50}$$

which can be again expanded in T as

$$\gamma = \frac{|\varepsilon_0|^2}{8\delta^2}\left(\delta T + \frac{\pi^2}{\delta T} + \frac{2\pi^2}{(\delta T)^2}\sin\delta T + \dots\right).$$

We can see that it indeed contains only the adiabatic dynamical phase term proportional to T and non-adiabatic corrections. The constant term is zero as expected. Fig. 28 shows a comparison of the total phases given by the sum of Eqs. (48) for the two orientations of the circular path and the phase for the real drive expressed in Eq. (50). The calculated

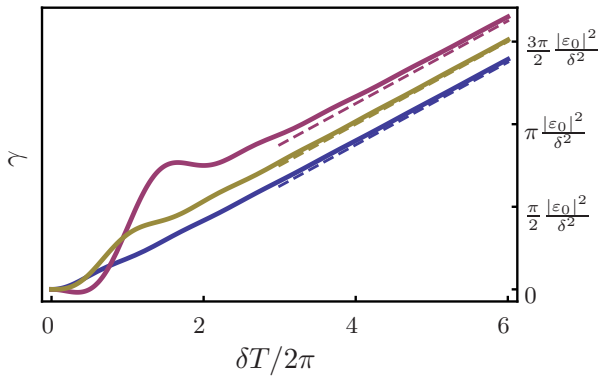

Figure 28: Phases induced by a drive with a circular trajectory. A comparison of the total phases for the drive defined in Eq. (39) as a function of $\delta T/2\pi$ with $\Omega > 0$ (in blue) and $\Omega < 0$ (in purple). The yellow curve shows the phase induced by the real drive given in Eq. (49). The dashed lines represent the adiabatic limit.

phases approach the adiabatic limit as $T \to \infty$ where we expect the phases for the two cycles to differ by the time-independent adiabatic geometric phase from the phase for the straight line trajectory, which is proportional to T.

It is quite noteworthy that the adiabatic limit describes the calculated exact phases rather accurately even for low values of $\delta T/2\pi$. The geometric phase of a harmonic oscillator is surprisingly robust against non-adiabatic effects.

4.3 Dephasing due to residual qubit-resonator entanglement

However, in the highly non-adiabatic regime where $\delta T/2\pi \gtrsim 1$, another effect starts to complicate measurements or potential practical utilization of the geometric phase.

A non-adiabatic process with a cyclically varying Hamiltonian does not in general drive the state of the system along a closed path. We have seen that the circular drive of a harmonic oscillator defined by Eq. (39) transports the initial vacuum state into a coherent state $|\alpha\rangle$ with α given by Eq. (47). The phase accumulated by the system can be described within the framework introduced for non-cyclic processes by Samuel and Bhandari [48].

Since the final displacement of the coherent state depends on the detuning δ (see Fig. 29) between the resonator and the drive frequency, it will interfere with the Ramsey-type phase measurement procedure (Section 4.1) which assumes that the state of the system after the resonator drive pulse can be written as a product state.

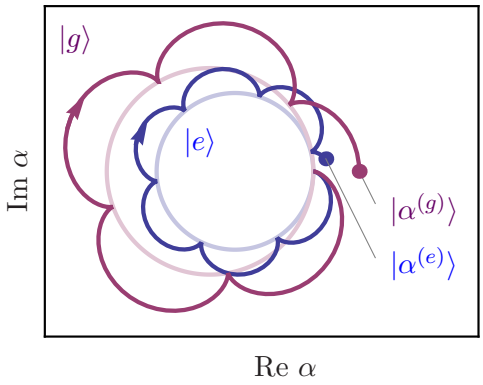

Figure 29: Qubit dependent final displacement of the resonator state. The final state of the resonator after a non-adiabatic pulse depends on the state of the qubit through the resonator-drive detuning δ. One reason is the different scale of the trajectory given by ε_0/δ, the other is the different phase of the non-adiabatic corrections which oscillate with frequency δ. The paths shown here correspond to rather arbitrarily chosen values of $\delta T/2\pi = 7.25$ for the excited state and $\delta T/2\pi = 5.5$ for the ground state.

Taking into account non-adiabatic effects, instead of the separable state given in Eq. (41a), the resonator drive pulse will result in a state

$$|\psi\rangle = \frac{1}{\sqrt{2}}(\mathrm{e}^{\mathrm{i}\gamma^{(g)}}|g\rangle \otimes |\alpha^{(g)}\rangle + \mathrm{e}^{\mathrm{i}\gamma^{(e)}}|e\rangle \otimes |\alpha^{(e)}\rangle),$$

in which the qubit and the resonator are entangled. The state of the qubit is then described by the reduced density matrix obtained from the full density matrix

$$\hat{\rho} = |\psi\rangle\langle\psi| = \frac{1}{2}\sum_{i,j\in\{g,e\}} \mathrm{e}^{\mathrm{i}(\gamma^{(i)}-\gamma^{(j)})}|i\rangle\langle j| \otimes |\alpha^{(i)}\rangle\langle\alpha^{(j)}|$$

by tracing over the resonator Hilbert space. The resulting expression is

$$\hat{\rho}_q = \frac{1}{2}(\mathbb{1} + |e\rangle\langle g|\mathrm{e}^{\mathrm{i}(\gamma^{(e)}-\gamma^{(g)})}\langle\alpha^{(g)}|\alpha^{(e)}\rangle + |g\rangle\langle e|\mathrm{e}^{\mathrm{i}(\gamma^{(g)}-\gamma^{(e)})}\langle\alpha^{(e)}|\alpha^{(g)}\rangle).$$

This density matrix differs from the one which we would get in the ideal adiabatic case for $\alpha^{(g)} = \alpha^{(e)}$ by the presence of the factor $\langle\alpha^{(g)}|\alpha^{(e)}\rangle$ which represents the overlap of the two final resonator states. It reduces the off-diagonal elements of the qubit density matrix, thereby effectively contributing to dephasing. In the Bloch sphere picture, it can be interpreted as a decrease in the x and y components of the Bloch vector.

Using Eq. (29) to express the coherent states in the Fock basis, the overlap factor can be easily calculated as

$$\langle\alpha^{(g)}|\alpha^{(e)}\rangle = \exp\left(\alpha^{(g)*}\alpha^{(e)} - \frac{1}{2}|\alpha^{(g)}|^2 - \frac{1}{2}|\alpha^{(e)}|^2\right),$$

which can be further rewritten in the form

$$\langle \alpha^{(g)} | \alpha^{(e)} \rangle = \exp\left(\mathrm{i}\, \mathrm{Im}\, \alpha^{(g)*} \alpha^{(e)} \right) \exp\left(-\frac{1}{2} |\alpha^{(g)} - \alpha^{(e)}|^2 \right).$$

The first exponential term is a phase factor which can be seen as an additional contribution to the geometric phase difference. This phase shift, which we will denote as γ_Δ, can be very naturally accounted for by a simple change of the definition of the area in the quadrature plane, as illustrated in Fig. 30.

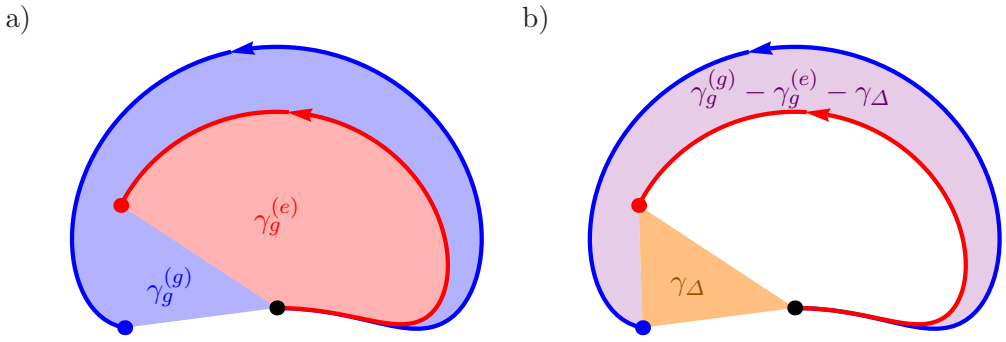

Figure 30: Interpretation of the coherent state overlap phase. (a) For an open trajectory in the quadrature plane, the "enclosed" area defined by Eq. (34) is obtained by joining the initial vacuum state with the final state, thus closing the path. (b) The additional phase term $\gamma_\Delta = \mathrm{Im}\, \alpha^{(g)*} \alpha^{(e)}$ is equivalent to a geometric phase corresponding to the area of a triangle (in orange) with vertices in the origin (black point) and the two quadratures $\alpha^{(e)}$ (red point) and $\alpha^{(g)}$ (blue point). The geometric phase difference together with this additional term then corresponds to the area (shown in purple) enclosed by the trajectories of the ground (in blue) and the excited (in red) states while joining the final resonator states directly instead of through the vacuum state.

The second exponential factor $\exp(-|\alpha^{(g)} - \alpha^{(e)}|^2/2)$ determines the magnitude of the off-diagonal terms in $\hat{\rho}_q$ and therefore the maximum possible value of the measured x and y spin projections.

This dephasing effect can be theoretically reduced in two ways. One of them is of course using longer adiabatic pulse. According to Eq. (47), the final resonator state quadratures decrease as $\mathcal{O}(1/T)$ in the adiabatic limit $T \to \infty$ which implies that the dephasing factor behaves as $1 - \mathcal{O}(1/T^2)$. Another way to reduce the non-adiabatic dephasing is to choose the detuning δ and the time T carefully so that δT is an integer number for *both* states of the qubit. Eq. (47) then implies that $\alpha^{(g)} = \alpha^{(e)} = 0$.

4.4 Two-qubit geometric phase gate

The non-linearity of the relation between the resonator-drive detuning and the geometric phase offers an interesting possibility to realize a two-qubit geometric phase gate.

Two-qubit gates utilizing the *non-adiabatic* harmonic oscillator geometric phase in systems with trapped ion qubits have been theoretically proposed in Refs. [19] and [53]. An

experimental implementation based on a process of the type described in Section 3.4 has been demonstrated in Ref. [21]. An important distinction between this experiment and the one performed in our work is that the drive of the harmonic oscillator in the trapped ion setup can be made highly selective to the qubit states. Specifically, the stretch mode of the collective oscillations in the trap is excited by the drive only if the qubits are in one of the states $|ge\rangle$ and $|eg\rangle$. On the other hand, in our circuit QED experiment the sensitivity of the resonator to the drive depends on the qubit states only weakly through the dispersive shifts. This causes the geometric phase differences measured in our experiment to be considerably smaller.

Let us consider a resonator dispersively coupled to two qubits. Just like in the one-qubit case, the resonator can be still treated as a harmonic oscillator but its frequency now depends on the state of the qubit due to the dispersive shift. We can write the detuning between the resonator and the drive frequency as

$$\delta + \chi^{(1)}\hat{\sigma}_z^{(1)} + \chi^{(2)}\hat{\sigma}_z^{(2)},$$

where $\chi^{(1,2)}$ are the dispersive shifts of the two qubits and $\hat{\sigma}_z^{(1,2)}$ are their Pauli matrices. As we have now expressed the dispersive shift in terms of the Pauli matrices instead of the projectors $|e\rangle\langle e|$, the detuning δ is now measured from the *bare* frequency of the resonator rather than its dressed frequency corresponding to the qubit in the ground state.

The adiabatic dynamical and geometric phases can be expressed using Eqs. (31a) and (34) as

$$\begin{aligned}\gamma_d =& \frac{1}{\delta + \chi^{(1)}\hat{\sigma}_z^{(1)} + \chi^{(2)}\hat{\sigma}_z^{(2)}} \int_0^T \frac{|\tilde{\varepsilon}(t)|^2}{4}\,\mathrm{d}t,\\ \gamma_g =& -\frac{1}{\left(\delta + \chi^{(1)}\hat{\sigma}_z^{(1)} + \chi^{(2)}\hat{\sigma}_z^{(2)}\right)^2}\frac{A_{\tilde{\varepsilon}}}{2}.\end{aligned}$$

Both of the qubit-dependent prefactors can be written in the form

$$A + B\hat{\sigma}_z^{(1)} + C\hat{\sigma}_z^{(2)} + D\hat{\sigma}_z^{(1)}\hat{\sigma}_z^{(2)}$$

for some coefficients A, B, C and D which can be easily determined by replacing the Pauli matrices with their eigenvalues ± 1 and solving the four resulting linear equations. Instead of calculating the coefficients exactly, we will settle for an approximation. By expanding the prefactors in powers of the dispersive shifts and truncating the series at the second order, we find that

$$\begin{aligned}\gamma_d \approx& \left(\frac{1}{\delta} - \frac{\chi^{(1)}}{\delta^2}\hat{\sigma}_z^{(1)} - \frac{\chi^{(2)}}{\delta^2}\hat{\sigma}_z^{(2)} + \frac{2\chi^{(1)}\chi^{(2)}}{\delta^3}\hat{\sigma}_z^{(1)}\hat{\sigma}_z^{(2)}\right)\int_0^T \frac{|\tilde{\varepsilon}(t)|^2}{4}\,\mathrm{d}t,\\ \gamma_g \approx& -\left(\frac{1}{\delta^2} - \frac{2\chi^{(1)}}{\delta^3}\hat{\sigma}_z^{(1)} - \frac{2\chi^{(2)}}{\delta^3}\hat{\sigma}_z^{(2)} + \frac{6\chi^{(1)}\chi^{(2)}}{\delta^4}\hat{\sigma}_z^{(1)}\hat{\sigma}_z^{(2)}\right)\frac{A_{\tilde{\varepsilon}}}{2}.\end{aligned}$$

The presence of the term $\hat{\sigma}_z^{(1)}\hat{\sigma}_z^{(2)}$ shows that the adiabatic cycles realizes a unitary operation which cannot be decomposed into a combination of one-qubit operations.

The total two-qubit phase can be isolated using a simple spin echo sequence similar to that described in subsequent Section 5.3.5 – the only difference being that the spin-flip operation $\hat{U}_F$ needs to be applied to both qubits and the direction of the second adiabatic cycle is not reversed. Assuming that the qubits are flipped back to their initial state in the end, the phases accumulated by the system during the two cycles have the form

$$A + B\hat{\sigma}_z^{(1)} + C\hat{\sigma}_z^{(2)} + D\hat{\sigma}_z^{(1)}\hat{\sigma}_z^{(2)},$$
$$A - B\hat{\sigma}_z^{(1)} - C\hat{\sigma}_z^{(2)} + D\hat{\sigma}_z^{(1)}\hat{\sigma}_z^{(2)}.$$

In this way we get rid of the one-qubit terms. The overall constant phase $2A$ can be neglected and the result is a simple two-qubit operation which can be written as $\exp(2\mathrm{i}D\hat{\sigma}_z^{(1)}\hat{\sigma}_z^{(2)})$. Obviously, the procedure we have just described gives us the *total* two-qubit phase, i.e. it does not separate the dynamical and the geometric part. If we are interested in the geometric phase, a more complicated spin echo sequence is needed.

It consists of four adiabatic cycles out of which the second and the fourth are reversed. Between the first and the second cycle, one of the qubits is spin-flipped. The other qubit is then flipped between the second and the third cycle and finally, the first qubit is flipped again between the last pair of cycles. The acquired phases are

$$A + B\hat{\sigma}_z^{(1)} + C\hat{\sigma}_z^{(2)} + D\hat{\sigma}_z^{(1)}\hat{\sigma}_z^{(2)},$$
$$\pm(A - B\hat{\sigma}_z^{(1)} + C\hat{\sigma}_z^{(2)} - D\hat{\sigma}_z^{(1)}\hat{\sigma}_z^{(2)}),$$
$$A - B\hat{\sigma}_z^{(1)} - C\hat{\sigma}_z^{(2)} + D\hat{\sigma}_z^{(1)}\hat{\sigma}_z^{(2)},$$
$$\pm(A + B\hat{\sigma}_z^{(1)} - C\hat{\sigma}_z^{(2)} - D\hat{\sigma}_z^{(1)}\hat{\sigma}_z^{(2)}),$$

where the signs + and − in ± correspond respectively to the dynamical and the geometric phase. We can see that the dynamical phase gets completely cancelled except for the irrelevant constant term whereas the only part remaining from the geometric phase is the two-qubit term $4D\hat{\sigma}_z^{(1)}\hat{\sigma}_z^{(2)}$.

An experimental demonstration of this two-qubit geometric phase gate will most likely be quite demanding. The fact that the two-qubit phase term is of second order in the dispersive shifts means that it is significantly smaller in magnitude than the one-qubit phases which we have measured so far. Also, the need for a spin echo sequence consisting of four adiabatic cycles implies that the length of the sequence and related decoherence effects will probably be a cause for concern.

5 Experiment

5.1 Experimental setup

5.1.1 The sample

The sample containing the superconducting qubits is a chip with an in-plane transmission line resonator with its centre line and ground planes fabricated out of niobium on a sapphire substrate by optical lithography (Fig. 31). More information about on-chip superconducting transmission line resonators and their fabrication can be found in Ref. [54].

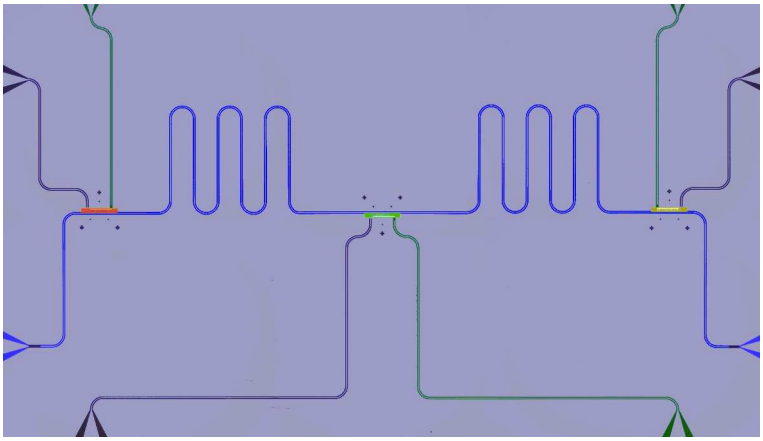

Figure 31: Optical microscope image of the sample (shown in false colours). The transmission line resonator is displayed in blue. The meander-like sections increase its total length without the need for a larger chip. Three transmon qubits – the rectangular structures shown in orange, green and yellow (for a close-up image, see Fig. 3b) – are located near the antinodes of the first harmonic mode of the resonator. They can be coherently manipulated using *charge lines* (dark green) and dynamically tuned by applying magnetic flux using *flux lines* (purple). The image was provided by J. Fink.

The sample contains three transmon qubits although only one of them was used in our experiment. They are embedded inside the resonator close to the antinodes of one of its electromagnetic modes. Their superconducting islands are made of aluminium and separated by a thin tunnel barrier of aluminium oxide constituting the Josephson junctions. For a more detailed description of the transmon qubit and its microscope image, see Section 2.1.3 and Fig. 3b.

A circuit diagram of the sample is shown in Fig. 32. The resonator can be driven by a microwave signal applied to its input port and the electric field inside can be observed via the output port. The qubits can be manipulated either through the resonator to which they are capacitively coupled or – as was the case in our experiment – using charge lines coupled directly to the qubits. Readout of the qubits is realized by dispersive measurement (see Section 2.3) using the resonator as a probe of the qubit state.

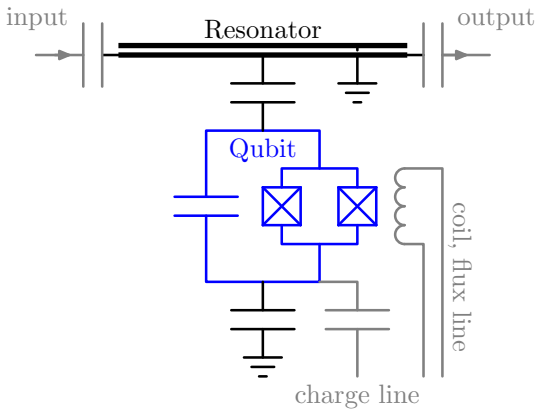

Figure 32: Circuit diagram of the sample. The transmon qubits, only one of which is shown here for simplicity, are capacitively coupled to a transmission line resonator equipped with an input and output port. External coils and on-chip flux lines are used to tune the qubit energies. The qubits can be driven directly by applying signals through their charge lines.

5.1.2 The dilution refrigerator

The sample is placed inside a *dilution refrigerator* where it is kept at a temperature of approximately 20 mK – sufficiently low to effectively cool the resonator and the qubits to their ground states. The typical qubit and resonator frequencies are in the range of 6 to 10 GHz. The corresponding excitation energies are equivalent to temperatures between 40 and 70 mK.

The dilution refrigerator operates by transporting helium-3 between two distinct thermodynamic phases of a ^{4}He/^{3}He mixture [55].

5.1.3 Measuring instruments

The microwave signals used to manipulate and read out the system are provided by RF signal generators producing frequencies in the gigahertz range. In our experiment, three microwave sources were connected to the resonator input, as illustrated in Fig. 33.

One of them, typically tuned close to the resonator frequency, is used for probing the resonator transmission. The signal transmitted through the resonator is then measured using *heterodyne detection* – it is mixed with a local oscillator signal, detuned from the probe frequency by 25 MHz, using a non-linear element – the *IQ mixer*. This component is designed to multiply two electrical signals, as described in more detail in Ref. [56]. In this case, multiplication of the probe and the local oscillator signals with respective frequencies f_R and f_L produces two side-band frequencies $|f_R - f_L|$ and $f_R + f_L$. The first of these components oscillates at 25 MHz – slowly enough to be time-resolved by a *field programmable gate array* (FPGA). The detected signal in a typical circuit QED measurement is extremely weak – the input signal is heavily attenuated in order to reach

the quantum regime where the mean number of photons in the resonator is of order unity. Consequently, the signal to be detected is much weaker than the noise imposed by the standard quantum limit as well as by non-ideal properties of the amplifiers used in the measurement process. The collected data therefore have to be hardware-averaged over many realizations of the measurement before they can be used to reconstruct the amplitude and the phase of the transmitted probe signal.

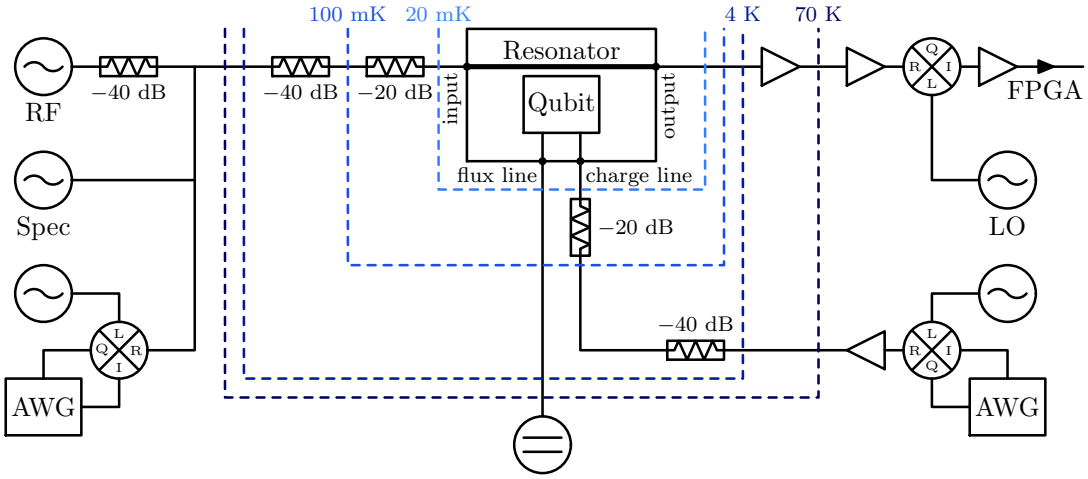

Figure 33: Schematic diagram of the experimental setup. The sample placed inside the dilution refrigerator is connected to four RF signal generators – three of them are connected to the input of the microwave resonator and one to the charge line of the qubit. The drive signals whose amplitudes and phases need to be modulated are mixed with a lower frequency output of arbitrary waveform generators. The AC signals are strongly attenuated before they enter the sample. DC sources are used to apply a magnetic flux to the split Josephson junction of the qubit and tune its frequency. The field at the output of the resonator is amplified and, after mixing with a detuned local oscillator tone, measured by an FPGA.

Another RF source is used to apply a coherent tone for qubit spectroscopy measurements which will be described in Section 5.2.2. The third generator provides the detuned resonator drive signal for transporting the resonator state along an adiabatic cycle. Frequency mixing is used to modulate the amplitude and the phase of the microwave signal [56]. A signal at a lower intermediate frequency f_{IF} with the desired amplitude and phase envelope is first generated by an *arbitrary waveform generator* (AWG). Mixing with the high frequency f_L yields two sidebands at frequencies $f_L \pm f_{IF}$. The amplitudes, phases and DC components of the input signals can be adjusted (in a so-called *mixer calibration* procedure) to eliminate one of the output frequency components as well as any direct leakage of the frequency f_L caused by imperfect operation of the device. As a result of the upconversion process, the phase and amplitude of the low frequency signal is imprinted on the high frequency wave.

The same technique is used to generate a modulated drive signal applied to the qubit through its charge line.

5.2 Methods

5.2.1 Resonator spectroscopy

The two key parameters of the microwave resonator – its resonant frequency ν_r and its photon life-time τ can be easily measured in a simple transmission measurement. The power P of a harmonic probe signal transmitted through the resonator as a function of its frequency is given by a Lorentzian function

$$P(\nu) = P_{\max} \frac{\delta\nu^2}{(\nu - \nu_r)^2 + \delta\nu^2},$$

where $P_{\max}$ is the peak power and $\delta\nu$ is the FWHM of the spectral line, related to the photon life-time by $\tau = 1/4\pi\delta\nu$.

Fig. 34 shows the result of a resonator transmission measurements. A fit of the theoretical Lorentzian lineshape to the experimental data yields the resonant frequency $\nu_r = \omega_r/2\pi = 7020.39$ MHz and the photon lifetime $\tau = (335 \pm 1)$ ns, corresponding to a decay rate $\kappa/2\pi = 2\delta\nu = (475 \pm 2)$ kHz.

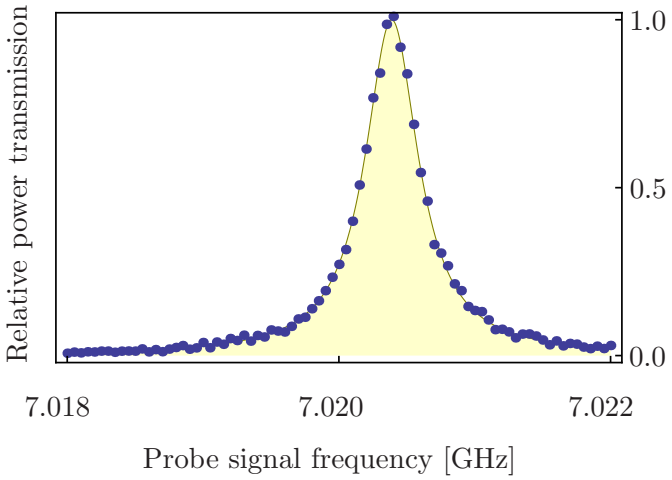

Figure 34: Resonator transmission spectrum. The plot shows the measured power transmitted through the resonator as a function of the signal frequency. The yellow curve is the fitted Lorentzian lineshape.

5.2.2 Qubit spectroscopy

The transition frequency of the qubit can be determined by a continuous spectroscopy measurement with two coherent tones being sent into the resonator. One of them is tuned to the resonator frequency while the other serves as the qubit drive. The stationary state of the qubit depends on the detuning δ_q between the drive signal and the qubit frequency. In a simple model which neglects the interactions between the resonator and the qubit,

solving the quantum master equation for the qubit yields the mean population p_e of the excited state in the stationary limit

$$p_e = \frac{\Omega^2}{\Gamma^2 + 4\delta_q^2 + 2\Omega^2}, \tag{51}$$

where Ω is the Rabi frequency corresponding to the applied qubit drive strength and Γ is the qubit relaxation rate. If the qubit is dispersively coupled to the resonator, it induces a shift of the resonator frequency depending on its quantum state, as expressed in Eq. (15). We can therefore (naively) expect that in the stationary state described above, the resonator frequency will be shifted on average by $2p_e\chi$ from its frequency for the qubit in the ground state. If the resonator probe signal is set to the frequency ω_r when $p_e = 0$, it will become off-resonant for $p_e > 0$ and the transmitted power will decrease. As we have seen, the excited state population p_e is largest when the qubit drive is resonant with the qubit frequency, i.e. $\delta_q = 0$, and becomes negligible when $\delta_q \gg \Gamma, \Omega$. In summary, if the experiment is repeated for varying frequencies of the qubit drive signal, we expect to observe a drop in the power of the transmitted resonator probe when the qubit drive is close to the qubit frequency.

This simple explanation of the qubit spectroscopy measurement relies on a rather crude assumption that the qubit can be treated separately from the resonator. In reality, the measured transmission spectrum as a function of the qubit drive frequency typically looks as shown in Fig. 35. The presence of multiple dips in the spectrum – a feature

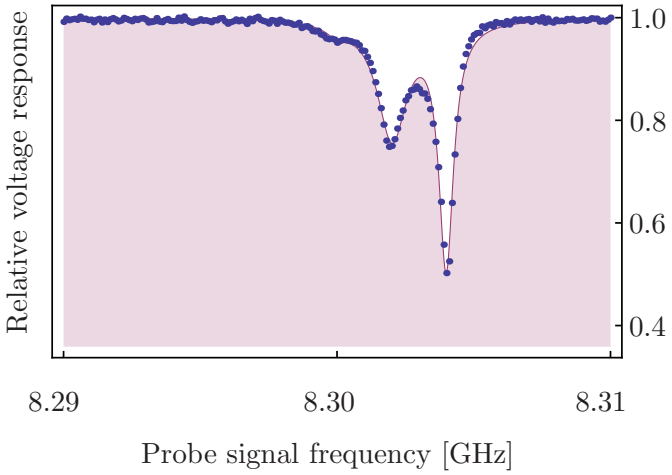

Figure 35: Qubit spectrum. The plot shows the measured relative voltage of the transmitted resonator probe signal as a function of the qubit drive frequency. The curve is a fit of three Lorentzian functions to the experimental data, which yields an estimate of the qubit frequency as well as the dispersive shift.

known as *photon number splitting* – is a result of the quantum nature of the resonator. The qubit frequency is shifted by $2\chi n$ with n photons in the resonator. The resulting spectrum can then be understood as a superposition of the individual discretely spaced spectral dips for the different photon numbers.

This description is still somewhat simplistic. In fact, the real form of the qubit spectrum can be quantitatively understood only by solving the full quantum master equation (21). However, the simple picture can still be used to at least estimate the qubit frequency ω_q and the dispersive shift χ. We did this by fitting a sum of three Lorentzian functions centered around ω_q, $\omega_q + 2\chi$ and $\omega_q + 4\chi$ to the measured data shown in Fig. 35. In this case, the choice of Lorentzian lineshapes was rather arbitrary. The obtained values of the qubit frequency and the dispersive shift were $\omega_q/2\pi = 8.3040$ GHz and $\chi/2\pi = -0.99$ MHz.

A more precise estimate of the qubit frequency can be obtained using a measurement of the Ramsey fringes which will be described in Section 5.2.4.

5.2.3 Qubit manipulation pulses

Unlike the continuous measurements described so far, most circuit QED experiments make use of microwave pulses to manipulate the qubit on a time scale much shorter than its coherence time. They can be applied either via the resonator or directly using the qubit's charge line. In both cases, the qubit – when approximated as an ideal two-level system – can be described by the simple Hamiltonian given in Eq. (4), which in the frame rotating with the drive frequency ω_d takes the form

$$\hat{H}(t) = \frac{1}{2}\hbar\delta_q\hat{\sigma}_z + \frac{1}{2}\hbar\left(\tilde{\Omega}(t)\hat{\sigma}_+ + \tilde{\Omega}^*(t)\hat{\sigma}_-\right), \tag{52}$$

where $\delta_q = \omega_q - \omega_d$ is the detuning between the qubit and the drive frequency, $\tilde{\Omega}$ is the complex qubit drive in the rotating frame and $\hat{\sigma}_\pm = (\hat{\sigma}_x \pm \hat{\sigma}_y)/2$.

By using resonant pulses, i.e. $\delta_q = 0$, with appropriate phases, simple unitary operations such as $\exp(-\mathrm{i}\beta\hat{\sigma}_x/2)$ and $\exp(-\mathrm{i}\beta\hat{\sigma}_y/2)$, corresponding to rotations by β around the x and y axes on the Bloch sphere, can be realized. For example, if $\tilde{\Omega}(t)$ is real then then the evolution operator is

$$\hat{U}(T) = \exp\left(-\frac{\mathrm{i}}{2}\hat{\sigma}_x\int_0^T \tilde{\Omega}(t)\,\mathrm{d}t\right).$$

If one chooses $\tilde{\Omega}(t)$ such that its time integral is equal to β, the resulting evolution is exactly a rotation by β around the x axis. Similarly, if the phase of the drive signal is shifted by $\pi/2$ – meaning that $\tilde{\Omega}(t)$ is purely imaginary – one obtains rotations around the y axis.

In this simple model, the resulting operation does obviously not depend on the shape and length of the drive pulse as long as the time integral of $\tilde{\Omega}(t)$ is fixed. In practice, using too short pulses will result in a violation of one of the approximations used to derive Eq. (52) – the rotating wave approximation or the assumption that the qubit is an ideal two-level system. Shorter pulses have a broader frequency spectrum and can

contain Fourier components which induce unwanted transitions into higher energy states of the qubit.

To avoid these effects, pulses with a smoother variation of the drive amplitude $\tilde{\Omega}(t)$ are usually preferred – for instance a Gaussian pulse has a narrower spectrum than a square pulse of the same length and with the same time integral of $\tilde{\Omega}(t)$. In our experiment, we use the so-called *DRAG pulses* proposed in Ref. [57] to reduce leakage to higher energy levels in weakly non-linear qubits.

These pulses are generated by adding a term proportional to $-\mathrm{i}\dot{\tilde{\Omega}}(t)/\alpha$, where α is the qubit anharmonicity, to the complex drive amplitude $\tilde{\Omega}(t)$. While theory dictates that the additional drive contribution should be *equal* to this expression, experimental data have shown [18] that the best results are obtained if it is scaled by a factor determined from a calibration measurement.

Fig. 36 shows a typical DRAG pulse used in our experiment. It is derived from a truncated Gaussian pulse and its length is 20 ns.

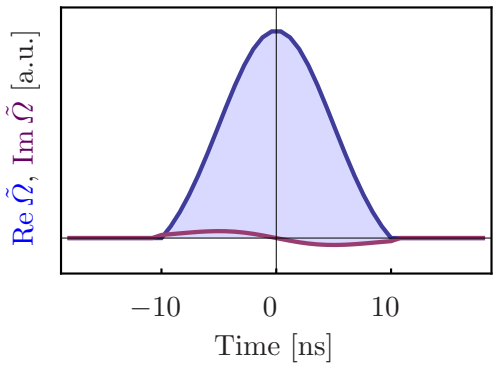

Figure 36: DRAG pulse. This plot shows the time variation of the two drive quadratures for a Gaussian DRAG pulse used in the experiment. It realizes a rotation around the x axis on the Bloch sphere. The DRAG correction $\mathrm{Im}\,\tilde{\Omega}(t)$ is proportional to the time derivative of the original pulse $\mathrm{Re}\,\tilde{\Omega}(t)$.

5.2.4 Ramsey fringes

A simple Ramsey interference measurement is typically used to improve the estimate of the qubit frequency obtained in a spectroscopy measurement. As described before in Section 4.1, this technique is a useful tool for measuring the difference between the phases accumulated by the two qubit states. In this case, it can be used to determine the phase associated with a free evolution of the qubit. The Ramsey sequence consists of two pulses rotating the qubit by $\pi/2$ around the x or the y axis and a time period between the two pulses during which the qubit accumulates the phase to be measured. If we let the qubit evolve freely, this phase will be equal to $-\delta_q T$ (Eq. (52)) where T is the time separation between the two qubit pulses. The measured population of the qubit excited state is then related to the phase (Eq. (42)). If we take into account dephasing

effects which cause an exponential decay of the magnitude of the qubit's Bloch vector during its free evolution, the final excited state population measured in the experiment is

$$p_e(T) = \frac{1}{2}\left(1 + \cos\left(\delta_q T\right) \exp\left(-\frac{T}{T_2}\right)\right),$$

where T_2 is the *dephasing time* of the qubit. As the time T increases, $p_e(T)$ undergoes damped oscillations – so-called *Ramsey fringes* – whose parameters δ_q and T_2 can be estimated from the measured data. Since the estimation is more accurate if $\delta_q \neq 0$, the objective of the qubit frequency measurement is usually to find a drive frequency which is detuned from the qubit by some given amount – typically $\delta_q/2\pi = 5$ MHz. The result of such Ramsey measurement is illustrated in Fig. 37a. The dephasing time obtained from the fit to the data is $T_2 = 0.96$ μs.

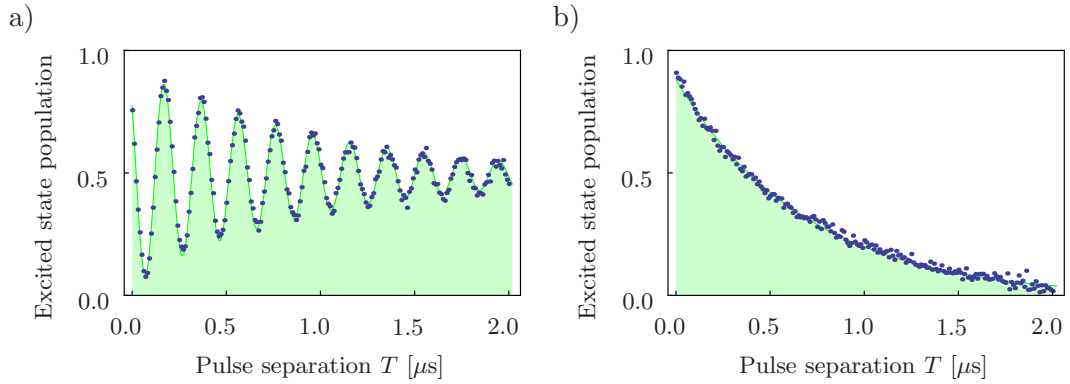

Figure 37: Ramsey and relaxation time measurement. (a) Results of a Ramsey measurement. The excited state population as a function of the separation T between the two qubit pulses oscillates with the frequency $\delta_q/2\pi = 5$ MHz. The green line is the theoretical fit of the damped Ramsey oscillations. (b) Results of a qubit relaxation measurement. The excited state population decays exponentially with increasing time delay T between the excitation pulse and the measurement.

5.2.5 Qubit relaxation time measurement

Apart from the dephasing time, the decoherence of the qubit is characterised by its relaxation time. It determines the rate at which the qubit spontaneously decays from the excited to the ground state. It can be determined by preparing the qubit in the excited state and measuring the population $p_e(T)$ as a function of the delay T between the state preparation and the measurement. The theoretically expected form of $p_e(T)$ is

$$p_e(T) = \exp\left(-\frac{T}{T_1}\right).$$

The measured data are shown in Fig. 37b. The extracted relaxation time is $T_1 = 0.68$ μs.

5.2.6 Rabi oscillations

The qubit and resonator drive parameters $\tilde{\Omega}$ and $\tilde{\varepsilon}$ are proportional to the voltage amplitudes of the microwave signals generated by the RF sources or the AWGs. The proportionality constant between these quantities is determined in a calibration measurement.

The Rabi frequency $\tilde{\Omega}$ for stronger signals, such as those used in qubit manipulation pulses, is usually calibrated by applying a short pulse to the qubit in its ground state and measuring the excited state population $p_e(a)$ as a function of the dimensionless pulse amplitude a passed as an input parameter to the AWG. The qubit undergoes flipping between the ground and the excited state whose angle β is proportional to a. By observing the *Rabi oscillations* of $p_e(a)$, one can obtain the relation between β and a or, if needed, between $\tilde{\Omega}$ and a.

Another type of calibration measurement for $\tilde{\Omega}$ uses a pulse of a given constant *amplitude* and observes the Rabi oscillations as a function of the pulse length T. It can be shown by solving the quantum master equation that the excited state population $p_e(T)$ in this case approaches the limiting value given by Eq. (51) as $T \to \infty$ and the deviation from this stationary value undergoes damped oscillations with a frequency $\sqrt{\Omega^2 - \Gamma^2/16}$ where $\Omega = |\tilde{\Omega}|$ and $\Gamma = 1/T_1$. By fitting this theoretical time dependence to the measured data, $\tilde{\Omega}$ can be determined for any given amplitude of the pulse. A result of this type of Rabi frequency measurement for $a = 0.04$ is shown in Fig. 38. The corresponding value of $\tilde{\Omega}$ extracted from the fit is $\tilde{\Omega} = 4.4$ MHz.

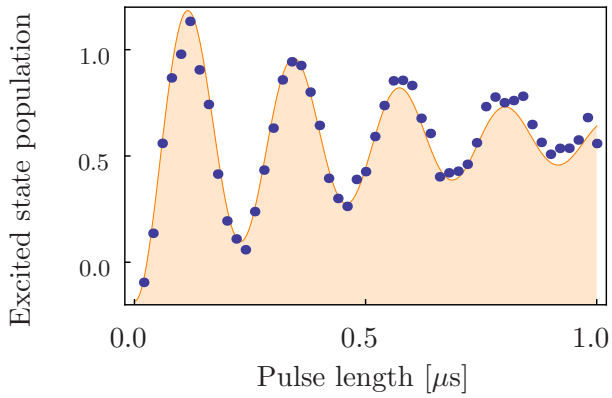

Figure 38: Rabi frequency measurement. The plot shows Rabi oscillations of the excited state population induced by a pulse of a constant amplitude $a = 0.04$ and a varying length T. The Rabi frequency can be determined from a fit of exponentially decaying oscillations (orange line) to the data. The range of the measured population is obviously incorrect as it clearly exceeds the maximum value of 1. This is most likely due to a poor calibration of the read-out but it does not affect the results of the fit.

5.2.7 Calibration of the resonator drive strength

The usual procedure for calibrating the resonator drive strength $\tilde{\varepsilon}$ is based on a measurement of the dispersive shift of the qubit frequency by the resonator field – sometimes also called *AC Stark shift*. A resonantly driven damped harmonic oscillator asymptotically approaches a stationary state in which the mean number of excitations is given by $n = \langle \hat{a}^\dagger \hat{a} \rangle = |\tilde{\varepsilon}|^2/\kappa^2$. We can therefore expect the qubit frequency to be dispersively shifted by $2\chi|\tilde{\varepsilon}|^2/\kappa^2$. This shift is measured in a simple spectroscopy experiment (Section 5.2.2) whose results are shown in Fig. 39a. Provided that the dispersive shift parameter χ and the resonator decay rate κ are known, we can then determine the drive strength $\tilde{\varepsilon}$.

This method is quite simple but it has a drawback. It can be used reliably only in the regime where the resonator field can be described classically, i.e. $\langle \hat{a}^\dagger \hat{a} \rangle \gg 1$. At the same time, it relies on the dispersive approximation which – as discussed in Section 2.2.2 – is justifiable only if $n \ll n_{\mathrm{crit}}$. The domain of validity of the simple model is therefore rather restricted and not very well defined.

Here we will describe an alternative calibration technique which we have tried out in our experiment. It is based on the same principle, i.e. measuring the qubit spectrum as a function of the resonator probe amplitude, but uses numerical calculations to relate the shape of the obtained spectral line to the unknown drive strength $\tilde{\varepsilon}$.

The outcome of the continuous qubit spectroscopy measurement can be found theoretically by calculating the stationary solution of the quantum master equation (21). It contains seven parameters. Three of them are fixed but can be determined in separate measurements as described earlier – the two dissipation rates Γ and κ and the dispersive shift χ. The two detunings δ_q and δ_r of the qubit and the resonator from their respective drive signals are freely adjustable. The resonator detuning is usually set to $\delta_r = 0$ and the value of δ_q is varied to obtain the qubit spectrum. The two drive amplitudes $\tilde{\Omega}$ and $\tilde{\varepsilon}$ can be also varied. The qubit drive can be determined by the Rabi frequency calibration procedure outlined above and the resonator drive is the only unknown parameter in the master equation.

We can therefore simulate the outcome of the spectroscopy measurement depending on the value of $\tilde{\varepsilon}$ and by comparison with the experimental results obtained for varying amplitude a of the resonator drive signal, we can find the unknown proportionality constant between $\tilde{\varepsilon}$ and a.

We solved the master equation numerically after restricting the infinite-dimensional Hilbert space of the resonator to a finite-dimensional one spanned by a certain number of the lowest lying Fock states. We chose a cutoff photon number of 12 and checked that this was indeed high enough by reproducing the stationary mean number of photons $|\tilde{\varepsilon}|^2/\kappa^2$ for a drive of the resonator without driving the qubit at the same time. We then ran the simulation long enough for the system to get sufficiently close to the stationary state and calculated the expected voltage quadrature measured at the output

of the resonator, which is proportional to $\langle \hat{a} \rangle = \mathrm{Tr}\, \hat{a}\hat{\rho}$ (see Fig. 39).

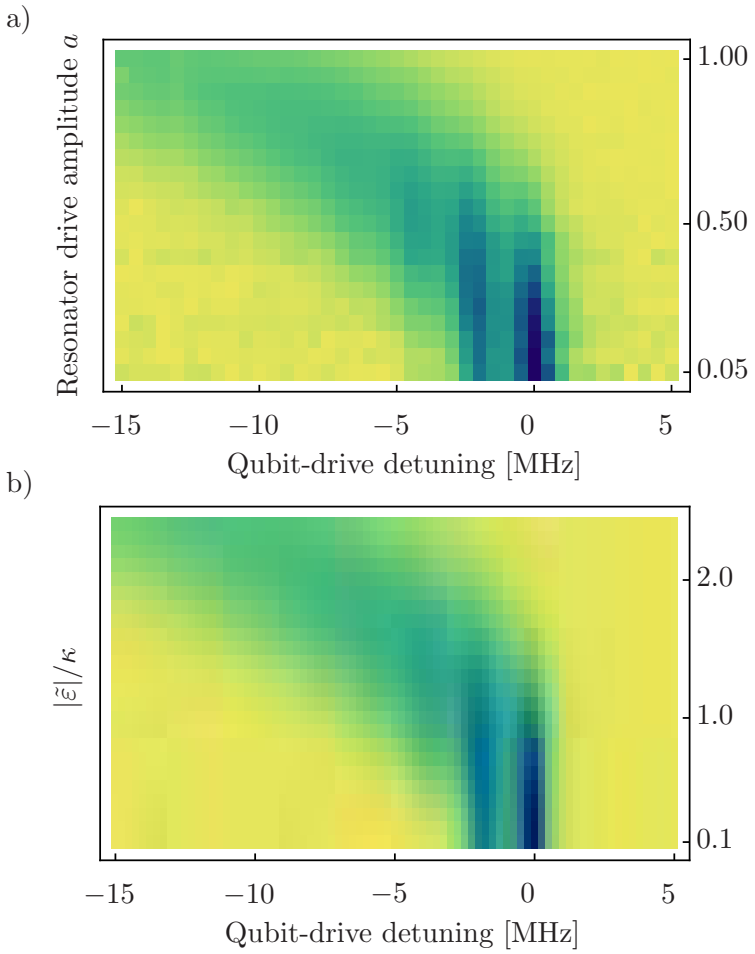

Figure 39: AC Stark shift measurement. (a) Experimental results of a qubit spectroscopy measurement versus the amplitude of the applied resonator drive. For better visibility, the detected signal is normalized to have the same maximum value for each amplitude of the resonator drive. Lighter colours correspond to higher voltage values. (b) Theoretical simulation based on the quantum master equation. The qubit spectrum is shown as a function of the dimensionless ratio between the resonator drive strength $\tilde{\varepsilon}$ and the decay rate κ.

The simulation agrees with the measured data reasonably well. The next step was to find for each measured qubit spectrum the most similar simulated spectrum, thus obtaining a correspondence between the signal amplitudes a and the drive strengths $\tilde{\varepsilon}$. Once again, the agreement between the experimental spectra and the theoretical predictions was relatively good although not perfect, as illustrated in Figs. 40a-c. The differences may be due to errors in some of the fixed parameters of the model.

We expect the relation between the drive signal amplitudes a and the corresponding drive strength $\tilde{\varepsilon}$ to be linear. Fig. 40d presents the complete set of data obtained by the above described procedure. The dependence of $\tilde{\varepsilon}/\kappa$ on a is indeed approximately linear

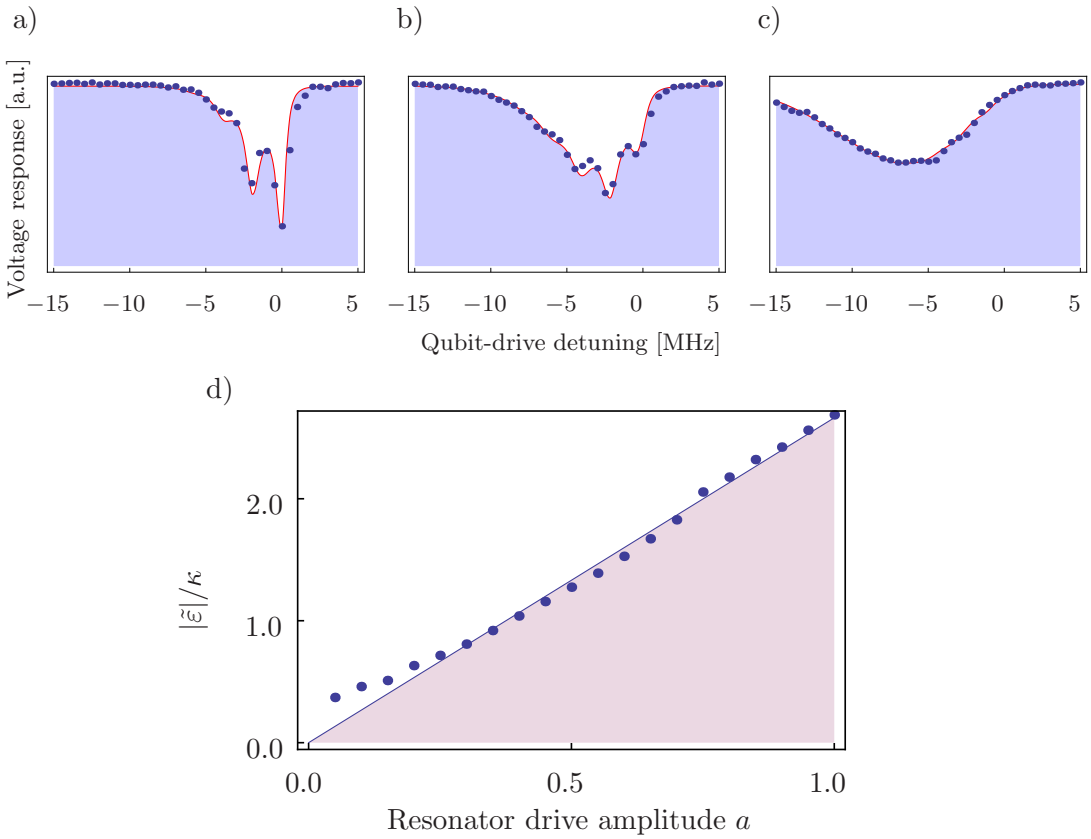

Figure 40: Measured and theoretically calculated qubit spectra. Plots (a), (b) and (c) give a comparison between the measured qubit spectroscopy results (blue points) and the corresponding theoretical spectra (red lines) for resonator drive amplitudes equal to (a) $a = 0.25$, (b) $a = 0.50$ and (c) $a = 0.75$. The drive strengths $\tilde{\varepsilon}/\kappa$ obtained from the fit in these three cases are respectively 0.72, 1.28 and 2.06. Plot (d) shows the resulting values of $\tilde{\varepsilon}/\kappa$ as a function of the drive amplitude a for all spectroscopy data sets. The blue line is a fitted linear function.

for higher values of a but it deviates from the linear relation for $a \ll 1$. This could once again be a consequence of errors in the input parameters of the theoretical model.

From the linear fit of the data in Fig. 40d we obtained the proportionality constant between a and $\tilde{\varepsilon}$ equal to $\tilde{\varepsilon}/a = 1.27$ MHz. The described calibration measurement is done with a resonant drive of the resonator. In our geometric phase experiment, where we need to drive the resonator off-resonantly and therefore more strongly to achieve the same field strength, we reduced the attenuation in the resonator drive line by 50 dB which results in an increase of $\tilde{\varepsilon}$ by a factor of $10^{5/2}$. The calibration parameter is then $\tilde{\varepsilon}/a = 400$ MHz.

5.3 Geometric phase measurements

We measured the resonator geometric in a simple Ramsey-type interference experiment as well as in a spin-echo measurement. These techniques were used in previous experiments focused on the geometric phase in a Cooper-pair box [17] and a transmon qubit [18].

5.3.1 Practical considerations

Although the theory behind the geometric phase of a harmonic oscillator and its measurement is relatively simple, choosing the appropriate parameters of the measurement can be in practice somewhat difficult. For example, the adiabaticity condition requires that the detuning δ between the resonator and the drive and the duration T of the cycle satisfy $\delta T \gg 1$. But at the same time, decoherence effects place a constraint on the time T, namely that $T \ll T_1, T_2$. As it turns out, the condition $T \ll 1/\kappa$ which we might expect to be imposed by resonator dissipation is not very critical if the drive signal is sufficiently off-resonant, specifically if $\delta \gg \kappa$.

According to Eqs. (38), the dynamical and geometric phase differences are proportional to $1/\delta - 1/(\delta + 2\chi)$ and $1/\delta^2 - 1/(\delta + 2\chi)^2$ – expressions which increase with the ratio χ/δ. To get appreciable phase differences to measure, the detuning δ should be as low as possible without violating the adiabatic condition $\delta \gg 1/T$. We might also hope to get larger phase differences by increasing the dispersive shift χ. Unfortunately, this quantity is constrained by the dispersive limit and typically cannot exceed values of several MHz.

An attempt to boost the phases by driving the resonator more strongly could result in a violation of the dispersive approximation which requires $n = |\tilde{\varepsilon}|^2/4\delta^2 \ll n_{\mathrm{crit}}$. It would also increase the pulse-induced dephasing discussed in Section 4.3.

We can see that there is a relatively complex system of conditions which should be satisfied if we want to observe the geometric phase and be able to describe the measurement by the simple theoretical model outlined in previous sections. After taking all of these requirements into consideration, we decided to use a resonator-drive detuning $\delta/2\pi = 40$ MHz and pulse length $T = 200$ ns as a starting point of our measurements.

5.3.2 Measurement of the total phase

The simplest possible measurement of the resonator geometric phase makes use of the Ramsey sequence described in Section 4.1. We used the resonator drive signal given in Eq. (39), which transports the resonator state along a circular path, and performed the measurement for different values of the dimensionless pulse amplitude a ranging from 0.0 to 1.0. This corresponds to values of the maximum drive strength $\varepsilon_0/2\pi$ between 0 and 400 MHz.

According to Eqs. (40), the total phase difference $\Delta\gamma$ grows quadratically with ε_0 and a. Therefore, if we take into account the dephasing effect (Section 4.3), we expect the final excited state population to oscillate as

$$p_e(a) = A\cos(\Delta\gamma_{\max}a^2 + \phi)\exp(-ka^2) + B, \tag{53}$$

where $\Delta\gamma_{\max}$ is the phase difference for $a = 1.0$. In the ideal case, the coefficients A and B would be both equal to $1/2$. In practice, A will be generally smaller due to qubit dephasing and B can be slightly different from the ideal value of $1/2$ because of errors in readout calibration. The phase offset ϕ accounts for a possible non-zero detuning δ_q between the qubit and the manipulation pulses which results in accumulation of an additional phase $\phi = \delta_q T$. The positive parameter k characterises the dephasing induced by the resonator pulse.

The outcome of the experiment agrees with the theoretically expected Ramsey oscillations given by Eq. (53) (see Fig. 41). The maximal accumulated phases extracted from the fit for the two orientations of the drive cycle, $\Delta\gamma_{\max} = (25.1 \pm 0.1)$ rad (counterclockwise) and $\Delta\gamma_{\max} = (34.0 \pm 0.1)$ rad (clockwise), clearly depend on the direction of the trajectory.

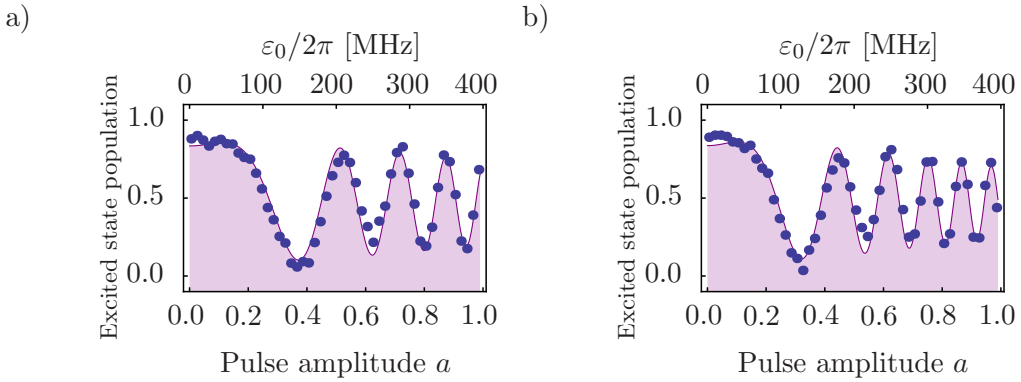

Figure 41: Ramsey measurement of the total accumulated phase. The plots shows the observed Ramsey oscillations of the excited state population as the accumulated phase difference $\Delta\gamma$ increases quadratically with the maximum drive amplitude ε_0 of the (a) counterclockwise and (b) clockwise circular pulse. The solid curves are fitted theoretical oscillations given by Eq. (53).

5.3.3 The total phase as a function of the pulse length

We used the Ramsey measurement to determine the total phase difference for several different lengths of the resonator drive pulse from 60 to 800 ns. As Fig. 42 illustrates, the Ramsey oscillations are robust against non-adiabatic effects and are clearly visible even for $T = 60$ ns which allows us to measure the phase well outside the adiabatic regime. Apart from the two circular drive pulses with opposite orientations, we have also measured the phase for the drive with fixed phase defined in Eq. (49) which in

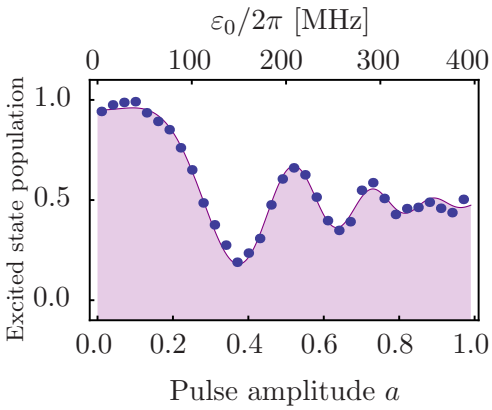

Figure 42: Ramsey oscillations for a strongly non-adiabatic pulse. The presence of clearly visible Ramsey oscillations for pulse lengths as short as $T = 60$ns in this plot demonstrates that the accumulated phase can be measured even in the non-adiabatic regime.

the adiabatic limit yields the same dynamical phase as the two cycles but no geometric phase.

The phase accumulated by the system when the resonator state is transported along a straight line is approximately proportional to the pulse length T (see Fig. 43). The phases for the two cyclic paths are shifted from this linear function by the geometric phase which – in the adiabatic limit – is independent of time and changes its sign when the orientation of the path is reversed.

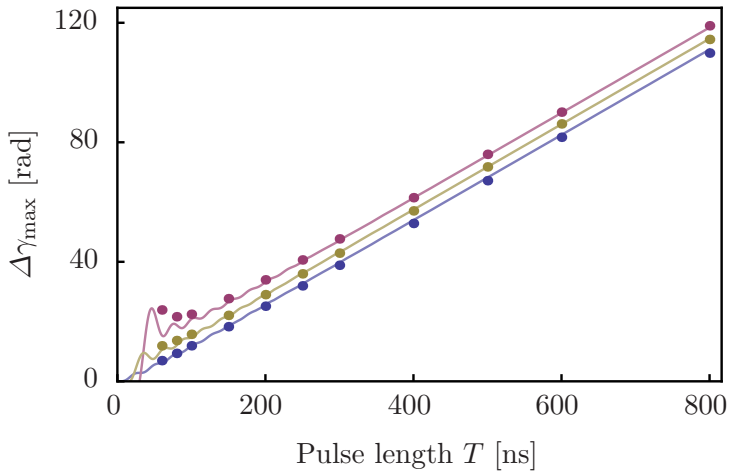

Figure 43: Total accumulated phase as a function of the pulse length. The phases measured in the Ramsey experiment for the counterclockwise (blue points) and clockwise (purple points) cycles and the drive pulse with fixed phase (yellow points) are plotted versus the duration T of the pulse. The solid lines are theoretical fits obtained from the exact solution of the harmonic oscillator evolution.

The experimental data in Fig. 43 are compared with the exact theoretical results from Eqs. (48) and (50) with the pulse amplitude ε_0 as a single free parameter fitted to the data. The theory reproduces some qualitative features of the measured non-adiabatic

corrections visible in the three shortest pulses – specifically the marked difference between the phases for the two orientations and the local minimum of the phase for the clockwise cycle. Nevertheless, the quantitative agreement is far from perfect. The cause of this discrepancy is not clear. One of the possible explanations could be a distortion of the drive pulses by some of the elements in the drive line.

Also, the value of the drive amplitude ε_0 resulting from the fit is about 370 MHz – about 10 % lower that the 400 MHz obtained from the calibration procedure descibed earlier. This could mean either that the calibration is not entirely correct or that the dynamical phase – which is the dominant component of the total phase and therefore determines the fitted amplitude ε_0 – for some reason deviates from the theoretically expected value.

It is quite straightforward to isolate the geometric phase difference $\Delta\gamma_g$ from the measured data – we simply fit linear functions of the form $cT + \Delta\gamma_g$ and $cT - \Delta\gamma_g$ to the phases for the two cycle directions. For this fit, we use only the data from the four longest pulses to ensure that the phases are sufficiently close to the adiabatic limit. This procedure yields the geometric phase difference $\Delta\gamma_g = (4.37 \pm 0.05)$ rad. The dynamical phase difference per unit time, which is simply the parameter c in the previous fit, is $\Delta\gamma_d/T = (143.2 \pm 0.3)\ \mathrm{rad} \cdot \mu\mathrm{s}^{-1}$.

The theoretically expected values calculated from Eqs. (40) using the calibrated pulse amplitude ε_0 are $\Delta\gamma_g = (4.24 \pm 0.11)$ rad and $\Delta\gamma_d/T = (165 \pm 4)\ \mathrm{rad} \cdot \mu\mathrm{s}^{-1}$. The estimated uncertainties of these quantities are based on the expected error of the measured dispersive shift parameter χ, which we expect to be the most important source of error in the calibration procedure. While the measured geometric phase agrees with the prediction quite well, the dynamical phase deviates from it by more than 10 %.

This result speaks in favour of the calibration being correct and the dynamical phase skewed by some unknown process although we cannot rule out the other possibility.

5.3.4 The phases for different path shapes

We repeated the measurement described above for other shapes of the drive path – a semicircle, a square and a figure-eight curve (see Fig. 44). The measured phases and their theoretically expected values are summarized in Table 1a and presented in a graphical form in Fig. 45.

As we have already seen for the circular path, the geometric phases are generally in a relatively good agreement with theoretical predictions whereas the dynamical phases are consistently smaller than the expected values. Quite interestingly, if we look at the *ratios* between the accumulated phases for the different paths then – as the values in Table 1b illustrate – the dynamical phases also match the theory reasonably well with the exception of the figure-eight curve.

There are several important things to bear in mind when inspecting the data in Table 1 and Fig. 45. The presented uncertainties of the measured phases include only

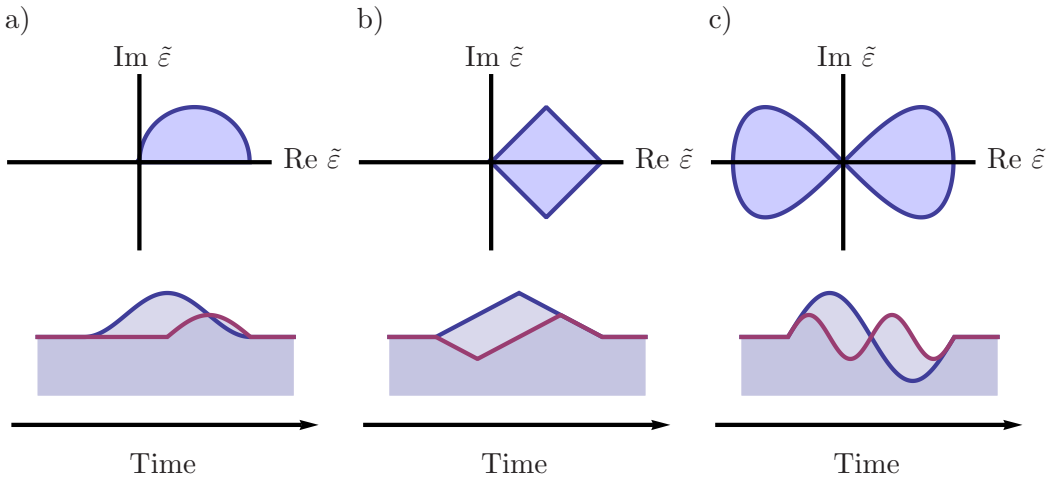

Figure 44: Alternative shapes of the drive path. (a) a semicircle, (b) a square and (c) a figure-eight curve. The plots in the top row show the trajectories and the bottom row presents the drive strength $\tilde{\varepsilon}$ as a function of time – its real and imaginary part are plotted respectively in blue and purple.

a)

	Geometric phase [rad]		Dynamical phase [rad·μs^{-1}]	
	Experiment	Theory	Experiment	Theory
Circle	4.37 ± 0.05	4.24 ± 0.11	143.1 ± 0.3	165 ± 4
Semicircle	2.06 ± 0.04	2.12 ± 0.06	123.4 ± 0.2	146 ± 4
Square	2.91 ± 0.07	2.70 ± 0.07	118.7 ± 0.3	138 ± 4
Figure-eight curve	-0.04 ± 0.04	0	150.4 ± 0.2	207 ± 6

b)

	Geometric phase ratio		Dynamical phase ratio	
	Experiment	Theory	Experiment	Theory
Semicircle / Circle	0.47 ± 0.01	0.5	0.862 ± 0.002	0.875
Square / Circle	0.67 ± 0.02	$0.637\ldots$	0.829 ± 0.003	$0.833\ldots$
Figure-eight / Circle			1.051 ± 0.003	1.25

Table 1: Comparison of the measured and theoretically predicted (a) phases and (b) phase ratios.

the estimated errors of the fit – any potential sources of systematic errors such as non-adiabatic corrections are not considered here. Also, the uncertainty of the drive strength calibration, being based on a numerical simulation, is quite difficult to estimate.

The larger deviation of the experimental result from theory in the case of the figure-eight trajectory might be related to the fact that this particular measurement was performed later than the remaining three. These were all done in the course of approximately 24 hours. It is possible that the outcome of the experiment is influenced by some parameters of the experimental setup which change over time. One particularly important change in the settings of the experiment made between the set of the first three measurements and the last one was calibration of the IQ mixers. The first three measurements were performed without proper mixer calibration due to technical problems. While this

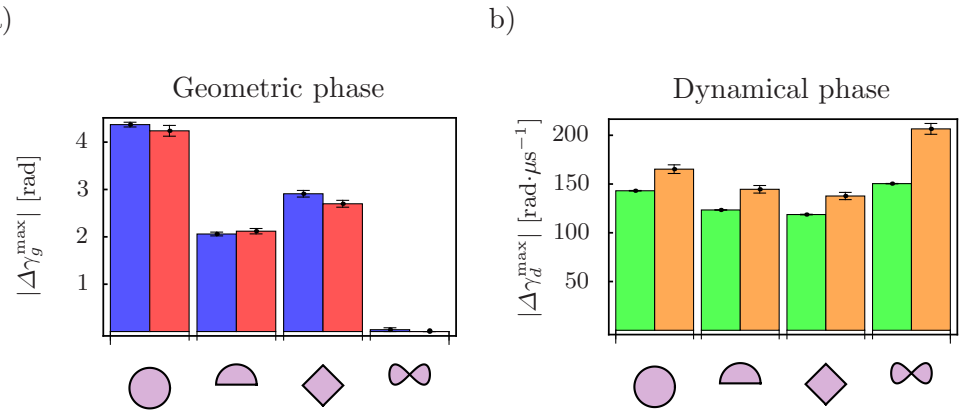

Figure 45: Measured phases for different path shapes. The bar charts show the measured and theoretically calculated (a) geometric and (b) dynamical phases for the four different path geometries represented by the symbols below the bars. The measured phases are displayed by the left-hand (blue and green) bars in each pair while the right-hand (red and orange) bars show the values predicted by theory.

could explain why the last measurement outcome is inconsistent with the other three, it is unclear how performing mixer calibration could lead to a *worse* agreement of the dynamical phase with theory.

5.3.5 Direct measurement of the geometric phase

The simple Ramsey measurement allows us to measure the total phase difference accumulated by the system but it does not provide means to separate the geometric and the dynamical phase except by subtracting the phases obtained from two *separate* Ramsey measurements. If we want to measure the geometric phase in a single experiment a slightly more complicated measurement sequence is needed.

The so-called *spin echo measurement*, well-known in the context of nuclear magnetic resonance, is a technique which can be used to subtract phases accumulated by a system. Like the Ramsey sequence, it starts by preparing a superposition state and applying the adiabatic pulse which causes the two components of the superposition state to acquire different phases. The resulting state

$$\frac{1}{\sqrt{2}}(\mathrm{e}^{\mathrm{i}(\gamma_d^{(g)}+\gamma_g^{(g)})}|g\rangle + \mathrm{e}^{\mathrm{i}(\gamma_d^{(e)}+\gamma_g^{(e)})}|e\rangle) \otimes |0\rangle \tag{54a}$$

is then transformed by a unitary operation $\hat{R}^y_{-\pi} = \exp(\mathrm{i}\pi\hat{\sigma}_y/2)$, which exchanges the states $|g\rangle$ and $|e\rangle$ and can be interpreted as a rotation by $-\pi$ around the y-axis on the Bloch sphere, into the state

$$\frac{1}{\sqrt{2}}(\mathrm{e}^{\mathrm{i}(\gamma_d^{(g)}+\gamma_g^{(g)})}|e\rangle - \mathrm{e}^{\mathrm{i}(\gamma_d^{(e)}+\gamma_g^{(e)})}|g\rangle) \otimes |0\rangle. \tag{54b}$$

Then the adiabatic cycle is applied again but this time in the opposite direction. Reversing the path leads to a sign-reversal of the geometric phase but leaves the dynamical phase unchanged. The vectors $|g\rangle \otimes |0\rangle$ and $|e\rangle \otimes |0\rangle$ therefore acquire phases $\gamma_d^{(g)} - \gamma_g^{(g)}$ and $\gamma_d^{(e)} - \gamma_g^{(e)}$ and the state of the system becomes

$$\frac{1}{\sqrt{2}} \mathrm{e}^{\mathrm{i}(\gamma_d^{(g)} + \gamma_d^{(e)})} (\mathrm{e}^{-\mathrm{i}\Delta\gamma_g} |e\rangle - \mathrm{e}^{\mathrm{i}\Delta\gamma_g} |g\rangle) \otimes |0\rangle. \tag{54c}$$

Applying the operation $\hat{R}^y_{-\pi/2}$ one more time and measuring the population of the qubit excited states then yields

$$p_e = \sin^2 \Delta\gamma_g,$$

from which the geometric phase difference $\Delta\gamma_g$ can be determined up to a sign and a shift by a multiple of π. The full spin echo sequence is shown in Fig. 46.

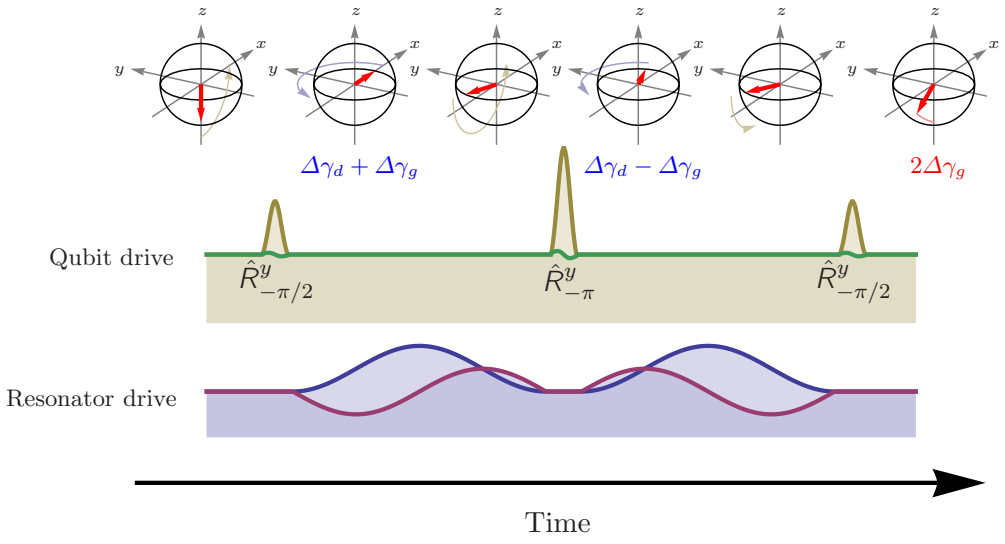

Figure 46: Spin echo measurement. The two outermost pulses applied to the qubit realize the unitary operation $\hat{R}^y_{-\pi/2}$, while the central pulse with double the amplitude realizes the operation $\hat{R}^y_{-\pi}$, exchanging the ground and the excited state of the qubit. The adiabatic resonator pulses enclosed between the qubit pulses both drive the resonator state along the same closed path but in opposite directions. The Bloch state pictures schematically show the initial and the final state of the qubit as well as the states between the pulses. The axial angle $2\Delta\gamma_g$ accumulated during the adiabatic cycles is mapped to an inclination angle with respect to the z-axis by the third qubit pulse.

Just like for the Ramsey sequence, replacing the last gate and the simple excited state population measurement by qubit tomography allows us to extract the sign of $\Delta\gamma_g$ from the two spin projections

$$\langle \hat{\sigma}_x \rangle = -\cos 2\Delta\gamma_g,$$
$$\langle \hat{\sigma}_y \rangle = -\sin 2\Delta\gamma_g.$$

Similarly to Eq. (53), if we take dephasing and possible imprecision of readout calibration into consideration, we expect the projections to vary according to

$$\langle \hat{\sigma}_x + \mathrm{i}\hat{\sigma}_y \rangle = -A \exp(2\mathrm{i}\Delta\gamma_g^{\max} a^2 - ka^2) + B, \tag{55a}$$

$$\langle \hat{\sigma}_z \rangle = C, \tag{55b}$$

where $\Delta\gamma_g^{\max}$ is the geometric phase difference accumulated for the maximum drive pulse amplitude $a = 1.0$, k determines the dephasing induced by the resonator pulse and the constants A, B and C are in the ideal case equal to $A = 1$, $B = 0$ and $C = 0$. In reality, C will be negative due to qubit dissipation and the magnitude of A reduced because of qubit dephasing. Its phase, $\arg A$, corresponds to a residual phase accumulated by the qubit during the spin echo sequence in the absence of the resonator drive pulse. While this phase should be ideally zero, i.e. A should be a real number, we account for the possibility of the spin echo sequence being non-ideal by allowing A to be complex.

Figs. 47 show the results of a spin echo measurement for a circular drive trajectory with detuning $\delta/2\pi = 40$ MHz and pulse length $T = 200$ ns together with the fitted theoretical functions. In this case, the calculated offset parameter B is subtracted from the measured data and set to zero in the theoretical curves.

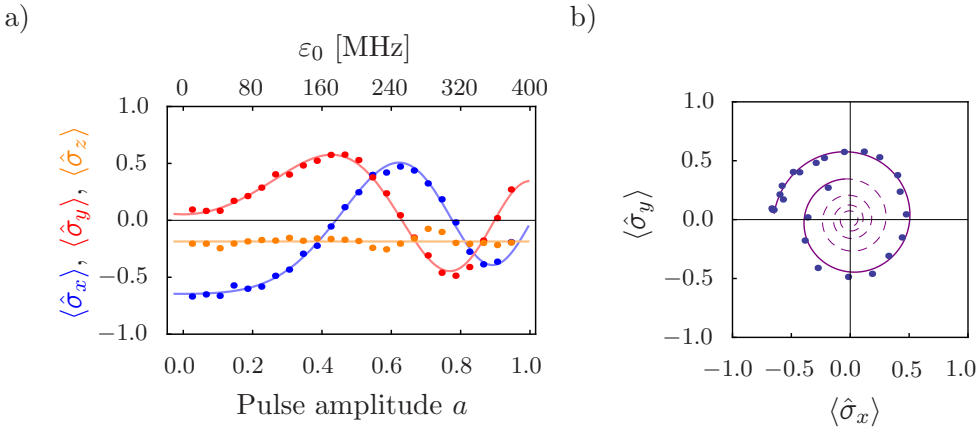

Figure 47: Ramsey oscillations in the spin echo measurement. (a) Three projections of the final spin in a spin echo measurement of the geometric phase onto the x (in blue), y (in red) and z (in orange) axes as a function of the resonator drive amplitude. The measurement was done for $\delta/2\pi = 40$ MHz and $T = 200$ ns. (b) The curve traced by the final spin in the xy plane as the drive amplitude increases. The solid lines are fitted functions of the form given in Eqs. (55).

We can see in Fig. 47b that as the drive amplitude increases and the geometric phase difference accumulated by the system grows, the Bloch vector rotates around the z axis and decreases in magnitude due to dephasing.

While we could use the fits to determine the maximum accumulated geometric phase difference $\Delta\gamma_g^{\max}$ in the same way as for the Ramsey measurement, we can now also extract the geometric phase directly from the x and y spin projections using the relation

$$2\Delta\gamma_g = \arg(-\langle\hat{\sigma}_x + \mathrm{i}\hat{\sigma}_y\rangle).$$

The phase $2\Delta\gamma_g$ can be obtained simply as the angle of rotation between the Bloch vector and the axis $-x$ in Fig. 47b. Although in this case we could in principle do completely without the theoretical fit, we still use it to determine the population offset given by the parameter B which we then subtract from the measured data before calculating the phase.

The results of two measurements for resonator drive pulse lengths $T = 200$ ns and $T = 400$ ns are presented in Figs. 48. This time we plot the phase against the area A_a enclosed by the trajectory of the dimensionless drive amplitude a to illustrate that the relation between these quantities is with a good precision linear as expected.

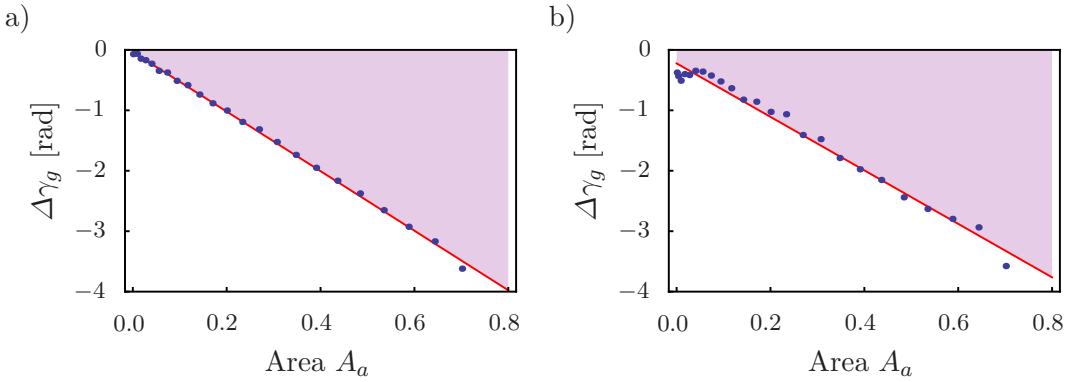

Figure 48: Measured geometric phase versus the area enclosed by the circular trajectory. The detuning is $\delta/2\pi = 40$ MHz and pulse lengths (a) $T = 200$ ns and (b) $T = 400$ ns. The solid red lines represent fitted linear functions.

The proportionality constants between the geometric phase difference $\Delta\gamma_g$ and the area A_a obtained from the fitted linear functions are $\Delta\gamma_g/A_a = (-4.93 \pm 0.03)$ rad for $T = 200$ ns and $\Delta\gamma_g/A_a = (-4.43 \pm 0.11)$ rad for $T = 400$ ns. The difference between these values is probably due to non-adiabatic corrections.

Based on Eqs. (40) and the drive strength calibration constant $\varepsilon_0/a = 400$ MHz, the value predicted by theory for the geometric phase in the adiabatic limit is $\Delta\gamma_g/A_a = (-5.40 \pm 0.14)$ rad. The agreement between theory and experimental results is worse than for the simpler Ramsey experiment.

It is possible that non-adiabatic effects could lead to a systematic shift of the phase measured in a spin-echo sequence. If the first resonator drive cycle is not ideally adiabatic it generally leaves the resonator in a coherent state $|\alpha\rangle$ with a quadrature $\alpha \neq 0$ which depends on the qubit state. The second drive cycle will therefore start in a state in which the resonator and the qubit are entangled. This could potentially change the phase accumulated during the second cycle.

Despite the discrepancy between the experimental results and theoretical predictions, the data shown in Figs. 48 clearly show that the geometric phase is very insensitive to the drive pulse length. In this particular example, its value changes by just 10 % when the duration of the pulse doubles.

5.3.6 Observed non-linearity of the geometric phase

Although the measured data presented in Figs. 48 apparently obey the expected linear relation between the geometric phase and the area enclosed by the drive path, we have also observed what appears to be a deviation from this simple dependence.

After decreasing the detuning $\delta/2\pi$ between the resonator and the drive frequency to 30 MHz, we have measured the geometric phase plotted in Fig. 49. It seems to depend on the area A_a in a slightly non-linear way. This effect is not very pronounced but if we compare the geometric phase obtained for the maximum drive amplitude $a = 1.0$ with the value predicted by theory, we find that it is more than 30 % higher. Considering that the measured phases presented in Section 5.3.5 were *lower* than the values calculated from theory, this indicates that we might be indeed looking at some additional correction to the phases, different from what causes the deviations in Section 5.3.5.

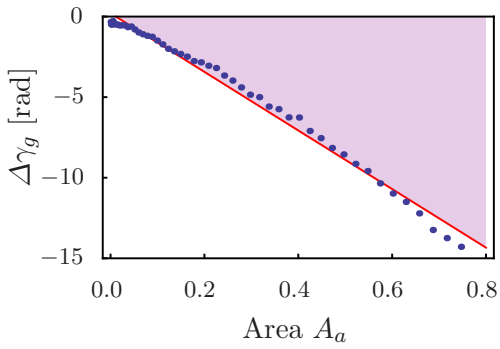

Figure 49: Observed non-linearity of the geometric phase. This plot shows the measured geometric phase as a function of the area enclosed by the circular trajectory of the drive amplitude for detuning $\delta/2\pi = 30$ MHz and pulse length $T = 200$ ns. The dependence of the phase on the area seems to deviate from the linear fit.

We suspect that this non-linearity could be related to the fact that the maximum number of photons present in the resonator during the drive pulse is relatively large. It is given by $n_{\max} = \varepsilon_0^2/4\delta^2$ which for $\delta/2\pi = 30$ MHz gives us approximately $n_{\max} = 45$. The critical photon number, which determines the domain of validity of the dispersive approximation, is in our system close to $n_{\text{crit}} = 140$. Violation of the dispersive approximation would certainly cause a shift of the geometric phase. It should be relatively straightforward to obtain an approximation of this correction using perturbation theory and check whether it can account for the observed increase of the geometric phase.

5.3.7 Measurement of the pulse-induced dephasing

The dephasing induced by the resonator pulse (Section 4.3) was observed in most of our measurements. We have therefore performed a separate experiment in an attempt to quantify it and compare the results with our theoretical expectations.

In the Ramsey measurement of the phase, the state of the qubit right after the resonator drive pulse is characterised by its Bloch vector $\vec{b}$ lying in the xy plane. Applying the operation $\hat{R}^y_{-\pi/2}$ and measuring the excited state population allowed us to determine the projection of the Bloch vector onto the x axis. By changing the phase of the second qubit manipulation pulse, we can measure any desired projection in the xy plane. If we sweep the phase of the pulse from 0 to 2π, the measured projection undergoes one oscillation whose amplitude is equal to $|\vec{b}|$ – the magnitude of the Bloch vector. We can perform this measurement with different amplitudes of the resonator pulse and determine the visibility of the population oscillations for each of them. In this way we obtain the magnitude of the Bloch vector after the resonator pulse as a function of the pulse amplitude.

The theoretical result derived in Section 4.3 tells us that a resonator drive pulse with amplitude a should reduce $|\vec{b}|$ by a factor of the form $\exp(-ka^2)$. Here k is a constant depending on the shape of the drive path, the proportionality constant between ε_0 and a, the detuning δ and the dispersive shift parameter χ. Its exact form is rather complicated but we generally expect it to decrease with the length of the pulse because longer, more adiabatic pulses result in less entanglement of the qubit and the resonator, which is the key factor behind this dephasing effect.

Two plots showing how the dephasing changes with the amplitude of the pulse are presented in Fig. 50.

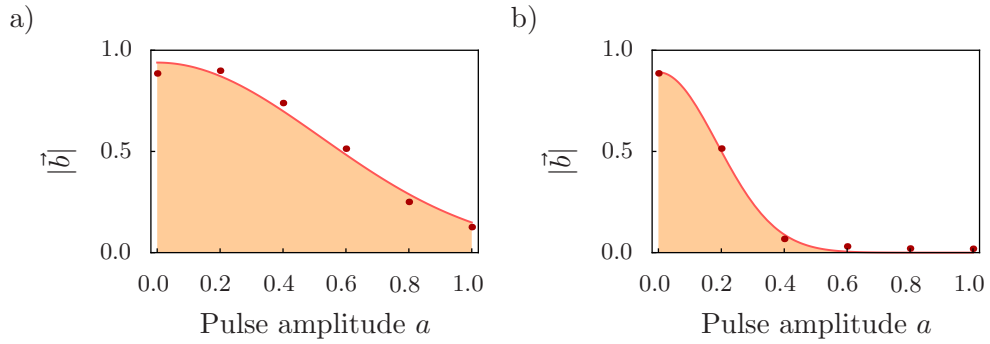

Figure 50: Dephasing induced by the resonator pulse. The plots show the magnitude of the Bloch vector $\vec{b}$ after the resonator drive pulse as a function of the pulse amplitude and demonstrate that the pulse causes dephasing of the qubit. The lengths of the pulses are (a) $T = 60$ ns and (b) $T = 40$ ns. The solid lines represent the theoretically expected dependence of the form $A\exp(-ka^2)$ with the parameters A and k fitted to the data.

The measured data clearly confirm that the dephasing increases with the pulse amplitude. The decrease in the magnitude of the Bloch vector seems to be consistent with the theoretically predicted dephasing factor $A\exp(-ka^2)$. The constant $A < 1$ describes dephasing coming from other sources which does not depend on the amplitude. A comparison of the plots in Fig. 50 also supports our theoretical expectation that the effect is weaker for longer pulses.

6 Conclusion

6.1 Summary of the results

Over the course of this four months' work, we have designed and performed an experiment to analyze the geometric phase of an adiabatically driven harmonic oscillator – a microwave transmission line resonator in a superconducting circuit QED system. We made use of a qubit dispersively coupled to the resonator which makes the value of the resonator phase dependent on the qubit state. This allowed us to measure the phase difference in a simple Ramsey interference experiment.

In this way, we have successfully observed the geometric phase and demonstrated its dependence on the shape and direction of the trajectory traced by the state of the system in its Hilbert space only, insensitive to dynamical parameters of the evolution. We have studied the behaviour of the phase both in the adiabatic and non-adiabatic regime and found that it is robust against non-adiabatic effects. Its measurement and potential utilisation is, however, complicated by entanglement between the qubit and the resonator which induces dephasing of the reduced qubit state.

In this thesis, we present a theoretical introduction to superconducting qubits and circuit QED and an overview of the geometric phase – both in its general form and in the specific context of our circuit QED system. Thanks to the exact integrability of the harmonic oscillator, we are able to derive analytical expressions for the evolution of the system as well as the accumulated phases and describe the processes theoretically even in the non-adiabatic regime to compare the theoretical predictions with experimental results.

The geometric phase determined from a set of simple Ramsey measurement is in good agreement with theory but the dynamical phase is consistently lower than predicted. By measuring the phase for several different path geometries, it is shown that the geometric phase is proportional to the area enclosed by the trajectory of the coherent state in the quadrature plane and that the dynamical phase scales with the time integral of the squared drive amplitude.

The geometric phase measured in a spin echo experiment also shows good linear scaling with the area enclosed by the path, but its values differ from those predicted by theory. As of now, we do not have a good explanation for the differences between the measured phases and theoretical predictions. We observe a small deviation from the linear relation between the phase and the enclosed area in a measurement with smaller detuning of the drive signal from the resonator frequency – we suspect that this could be a sign of a potentially interesting regime in which the dispersive approximation of qubit-resonator interactions starts to break down and the resonator can no longer be described as an ideal harmonic system.

In addition, we also investigate the dephasing effects of qubit-resonator entanglement caused by non-adiabaticity of the resonator drive pulse – specifically its dependence on

the resonator drive amplitude and the length of the drive pulse – and find qualitative agreement with the theoretically expected behaviour. The effect is enhanced as the drive amplitude increases and as the pulses become less adiabatic.

6.2 Outlook

We believe that the simplicity and exact integrability of the harmonic oscillator make it a very convenient system for studying the geometric phase both experimentally and theoretically. For example, by adding artificially generated noise to the resonator drive signal, one can easily study its effects on the phase and compare them with theoretical predictions. Another potentially interesting topic to address could be the relation between adiabaticity and differentiability of the drive path discussed in this thesis.

It would of course be highly desirable to find an explanation of the discrepancy between some of our phase measurement and theoretical predictions. We therefore plan to double-check our calibrations and determine whether the drive pulses do not get distorted on the way from the AWG to the sample.

In future experiments, we would like to extend our measurement and try to observe the two-qubit geometric phase. This may require a different sample with parameters specifically designed to increase our chances of seeing this presumably weak effect.

We also want to look closer at the transition regime in which the dispersive approximation ceases to be valid. This could allow us to measure the geometric phase of a weakly anharmonic oscillator and possibly compare the results with the geometric phase measured in a transmon qubit.

These are just a few possible directions for future investigation of the harmonic oscillator geometric phase. We think they illustrate that this area definitely offers many intriguing topics to study.

A Geometric phase in the context of differential geometry

It was noted by Simon [16] immediately after Berry's insightful discovery of the geometric phase that it can be conveniently described in the language of differential geometry [58] as a result of the non-trivial geometric properties of complex Hilbert spaces.

A *projective Hilbert space* corresponding to a given Hilbert space $\mathscr{H}$ is a set $\mathscr{H}/\mathbb{C}$ of equivalence classes on $\mathscr{H}$ containing vectors which only differ by multiplication by a complex number. In other words, it is the set of all *physically distinct* states.

The full Hilbert space $\mathscr{H}$ can be viewed as collection of *rays* – classes of physically equivalent states – which are isomorphic to $\mathbb{C}$. Each ray then obviously corresponds to an element of the projective space $\mathscr{H}/\mathbb{C}$. Such mathematical structure is known in differential geometry as a *fibre bundle* [58]. Simply speaking, it is a manifold $\mathscr{M}$ (called the *base space*, in our case the projective space) with a copy of a space F (called the *fibre*, in our case the set of all equivalent states) embedded at each point of $\mathscr{M}$.

As we have mentioned earlier, the adiabatic theorem in the case of a non-degenerate energy spectrum determines the state vector only up to a complex phase factor, i.e. it specifies the path followed by the state in the projective base space $\mathscr{H}/\mathbb{C}$. Determining the phase associated with the evolution is in the language of differential geometry equivalent to finding the corresponding path in the bundle $\mathscr{H}$.

For general fibre bundles, elements of different fibres cannot be directly compared since they belong to different instances of the fibre space F. In order to define transport in the bundle in a meaningful way, an additional geometrical structure is needed. A so-called *connection* defines a correspondence between elements of a fibre at a point $x \in \mathscr{M}$ in the base space and elements of fibres in an infinitesimal neighbourhood of x. For bundles with a linear fibre space F – so-called *vector bundles* – a connection allows to add and subtract elements of infinitesimally separated fibres and thereby define a *covariant derivative* and *parallel transport* on the bundle.

A.1 Parallel transport

As we will see, in our case where the bundle is the Hilbert space $\mathscr{H}$, the connection is related to the inner product on $\mathscr{H}$ and the evolution of the state vector after eliminating the trivial dynamical phase is given by the corresponding parallel transport. The connection can in general be *curved*, i.e. an element parallel-transported along a closed curve in the projective base space back to the original fibre need not be the same as the initial element, as shown schematically in Fig. 51. This is nothing else than a statement that there is a non-zero geometric phase, which can therefore be viewed as a consequence of a curved connection on the Hilbert space fibre bundle.

Let us now derive the form of the covariant derivative which determines the adiabatic evolution of the state vector $|\psi(t)\rangle = \mathrm{e}^{\mathrm{i}\gamma(t)}|\varphi(t)\rangle$ expressed in Eqs. (22). We can eliminate

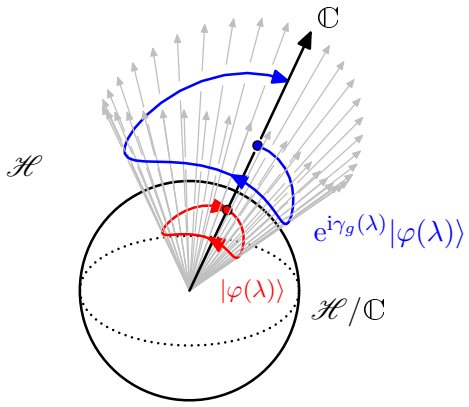

Figure 51: Adiabatic evolution as a parallel transport in a fibre bundle. The eigenvector $|\varphi(\lambda)\rangle$ of the adiabatically changing Hamiltonian determines the path (in red) followed by the state in the projective Hilbert space $\mathscr{H}/\mathbb{C}$. The path in the Hilbert space $\mathscr{H}$ itself (in blue) is given by a connection on the bundle of rays induced naturally by the inner product. This connection is in general not flat and can result in a non-zero cyclic geometric phase.

the dynamical evolution of the state if we multiply $|\psi(t)\rangle$ by $e^{-i\gamma_d(t)}$, thereby isolating the purely geometric evolution. Substituting the resulting modified state vector $|\psi_g(t)\rangle$ into the Schrödinger equation yields

$$\frac{d|\psi(t)\rangle}{dt} = e^{i\gamma_d(t)}\left(i\frac{d\gamma_d(t)}{dt} + \frac{d}{dt}\right)|\psi_g(t)\rangle = -\frac{i}{\hbar}\hat{H}(t)|\psi(t)\rangle.$$

Multiplying this equation by $\langle\varphi(t)|$ and using Eq. (22a) for the dynamical phase $\gamma_d(t)$ then results in the simple relation

$$\langle\varphi(t)|\frac{d}{dt}|\psi_g(t)\rangle = 0. \tag{56}$$

Once again, the time in this equation can be replaced by an arbitrary parametrization λ of the path the vector traces in the Hilbert space. We would like to find a covariant derivative ∇_λ for which the evolution of $|\psi_g(\lambda)\rangle$ is simply a parallel transport. Based on Eq. (56), it is not difficult to guess the correct form of ∇_λ and show that it indeed has all the properties required for a derivative

$$\nabla_\lambda|u(\lambda)\rangle = \hat{P}_{u(\lambda)}\frac{d}{d\lambda}|u(\lambda)\rangle. \tag{57}$$

Here $|u(\lambda)\rangle$ is an arbitrary, not necessarily normalized vector from $\mathscr{H}$ and $\hat{P}_{u(\lambda)}$ is the projector onto $|u(\lambda)\rangle$. With this definition, Eq. (56) can be shown to be equivalent to the parallel transport equation $\nabla_\lambda|\psi_g(\lambda)\rangle = 0$.

This form of parallel transport has a very natural interpretation. It means that the derivative of $|\psi_g(\lambda)\rangle$ is at each point of the adiabatic evolution perpendicular to the eigenvector $|\varphi(\lambda)\rangle$. Since $|\psi_g(\lambda)\rangle$ has to lie in the one-dimensional space spanned by

$|\varphi(\lambda)\rangle$, the vector $|\psi_g(\lambda)\rangle$ can be obtained from $|\psi_g(\lambda - \mathrm{d}\lambda)\rangle$ by projection onto $|\varphi(\lambda)\rangle$. Thus, the evolution of the vector $|\psi_g(\lambda)\rangle$ is in some sense given by continuously projecting $|\psi_g(\lambda)\rangle$ onto the changing eigenvector $|\varphi(\lambda)\rangle$, a process which can be perhaps somewhat simplistically expressed by the relation

$$|\psi_g(\lambda_2)\rangle = \mathscr{P} \prod_{\lambda\in[\lambda_1,\lambda_2]} \hat{P}_{\varphi(\lambda)} |\psi_g(\lambda_1)\rangle, \tag{58}$$

where the symbol $\mathscr{P}$ stands for path-ordering of the projectors. This process is very similar to the standard parallel transport of vectors in a curved manifold embedded in a Euclidean space. There, the transported vector is being continuously projected onto the tangent space to the manifold at each point of the path. But while this kind of parallel transport for a one-dimensional manifold is trivial due to the tangent space being real, our case of adiabatic transport is more interesting. Even though the eigenspace spanned by $|\varphi(\lambda)\rangle$ onto which we project is also one-dimensional, the fact that the space is complex makes all the difference and can give rise to a non-trivial geometric phase.

It may be noteworthy that Eq. (58) determines the evolution of $|\psi_g(\lambda)\rangle$ in a gauge-invariant way because the projectors $\hat{P}_{\varphi(\lambda)} = |\varphi(\lambda)\rangle\langle\varphi(\lambda)|$ do not depend on the phases of the eigenvectors $|\varphi(\lambda)\rangle$. It also makes manifest the gauge-transformation properties of the geometric phase. Since $|\psi_g(\lambda)\rangle = \mathrm{e}^{\mathrm{i}\gamma_g(\lambda)}|\varphi(\lambda)\rangle$, the geometric phase clearly obeys the relation

$$\mathrm{e}^{\mathrm{i}(\gamma_g(\lambda_2)-\gamma_g(\lambda_1))} = \langle\varphi(\lambda_2)|\mathscr{P} \prod_{\lambda\in[\lambda_1,\lambda_2]} \hat{P}_{\varphi(\lambda)} |\varphi(\lambda_1)\rangle$$

and as the product of projectors is gauge-invariant, the phase factor on the left-hand side transforms under a change of gauge in the same way as the inner product $\langle\varphi(\lambda_2)|\varphi(\lambda_1)\rangle$, in accordance with the transformation property discussed previously in Section 3.2.

This shows one of the strengths of the differential geometry framework as a tool to study inherently geometric properties of objects without the need to resort to any specific reference frame (gauge) or coordinate system. Sometimes it can offer more insight into the nature and origin of the geometric phase. For example, the described picture of adiabatic evolution as continuous projection onto the energy eigenspace is probably more intuitive than the treatment using Schrödinger equation (Eq. (22b)) which essentially conveys the same concept in a gauge-dependent way.

On the other hand, the abstract formalism of differential geometry is not particularly useful for actual calculations of the geometric phase which usually need to be done for some specific gauge choice and a system of coordinates within the projective space. In most cases, the calculation eventually boils down to evaluating the integral in Eq. (22b).

The differential-geometric approach also lends itself to generalization of the previous results to the case of degenerate eigenvectors. As discussed before, if the adiabatically evolving Hamiltonian $\hat{H}(t)$ has a degenerate eigenspace $\mathscr{S}(t)$ then a state vector initially in $\mathscr{S}(t)$ will be restricted to it. But unless there is some additional conserved quantity $\hat{A}$ whose presence splits $\mathscr{S}(t)$ into one-dimensional eigenspaces of $\hat{A}$ not connected by

the Hamiltonian, the evolution of the state vector within $\mathscr{S}(t)$ is not fully determined by the adiabatic theorem.

It can be easily shown that the parallel transport law (Eq. (56)) remains valid even in the degenerate case and holds if $|\varphi(t)\rangle$ is *any* vector in $\mathscr{S}$. Consequently, the covariant derivative governing the adiabatic transport then has a form almost identical to Eq. (57). The only difference is that the projector $\hat{P}_{u(\lambda)}$ is replaced by $\hat{P}_{\mathscr{S}(\lambda)}$ – a projector onto the eigenspace $\mathscr{S}(\lambda)$, i.e.

$$\nabla_\lambda |u(\lambda)\rangle = \hat{P}_{\mathscr{S}(\lambda)} \frac{\mathrm{d}}{\mathrm{d}\lambda} |u(\lambda)\rangle. \tag{59}$$

Just like in the non-degenerate case, the corresponding parallel transport can be interpreted as continuous orthogonal projection of the modified state vector $|\psi_g(\lambda)\rangle$ onto $\mathscr{S}(\lambda)$. The fact that a cyclic evolution starting and ending in the same degenerate eigenspace $\mathscr{S}$ can lead to a non-trivial rotation in $\mathscr{S}$ is in this case perhaps even more obvious than for the simpler one-dimensional parallel transport. The connection can be curved even for *real* degenerate eigenspaces. In that special case we have a situation *completely identical* to the parallel transport in Riemannian manifolds, previously mentioned only to illustrate the state vector transport given by Eq. (58). Now we see that this analogy is in certain cases rather accurate.

There is one particular quantum system commonly studied in the context of holonomic quantum computation – the so-called *tripod system* [46]. Its Hamiltonian has a two-fold degenerate eigenspace which can be arbitrarily manipulated within a fixed three-dimensional space. If the subspace is adiabatically varied in such a way that it always remains real, the evolution of the state vector $|\psi_g(\lambda)\rangle$ is equivalent to the parallel transport on a classical textbook-example of a curved manifold – a sphere. The non-trivial nature of such transport is clear to anyone who has ever wondered at the principle of Foucault's pendulum. It is perhaps partly due to this convenient and simple geometric interpretation that the tripod system is currently a popular basis for proposals of potential experimental realizations of holonomic quantum computation.

Fig. 52 presents this simple case of parallel transport. It shows a vector being parallel-transported along a closed curve on the surface of a sphere, returning to the point of origin rotated by a non-zero angle. It also illustrates how the vector evolves by successive projections onto infinitesimally separated tangent spaces.

A.2 The parallel transport law in a specific basis

In order to perform real calculations of the geometric phase in the degenerate case, we need to express the covariant derivative given by Eq. (59) in some specific basis $|\varphi_1(\lambda)\rangle, |\varphi_2(\lambda)\rangle, \ldots$ of the degenerate eigenspace. If we denote the components of the modified state vector $|\psi_g(\lambda)\rangle$ in this basis by $c_1(\lambda), c_2(\lambda), \ldots$ then the parallel transport

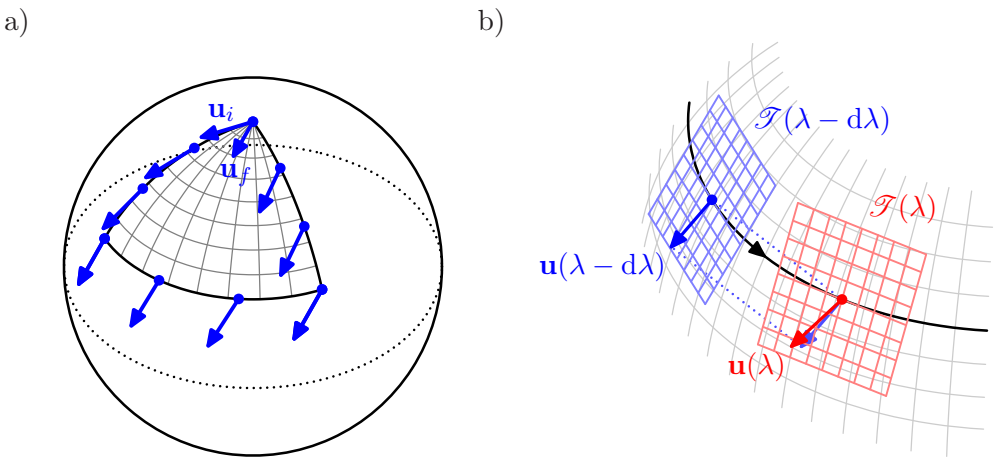

Figure 52: Parallel transport on a sphere. (a) The vector $\mathbf{u}_i$ is transported along a closed curve on the surface of a sphere (counterclockwise). The final vector $\mathbf{u}_f$ upon returning to the original point is different from $\mathbf{u}_i$. (b) The parallel transport can be interpreted as a continuous projection of the vector $\mathbf{u}(\lambda)$ onto the tangent space $\mathscr{T}(\lambda)$, i.e. the red vector $\mathbf{u}(\lambda)$ is obtained by projecting the blue vector $\mathbf{u}(\lambda - \mathrm{d}\lambda)$ onto the tangent space $\mathscr{T}(\lambda)$.

equation $\nabla_\lambda |\psi_g(\lambda)\rangle = 0$ takes the form

$$\sum_i (\nabla_\lambda c_i(\lambda))|\varphi_i(\lambda)\rangle + c_i(\lambda)\nabla_\lambda|\varphi_i(\lambda)\rangle = 0.$$

As the components $c_i(\lambda)$ are scalars, the covariant derivative acts on them as a standard total derivative. After multiplying the previous equation by $\langle\varphi_j(\lambda)|$, we obtain

$$\frac{\mathrm{d}c_j(\lambda)}{\mathrm{d}\lambda} + \sum_i c_i(\lambda)\langle\varphi_j(\lambda)|\nabla_\lambda|\varphi_i(\lambda)\rangle = 0.$$

This equation can be conveniently expressed in a matrix form as

$$\frac{\mathrm{d}\mathbf{c}(\lambda)}{\mathrm{d}\lambda} = \mathbf{A}(\lambda)\cdot\mathbf{c}(\lambda), \tag{60}$$

where $\mathbf{c}(\lambda)$ is a vector of the components $c_i(\lambda)$ and the elements of the matrix $\mathbf{A}(\lambda)$ are defined as $A_{ji}(\lambda) = -\langle\varphi_j(\lambda)|\nabla_\lambda|\varphi_i(\lambda)\rangle$ or, after using the definition of ∇_λ given in Eq. (59) and considering that $\hat{P}_{\mathscr{S}(\lambda)}|\varphi_j(\lambda)\rangle = |\varphi_j(\lambda)\rangle$, as

$$A_{ji}(\lambda) = -\langle\varphi_j(\lambda)|\frac{\mathrm{d}}{\mathrm{d}\lambda}|\varphi_i(\lambda)\rangle. \tag{61}$$

The solution of Eq. (60) can be formally written in terms of a path-ordered exponential,

$$\mathbf{c}(\lambda_2) = \mathbf{U}(\lambda_2,\lambda_1)\cdot\mathbf{c}(\lambda_1) = \left(\mathscr{P}\exp\int_{\lambda_1}^{\lambda_2}\mathbf{A}(\lambda)\,\mathrm{d}\lambda\right)\cdot\mathbf{c}(\lambda_1). \tag{62}$$

We can immediately recognize the matrix $\mathbf{U}(\lambda_2, \lambda_1)$ relating $\mathbf{c}(\lambda_1)$ to $\mathbf{c}(\lambda_2)$ as a generalization of the geometric phase factor $\mathrm{e}^{\mathrm{i}(\gamma_g(\lambda_2)-\gamma_g(\lambda_1))}$ (Eq. (22b)) in the simple non-degenerate case. There the vector $\mathbf{c}(\lambda)$ has only one component equal to $\mathrm{e}^{\mathrm{i}\gamma_g(\lambda)}$, and the matrix $\mathbf{A}(\lambda)$ acts as a simple scalar multiplication. This allows us to drop the path ordering in Eq. (62) and arrive at Eq. (22b). On the other hand, such simplification may not be possible in the degenerate case because the matrices $\mathbf{A}(\lambda)$ for different values λ need not commute. For this reason, the unitary matrix $\mathbf{U}(\lambda_2, \lambda_1)$ is often called *non-abelian geometric phase*.

Just like in the non-degenerate case, the matrix analogue of the geometric phase factor can be expressed using a line integral in a space of parameters $x_1, x_2, \ldots, x_d$ of the Hamiltonian, namely as

$$\mathbf{U} = \mathscr{P} \exp \int_P \mathbf{A}_i(\mathbf{x})\, \mathrm{d}x_i, \text{ where}$$
$$\mathbf{A}_i(\mathbf{x}) = -\langle \varphi_j(\mathbf{x}) | \frac{\partial}{\partial x_i} | \varphi_i(\mathbf{x}) \rangle.$$

Here we explicitly write the index i, enumerating the parameters $x_1, x_2, \ldots, x_d$, in order to avoid confusion with the matrix indices of $\mathbf{A}_i(\mathbf{x})$ acting on the components $c_1, c_2, \ldots$ of the state vector. The matrix-valued vector $\mathbf{A}_i(\mathbf{x})$ is usually called *gauge potential* [40] because it shares all the properties of this key object of gauge field theories.

All the gauge-dependent results derived here for the non-abelian geometric phase can be of course also obtained without using the fancy language of differential geometry, simply by working in a specified basis from the very beginning. But as we have just seen, there are certain interesting parallels between the geometric phase, curved manifolds and gauge fields, which may be useful for developing an understanding of the geometric phase. Differential geometry is just a natural tool to study these similarities.

Let us now consider the set of matrices $\mathbf{U}$ corresponding to all possible closed paths P starting and ending in a fixed given point $\mathbf{x}$. Such set obviously forms a group under matrix multiplication since any two closed paths P_1 and P_2 can be joined to form another closed path P and the matrix $\mathbf{U}$ corresponding to P is given by the product $\mathbf{U}_2 \cdot \mathbf{U}_1$ of the matrices for P_1 and P_2. Moreover, a degenerate loop consisting of only one point yields $\mathbf{U} = \mathbf{id}$ and reversing the direction of the path clearly transforms $\mathbf{U}$ into $\mathbf{U}^{-1}$. The matrix group defined in this way is called the *holonomy* of the parallel transport.

If this group is rich enough, specifically if it contains the group $SU(2)$ as its subgroup then it allows to perform arbitrary unitary operations on some two-dimensional computational subspace of the eigenspace $\mathscr{S}(\mathbf{x})$ by following suitably chosen closed paths starting and ending in $\mathbf{x}$. The geometric nature of such manipulation makes the resulting one-qubit gates less sensitive to noise, as discussed previously. The degeneracy of the computational states also eliminates the need to cancel the dynamical phases. Higher-dimensional degenerate eigenspaces could be used to accommodate two-qubit computational states and perform two-qubit fault-tolerant non-abelian geometric gates. It is therefore quite

natural that holonomic quantum computation based on non-abelian geometric phases is currently in the limelight of quantum information processing research – albeit mostly theoretically at this point.

B Parameters of the sample

Resonator					
Frequency	...	$\omega_r/2\pi$	...	7.0204	GHz
Decay rate	...	$\kappa/2\pi$	...	0.475	MHz
Mean photon lifetime	...	$\tau, 1/\kappa$	...	0.335	μs
Quality factor	...	$Q, \omega_r/\kappa$	...	14800	
Qubit					
Charging energy	...	$E_C/2\pi\hbar$	...	360	MHz
Max. Josephson energy	...	$E_J^{\max}/2\pi\hbar$	...	26	GHz
Max. frequency	...	$\omega_q^{\max}/2\pi$	...	8.3	GHz
Anharmonicity	...	$\alpha/2\pi$	...	-0.4	GHz
Resonator coupling	...	$g/2\pi$	...	56	MHz
Relaxation time	...	$T_1, 1/\Gamma$	...	$\lesssim 0.9^*$	μs
Dephasing time	...	$T_2, 1/\gamma$	...	$\lesssim 1.5^*$	μs
Dispersive shift	...	$\chi/2\pi$	...	1.0	MHz

*) Value varies over time by almost 50 %.

Index

References

[1] R.P. Feynman. Simulating physics with computers. *Int. J. Theor. Phys.*, 21:467–488, 1982.

[2] D. Deutsch. Quantum theory, the Church-Turing principle and the universal quantum computer. *Proc. R. Soc. Lond. A*, 400:97–117, 1985.

[3] D. Deutsch and R. Jozsa. Rapid solution of problems by quantum computation. *Proc. R. Soc. Lond. A*, 439:553–558, 1992.

[4] L.K. Grover. A fast quantum mechanical algorithm for database search. *Proceedings of the twenty-eighth annual ACM symposium on Theory of computing*, pages 212–219, 1996.

[5] P.W. Shor. Polynomial-time algorithms for prime factorization and discrete logarithms on a quantum computer. *SIAM Journal on Computing*, 26:1484–1509, 1997.

[6] D.P. DiVincenzo. The physical implementation of quantum computation. *Fortschr. Phys.*, 48:771–783, 2000.

[7] M.A. Nielsen and I.L. Chuang. *Quantum Computation and Quantum Information.* Cambridge University Press, 2000.

[8] J.I. Cirac and P. Zoller. Quantum computations with cold trapped ions. *Phys. Rev. Lett.*, 74:4091–4094, 1995.

[9] D.G. Cory, A.F. Fahmy, and T.F. Havel. Ensemble quantum computing by NMR spectroscopy. *Proc. Natl. Acad. Sci. USA*, 94:1634–1639, 1997.

[10] D. Loss and D.P. DiVincenzo. Quantum computation with quantum dots. *Phys. Rev. A*, 57:120–126, 1998.

[11] A. Blais, R.-S. Huang, A. Wallraff, S.M. Girvin, and R.J. Schoelkopf. Cavity quantum electrodynamics for superconducting electrical circuits: An architecture for quantum computation. *Phys. Rev. A*, 69:062320, 2004.

[12] A. Wallraff, D.I. Schuster, A. Blais, L. Frunzio, M.H. Devoret J. Majer, S.M. Girvin, and R.J. Schoelkopf. Approaching unit visibility for control of a superconducting qubit with dispersive readout. *Phys. Rev. Lett.*, 95:060501, 2005.

[13] J. Majer, J.M. Chow, J.M. Gambetta, J. Koch, B.R. Johnson, J.A. Schreier, L. Frunzio, D.I. Schuster, A.A. Houck, A.Wallraff, A. Blais, M.H. Devoret, S.M. Girvin, and R.J.M. Schoelkopf. Coupling superconducting qubits via a cavity bus. *Nature*, 449(7161):443–447, 2007.

[14] R. Bianchetti, S. Filipp, M. Baur, J.M. Fink, M. Göppl, P.J. Leek, L. Steffen, A. Blais, and A. Wallraff. Dynamics of dispersive single-qubit readout in circuit quantum electrodynamics. *Phys. Rev. A*, 80:043840, 2009.

[15] M.V. Berry. Quantal phase-factors accompanying adiabatic changes. *Proc. R. Soc. Lond. A*, 392(1802):45–57, 1984.

[16] B. Simon. Holonomy, the quantum adiabatic theorem, and Berry's phase. *Phys. Rev. Lett.*, 51:2167–2170, 1983.

[17] P.J. Leek, J.M. Fink, A. Blais, R. Bianchetti, M. Göppl, J.M. Gambetta, D.I. Schuster, L. Frunzio, R.J. Schoelkopf, and A.Wallraff. Observation of Berry's phase in a solid-state qubit. *Science*, 318(5858):1889–1892, 2007.

[18] S. Berger. Observation of Berry's phase in a transmon qubit. *unpublished*, 2010.

[19] G.J. Milburn, S. Schneider, and D.F.V. James. Ion trap quantum computing with warm ions. *Fortschr. Phys.*, 48:801–810, 2000.

[20] X.B. Wang and M. Keiji. Nonadiabatic conditional geometric phase shift with NMR. *Phys. Rev. Lett.*, 8709(9):097901, 2001.

[21] D. Leibfried, B. DeMarco, V. Meyer, D. Lucas, M. Barrett, J. Britton, W.M. Itano, B. Jelenkovic, C. Langer, T. Rosenband, and D.J. Wineland. Experimental demonstration of a robust, high-fidelity geometric two ion-qubit phase gate. *Nature*, 422(6930):412–415, 2003.

[22] M. Tinkham. *Introduction to Superconductivity.* McGraw-Hill, Inc., 1996.

[23] B.D. Josephson. The discovery of tunneling supercurrents. *Rev. Mod. Phys.*, 46:251–254, 1974.

[24] V. Bouchiat, D. Vion, P. Joyez, D. Esteve, and M.H. Devoret. Quantum coherence with a single cooper pair. *Phys. Script.*, T76:165–170, 1998.

[25] J.E. Mooij, T.P. Orlando, L. Levitov, L. Tian, C.H. van der Wal, and S. Lloyd. Josephson persistent-current qubit. *Science*, 285:1036–1039, 1999.

[26] J.M. Martinis, M.H. Devoret, and J. Clarke. Energy-level quantization in the zero-voltage state of a current-biased josephson junction. *Phys. Rev. Lett.*, 55:1543–1546, 1985.

[27] J. Koch, T.M. Yu, J. Gambetta, A.A. Houck, D.I. Schuster, J. Majer, A. Blais, M.H. Devoret, S.M. Girvin, and R.J. Schoelkopf. Charge-insensitive qubit design derived from the cooper pair box. *Phys. Rev. A*, 76:042319, 2007.

[28] M. Abramowitz and I.A. Stegun. *Handbook of Mathematical Functions with Formulas, Graphs, and Mathematical Tables.* National Bureau of Standards, 1972.

[29] A. Messiah. *Quantum Mechanics, Volume I.* North-Holland Publishing Company, Amsterdam, 1961.

[30] M.K. Tey, Z. Chen, S.A. Aljunid, B. Chng, F. Huber, G. Maslennikov, and C. Kurtsiefer. Strong interaction between light and a single trapped atom without the need for a cavity. *Nature Phys.*, 26:924–927, 2008.

[31] D.F. Walls and G.J. Milburn. *Quantum Optics*. Springer-Verlag, 2008.

[32] H.-P. Breuer and F. Petruccione. *The Theory of Open Quantum Systems*. Oxford University Press, 2002.

[33] S. Filipp, P. Maurer, P.J. Leek, M. Baur, R. Bianchetti, J.M. Fink, M. Gppl, L. Steffen, J.M. Gambetta, A. Blais, and A. Wallraff. Two-qubit state tomography using a joint dispersive read-out. *Phys. Rev. Lett.*, 102:200402, 2009.

[34] L. DiCarlo, M.D. Reed, L. Sun, B.R. Johnson, J.M. Chow, J.M. Gambetta, L. Frunzio, S.M. Girvin, M.H. Devoret, and R.J. Schoelkopf. Preparation and measurement of three-qubit entanglement in a superconducting circuit. *Nature*, 467:574–578, 2010.

[35] M. Neeley, R.C. Bialczak, M. Lenander, E. Lucero, M. Mariantoni, A.D. O'Connell, D. Sank, H. Wang, M. Weides, J. Wenner, Y. Yin, T. Yamamoto, A.N. Cleland, and J.M. Martinis. Generation of three-qubit entangled states using superconducting phase qubits. *Nature*, 467:570–573, 2010.

[36] L.D. Landau and L.M. Lifshitz. *Mechanics, Third edition*. Pergamon Press plc, 1976.

[37] E. Ott. Goodness of ergodic adiabatic invariants. *Phys. Rev. Lett.*, 42:1628–1631, 1979.

[38] M. Born and V. Fock. Beweis des Adiabatensatzes. *Zeit. Phys. A*, 51:165–180, 1928.

[39] A. Messiah. *Quantum Mechanics, Volume II*. North-Holland Publishing Company, Amsterdam, 1962.

[40] F. Wilczek and A. Zee. Appearance of gauge structure in simple dynamical systems. *Phys. Rev. Lett.*, 52:2111–2114, 1984.

[41] P. Zanardi and M. Rasetti. Holonomic quantum computation. *Phys. Lett. A*, 264:94–99, 1999.

[42] S. Pancharatnam. *Proc. Indian Acad. Sci.*, A44:247, 1956.

[43] Y. Aharonov and J. Anandan. Phase-change during a cyclic quantum evolution. *Phys. Rev. Lett.*, 58(16):1593–1596, 1987.

[44] S.L. Zhu and P. Zanardi. Geometric quantum gates that are robust against stochastic control errors. *Phys. Rev. A*, 72(2):020301, 2005.

[45] S.-B. Zheng. Unconventional geometric quantum phase gates with a cavity QED system. *Phys. Rev. A*, 70:052320, 2004.

[46] L.-M. Duan, J. I. Cirac, and P. Zoller. Geometric Manipulation of Trapped Ions for Quantum Computation. *Science*, 292(5522):1695–1697, 2001.

[47] Y. Aharonov and D. Bohm. Significance of electromagnetic potentials in the quantum theory. *Phys. Rev. A*, 115:485–491, 1959.

[48] J. Samuel and R. Bhandari. General setting for Berry's phase. *Phys. Rev. Lett.*, 60:2339–2342, 1988.

[49] N. Manini and F. Pistolesi. Off-diagonal geometric phases. *Phys. Rev. Lett.*, 85:3067–3071, 2000.

[50] J.C. Garrison and E.M. Wright. Complex geometrical phases for dissipative systems. *Phys. Lett. A*, 128(3-4):177–181, 1988.

[51] E. Sjöqvist, A.K. Pati, A. Ekert, J.S. Anandan, M. Ericsson, D.K.L. Oi, and V. Vedral. Geometric phases for mixed states in interferometry. *Phys. Rev. Lett.*, 85:2845–2849, 2000.

[52] S. Filipp and E. Sjöqvist. Off-diagonal geometric phase for mixed states. *Phys. Rev. Lett.*, 90:050403, 2003.

[53] X. Wang, A. Sørensen, and K. Mølmer. Multibit gates for quantum computing. *Phys. Rev. Lett.*, 86:3907–3910, 2001.

[54] M. Göppl, A. Fragner, M. Baur, R. Bianchetti, S. Filipp, J.M. Fink, P.J. Leek, G. Puebla, L. Steffen, and A. Wallraff. Coplanar waveguide resonators for circuit quantum electrodynamics. *Journal of Applied Physics*, 104(11):113904, 2008.

[55] G. Ventura and L. Risegari. *The Art of Cryogenics*. Elsevier, 2007.

[56] S. Schmidlin. Generation of amplitude and phase controlled microwave pulses for qubit manipulation in circuit QED. *unpublished*, 2009.

[57] F. Motzoi, J.M. Gambetta, P. Rebentrost, and F.K. Wilhelm. Simple pulses for elimination of leakage in weakly nonlinear qubits. *Phys. Rev. Lett.*, 103:110501, 2009.

[58] C. J. Isham. *Modern Differential Geometry for Physicists (2nd Edition)*. World Scientific Publishing Co. Pte. Ltd., 1999.

Acknowledgements

First of all, I would like to thank Prof. Andreas Wallraff for the opportunity to join his lab and not only work on an intriguing topic in quantum mechanics but also learn a lot about the practical side of physics. This was essentially my first real encounter with experimental work and it turned out to be a truly enriching and enjoyable experience.

My work would have been a great deal more difficult without Simon Berger who introduced me to the measurement software and hardware, spent a lot of time in the lab with me and was always willing to answer all of my rookie questions. Many thanks go to Dr. Stefan Filipp for awaking my interest in the geometric phase, proposing the topic of this thesis to me and initiating many inspiring discussions about the subject. They both provided me with useful feedback which proved to be a great help in writing this thesis.

I am very grateful to Dr. Farruh Abdumalikov for his invaluable help with the sometimes uncooperative experimental setup, as well as for his questions and comments, often so helpful in making me pause and *think* about what I was doing.

Whenever there was a need to dig deep into the cryptic guts of Cleansweep we could rely on the helping hand and expert advice of Christian Lang. I am also thankful to Arjan van Loo for his assistance with my first steps in Simon's absence, to Johannes Fink who manufactured the sample and to Jonas Mlynek who did much of the work needed to characterise it and prepare the experimental setup for measurements.

Obviously, this work would have been impossible without all those people who have worked in the lab since its start and put a vast amount of work into developing the measurement setup, techniques and software into their current state in which the measurement process is surprisingly simple and user-friendly.

My special thanks go to my family for being always there for me and supporting me during my studies, to my Swiss friends for helping me settle down in Zurich and making my stay very enjoyable and to my non-Swiss friends for keeping in touch which really meant a lot to me.